UNIVERSITÀ DEGLI STUDI DI PADOVA

DIPARTIMENTO DI SCIENZE CHIMICHE

CORSO DI LAUREA MAGISTRALE IN
SCIENZA DEI MATERIALI

TESI DI LAUREA MAGISTRALE

B-site doped Strontium Molybdate: a suitable material for thermo- and electro-catalytic valorisation of hydrogen from organic waste fermentation

RELATORE: Chiar.ma Prof.ssa Antonella Glisenti

CO-RELATORE: Chiar.mo Graziano Tassinato, PhD

CONTRORELATORE: Chiar.mo Prof. Andrea Sartorel

LAUREANDO: Davide Chinello

MATRICOLA: 2063134

ANNO ACCADEMICO 2022/2023

“Fasten your seatbelts. It’s going to be a bumpy night.”

Margo Channing, “All about Eve”

Index

INTRODUCTION 1

1. SOLID OXIDE FUEL CELLS 5

1.1 Fuel Cells introduction 5
1.1.1 Fuel Cells efficiency 6

1.2 Fuel Cell typologies 8
1.2.1 Market distribution 9
1.2.2 Proton Exchange Membrane fuel cells (PEMFCs) 10
1.2.3 Phosphoric Acid Fuel Cells (PAFCs) 11
1.2.4 Alkaline Fuel Cells (AFCs) 12
1.2.5 Direct Methane Fuel Cells (DMFCs) 12
1.2.6 Molten Carbonate Fuel Cells (MCFCs) 13

1.3 Solid Oxide Fuel Cells (SOFCs) 14
1.3.1 Historical background 15
1.3.2 Cell components: the anode 15
1.3.3 Cell components: the cathode 17
1.3.4 Cell components: the electrolyte 18

1.4 Reversible SOFCs 21

1.5 SOFCs challenges 22

2. PEROVSKITE MATERIALS 27

2.1 Crystalline structure 27

2.2 Perovskite properties 28

2.3 Double perovskite materials 29

3. SYNTHESIS AND CHARACTERIZATION OF SMMO MATERIALS 33

3.1 Main synthesis routes 33
3.1.1 Solid state synthesis 33
3.1.2 Wet chemistry synthesis 33

3.2 The Pechini method 34

3.3 X-Ray Diffraction (XRD) 35
3.3.1 Air atmosphere 35
3.3.2 5% H2 atmosphere 38

3.4 H_2 – Temperature Programmed Reduction (H_2 – TPR) 40

3.5 Understanding the morphology: Scanning Electron Microscopy (SEM) 42

3.6 Understanding the composition: Energy Dispersive X-Ray (EDX) and quantitative X-Ray Photoelectron Spectroscopy (XPS) 44

3.7 Understanding the surfaces: qualitative X-Ray Photoelectron Spectroscopy (XPS) 45
3.7.1 Strontium XPS spectra 47
3.7.2 Magnesium XPS spectra 48
3.7.3 Manganese XPS spectra 48
3.7.4 Molybdenum XPS spectra 50
3.7.5 Oxygen XPS spectra 51

4. THERMO-VALORISATION OF THE GAS MIXTURE: CO_2 REDUCTION TO CO 57

4.1 Catalytic results 58

4.2 Post-reaction Characterization of SMMO materials 60
4.2.1 X-Ray Diffraction (XRD) 60
4.2.2 Understanding the post-reaction morphology: Scanning Electron Microscopy (SEM) 63
4.2.3 Understanding the post-reaction composition: Energy Dispersive X-Ray (EDX) and quantitative X-Ray Photoelectron Spectroscopy (XPS) 64
4.2.4 Understanding the post-reaction surfaces: X-Ray Photoelectron Spectroscopy (XPS) 68

5. CELL DESIGN AND MANUFACTURING PROCESSES 77

5.1 SOFC configurations 77
5.1.1 Tubular design 77
5.1.2 Planar design 78

5.2 Cells construction 79
5.2.1 Choice of the electrolyte: compatibility and adhesion tests 80

5.3 Cell mounting 83

6. ELECTROCHEMICAL IMPEDENCE SPECTROSCOPY (EIS) CHARACTERIZATION OF SYMMETRICAL CELLS 85

6.1 EIS theory 85

6.2 EIS anode characterization 89
6.2.1 H_2 in Ar fuel 90
6.2.2 H_2 + CO_2 – in Ar – fuel 95

CONCLUSIONS AND OUTLOOKS **101**

APPENDIXES **111**

Appendix A: Brunauer-Emmett-Teller (BET) analysis 111

Appendix B: new SOFC testing set-up 113

AKNOWLEDGMENTS **115**

Introduction

The environmental problem

Among the problems that nowadays society has to face, a special attention has been given to the environment and to the energy production and consumption. These issues, that follow the developing of the global progresses in economy and technology, are mainly due to the utilization of non-renewable resources, the so-called "fossil fuels", as the principal energy production sources since the Industrial Revolution that took place in the 19th century, and to the continuous increase of waste production. Until today, only a few steps have been made to move towards the utilization of green approaches and to reduce the production of waste, ignoring their correlation to the disaster caused by the climate change. For example, Thwaites glacier, located in West Antarctica and known to be the biggest glacier in the World, is reported to be losing 50 billion tons of ice per year, causing the rise of 3 meters of the sea level. [1]

The widespread use of fossil fuels in the energy-intense industries is considered to be one of the main causes of harmful gas emissions in the atmosphere as CO_2, SO_2 and NO_x; while the first is well known to be the cause of the greenhouse effect, and so of all the issues related to the increase of the global temperature, the others are responsible not only for acid rains, but also for deaths caused by respiratory and cardiovascular diseases (6.4 million only in 2015). [2,3]

Moreover, although non-renewable sources are considered cheaper in respect to their "green" alternatives, their real cost is continuously increasing due to the impoverishment of these resources and to the "hidden cost" for the mitigation of their ecological and health impact.

The need of cleaner solutions

The priorities in the energy field are therefore exploring both the valorisation of the same pollutants to obtain alternative fuels and the environmentally friendly alternatives to fossil fuels as wind, solar or hydric energy, in order to reduce the emission of pollutants in the atmosphere. Nevertheless, renewable technologies are often criticized for their scarce ability to adapt their energy production to the customers' needs, as they are intermittent and frequently distant from the application place.

A promising way to implement the green routes is given by the possibility to store vast amounts of energy in the form of chemical compounds such as hydrogen, methane, methanol or dimethyl ether

(DME). In such a way, chemical compounds can be easily transported and converted into electrical energy “on demand”.

As a matter of facts, many governments lead by the United States and the European Union are considering the hypothesis of a hydrogen-based economy, developing new non-greenhouse emitting systems, in such a way to reach the goal fixed to 2050 of zero carbon emission. [4] Fuel cells could be very useful for this aim, as they are able to convert chemical energy into electrical energy with a higher efficiency and lower emissions compared to the traditional combustion of fossil fuels, with the production of water as only by-product. Moreover, compared to other sustainable energy sources as batteries, fuel cells are able to generate continuously electric energy, as long as fuel and oxygen are supplied.

In particular, focusing on a hydrogen-based energy system, new approaches are needed to supply enough fuel to satisfy the global requests. Currently, the principal production method is based on the reforming of natural gas (47% of the produced hydrogen), followed by the use of coal and oil (27% and 22%), and thus it is still not independent from fossil fuels. In this regard, an interesting long-term alternative that is being studied and still not applied in a wide scale, but however characterized, in principle, by a high efficiency, is represented by the dark fermentation with mixed coltures. [5] This particular approach represents a new research line especially for waste management company like Veritas, leader in the garbage collection in the province of Venice, which is now dedicating on the valorisation of the organic slurry via traditional biogas production and, as said, fermentation of agricultural residues, food waste and others, resulting in a gas mixture composed by 80% H_2 and 20% CO_2. [6,7]

Moreover, new limitation to the utilisation of traditional fuels has recently been set by the European Union, in order to lower the pollutants emission deriving from the combustion in heat engines, typically used in the transport sector. In fact, new European rules that will come into force in 2035 will shut down the production and the use of internal combustion engine powered cars, unless the fuels come from synthetic origin (the so-called e-fuel). [8,9] Thus, the scientific research needs to put more efforts on the re-valorisation of CO_2 through a direct way, as in the methanation via the Sabatier reaction, or an indirect way, as in its reduction to CO via the Reverse Water Gas Shift (RWGS) reaction. [10,11] CO and H_2 are the main reagents in some reactions, like the Fischer-Tropsch one, that are well known to lead to the formation of synthetic hydrocarbons. [12]

Aim of the work

Taking into account the previous considerations, this work will be focused on the synthesis, characterization and performances evaluation of $Sr_2Mg_{1-x}Mn_xMoO_6$-based double perovskites, considered as anode in Solid Oxide Fuel Cells (SOFCs), a particular sub-group of Fuel Cells that will be explained in a dedicated chapter (*Chapter 1*). Double perovskites are a particular kind of mixed oxides characterized by the possibility to up-grade reactivity and conductivity by means of the accurate selection of the composition (*Chapter 2*). The synthesis will be carried out by means of wet chemistry procedures, in order to favour the industrial up-scale and the characterization will help in following the steps of the preparation procedure (*Chapter 3*). In particular, X-Ray powder Diffraction will be used for the identification of the phases and the crystalline structures, SEM images will be useful for the determination of the morphology, EDX and XPS will give back information on the composition (the latter will also be useful for the investigation of oxidation states of the various elements). The valorisation of an 80% H_2 and 20% CO_2 simulated gas mixture, as obtained by dark fermentation, will be achieved in a dual approach: the utilisation of the materials as catalysts for the thermo-catalytic reduction of CO_2 to CO via the RWGS reaction (*Chapter 4*) and the design (*Chapter 5*) and electrocatalytic activity towards H_2 oxidation of a SOFC based on SMMO electrodes (*Chapter 6*).

References

1 B. E. Schmidt, P. Washam, P. E. D. Davis, K. W. Nicholls, D. M. Holland, J. D. Lawrence, K. L. Riverman, J. A. Smith, A. Spears, D. J. G. Dichek, A. D. Mullen, E. Clyne, B. Yeager, P. Anker, M. R. Meister, B. C. Hurwitz, E. S. Quartini, F. E. Bryson, A. Basinski-Ferris, C. Thomas, J. Wake, D. G. Vaughan, S. Anandakrishnan, E. Rignot, J. Paden and K. Makinson, Heterogeneous melting near the Thwaites Glacier grounding line, *Nature*, 2023, **614**, 471–478.

2 B. Kamarehie, M. Ghaderpoori, A. Jafari, M. Karami, A. Mohammadi, K. Azarshab, A. Ghaderpoury, A. Alinejad and N. Noorizadeh, Quantification of health effects related to SO_2 and NO_2 pollutants by using Air quality model, *Journal of Advances in Environmental Health Research*, 2017, **5**, 44–50.3 P. J. Landrigan, Air pollution and health, *The Lancet Public Health*, 2017, **2**, e4–e5.

4 J. O. Abe, A. P. I. Popoola, E. Ajenifuja and O. M. Popoola, Hydrogen energy, economy and storage: Review and recommendation, *International Journal of Hydrogen Energy*, 2019, **44**, 15072–15086.

5 M. El-Shafie, S. Kambara and Y. Hayakawa, Hydrogen Production Technologies Overview, *JPEE*, 2019, **07**, 107–154.

6 X. M. Guo, E. Trably, E. Latrille, H. Carrère and J.-P. Steyer, Hydrogen production from agricultural waste by dark fermentation: A review, *International Journal of Hydrogen Energy*, 2010, **35**, 10660–10673.

7 A. Noblecourt, G. Christophe, C. Larroche and P. Fontanille, Hydrogen production by dark fermentation from pre-fermented depackaging food wastes, *Bioresource Technology*, 2018, **247**, 864–870.

8 A. K. Agarwal and H. Valera, in *Greener and Scalable E-fuels for Decarbonization of Transport*, eds. A. K. Agarwal and H. Valera, Springer Singapore, Singapore, 2022, 3–8.

9 J. Liboreiro, *In win for Germany, EU agrees to exempt e-fuels from 2035 ban on new sales of combustion-engine cars*, 2023.

10 A. Shima, M. Sakurai, Y. Sone, M. Ohnishi and T. Abe, in *42nd International Conference on Environmental Systems*, American Institute of Aeronautics and Astronautics, San Diego, California, 2012.

11 M. González-Castaño, B. Dorneanu and H. Arellano-García, The reverse water gas shift reaction: a process systems engineering perspective, *React. Chem. Eng.*, 2021, **6**, 954–976.

12 C. Masters, in *Advances in Organometallic Chemistry*, Elsevier, 1979, vol. 17, pp. 61–103.

1. Solid Oxide Fuel Cells

1.1 Fuel Cells introduction

Fuel Cells (FC) are electrochemical devices able to convert chemical energy (in form of fuels) in electrical energy with high efficiency and low environmental impact. Their working principle is based on a serie of redox reactions between a fuel (usually hydrogen), that needs to be oxidized, and an oxidizing agent (usually air). [1,2]

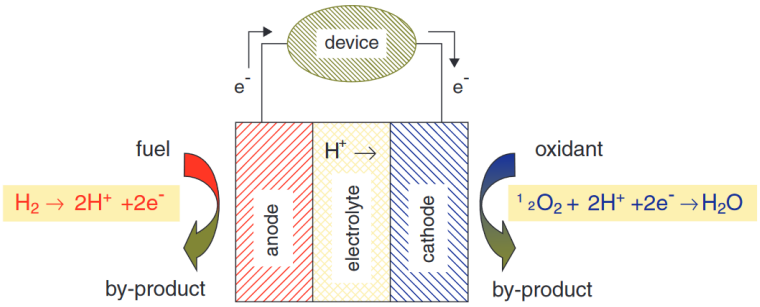

Figure 1.1: schematic representation of a proton conductive electrolyte-based fuel cell. [3]

Among standard energy-production devices, fuel cells present some advantage, like the absence of combustion processes, and thus of limitations due to the Carnot cycle, and the high energy conversion efficiency. Moreover, the lack of combustion ensures the absence pollutant by-products as water is the only outcome of the redox reaction if hydrogen is the only fuel supplied. Another advantage is related to the design of the device: the lack of mobile parts ensures a reliable and silent device, with the possibility to apply some types of cells in portable applications due to their manageable miniaturization.

Nevertheless, fuel cells have some disadvantages such as the need for highly pure hydrogen, that is expensive to produce and ideally it should be obtained in green ways. Moreover, there are some issues related with the transportation and storage of this fuel. A possible answer to these problems, however, is the use of high temperature fuel cells, where hydrogen can be produced and used in situ by internal reforming. A further solution could be the use of reversible SOFC (R-SOFC) devices, that can operate following two paths: the first ensures the production of energy from fuels, the second permits the production of hydrogen operating the inverse process (with electric energy produced from renewable sources, for example).

Although fuel cells are not a widespread technology, in the recent few years the energy production deriving from these devices has seen an important increase, as the number of units sold around the world.

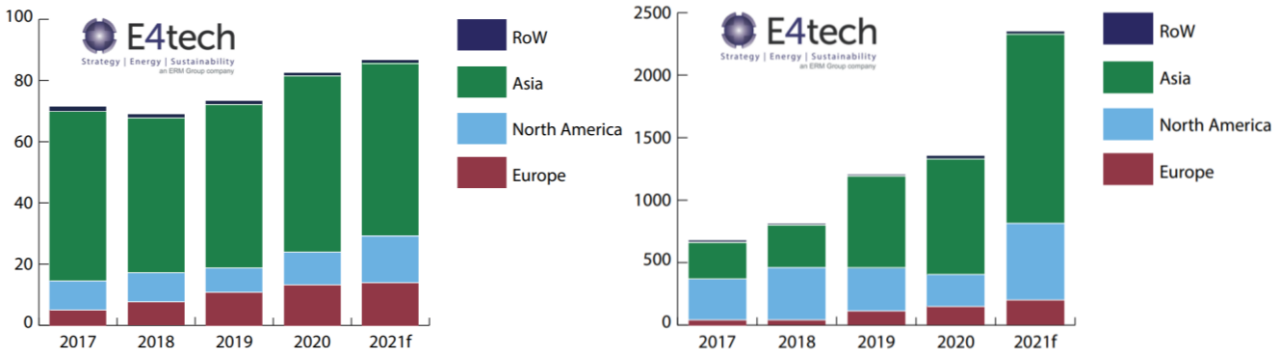

Figure 1.2: units sold by region of adoption between 2017 and 2021 (1000 units) (sx); megawatts by region of adoption between 2017 and 2021 (dx).

Giving a look to the global market distribution, compared to the energy production, Asia is clearly leading in unit numbers and megawatts; Europe is catching up North America in terms of unit shipments but lagging in megawatts, while Rest of the World (RoW) barely figures (about 600 units shipped, totalling 1.4 MW). These comprise mainly stationary and portable back-up and off-grid units delivered to a range of countries.

Even if the market has increased during the last five years, it is only the initial step of a widespread phenomenon. In fact, new projects worldwide are focusing on this technology, including portable and stationary devices. For example, the US, eastern Asia countries and some countries in Europe like France, Germany and the Netherlands are moving to a fuel cell based maritime infrastructure, with a special consideration for SOFCs [4]; Denish and Norwegian sea shipping companies, instead, are among the pioneers of fuel cell application to cargo boats in order to reduce of 60% their CO_2 emissions, in the context of international environmental agreements [5], while big automotive company based in Asia (like Hyundai, for instance) are planning to delivery 50000 fuel cell equipped vehicles (FCEV) in 2025, 20% of which will be heavy-duty. [6]

1.1.1 Fuel Cells efficiency

Even if fuel cells present a higher efficiency compared to traditional combustion-based devices, there are some limitations that are not possible to overcome. The total energy produced is:

$$W_e = \eta_T \cdot W_C \tag{1.1}$$

where η_T is the total efficiency and W_C the total chemical energy supplied. The chemical energy that is not used to produce electrical energy can be evaluated by the efficiency of fuel use (η_C), by the Gibbs efficiency (η_G) and by the electrical efficiency (η_V). The efficiency of fuel use is the quantity

of fuel that is consumed with relation to the quantity that was supplied and depends on the kinetics of the process and on its parameters.

The Gibbs efficiency is the ratio between the Gibbs free energy and the enthalpy of the chemical reaction involved in the cell:

$$\eta_G = \frac{\Delta_r G}{\Delta_r H} = \frac{\Delta_r H - T\Delta_r S}{\Delta_r H} = 1 - \frac{T\Delta_r S}{\Delta_r H} \tag{1.2}$$

Remembering that:

$$\left(\frac{\partial \Delta_r G^\circ}{\partial T}\right)_p = -\Delta_r S^\circ \tag{1.3}$$

$$\left(\frac{\partial \Delta_r H^\circ}{\partial T}\right)_p = -\Delta_r C_p \tag{1.4}$$

$T\Delta_r S$ represents the chemical energy fraction that is dissipated as heat. Moreover, $\Delta_r H°$ can be considered as independent from T because $\Delta_r C_p$ is usually very small and can be approximated to zero. It is then possible, to identify η_G, linking it to the fact that only the chemical energy quantity defined by $\Delta_r G$ can be turned into useful work. Even with this limitation, fuel cells have a better efficiency than a combustion-based device, because there are not the limitations imposed by the Carnot cycle for the conversion of heat into useful work.

The electromotive force is calculable from the Gibbs free energy:

$$\Delta E_{rev} = -\frac{\Delta_r G}{nF} \tag{1.5}$$

The electrical efficiency is due to the cell internal ohmic losses. They can be dependent on the current flow (polarization, electronic transfer, etc.) or independent from it (ohmic resistance of the materials). It follows:

$$R_{tot} = R_0 + R(i) \tag{1.6}$$

The electrical efficiency is the ratio between the effective cell potential and the thermodynamic theoretical value; when $R(i) \ll R_0$, that is usually verified, the electrical efficiency can be linearized, assuming $R_{tot} = R_0$:

$$\eta_V = \frac{V}{\Delta E_{rev}} = \frac{\Delta E_{rev} - R_{tot} \cdot I}{\Delta E_{rev}} = \frac{\Delta E_{rev} - R_0 \cdot I}{\Delta E_{rev}} = 1 - \frac{R_0 \cdot I}{\Delta E_{rev}} \tag{1.7}$$

The internal resistance $R(i)$ is not always negligible. In those cases, the main contribute is the activation overpotential, that is due to the scarce velocity of the electrode processes that happens in the cell.

The overall efficiency is then:

$$\eta_T = \eta_C \cdot \eta_G \cdot \eta_V = \frac{W_e}{W_C} \tag{1.8}$$

It follows:

$$W_e = (\eta_C \cdot \eta_G \cdot \eta_V) \cdot W_C \tag{1.9}$$

1.2 Fuel Cell typologies

Fuel cells classification is based on their electrolyte, fuel and working temperature, as it can be seen in *Figure 1.3*. Thus, it is possible to differentiate the devices in two categories:

Low temperature Fuel Cells (50-250°C):

- Proton Exchange Membrane Fuel Cells (PEM)
- Phosphoric Acid Fuel Cells (PAFC)
- Alkaline Fuel Cells (AFC)

High temperature Fuel Cells (600-1000°C):

- Direct Methanol Fuel Cells (DMFC)
- Molten Carbonates Fuel Cells (MCFC)
- Solid Oxide Fuel Cells (SOFC)

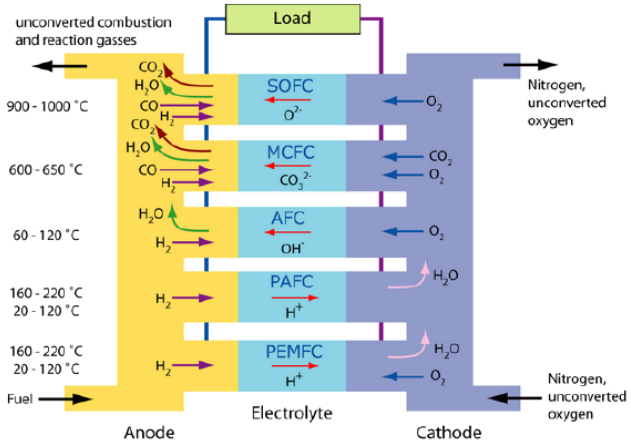

Figure 1.3: schematic representation of the main types of fuel cells.

Application type	Portable	Stationary	Transport
Definition	Units that are built into, or charge up, products that are designed to be moved, including small auxiliary power units (APUs)	Units that provide electricity but are not designed to be moved	Units that provide propulsive power or range extension to a vehicle
Power range	1 W to 20 kW	0.5 kW to 2 MW	1 kW to 300 kW
Typical technology	PEMFC DMFC SOFC	PEMFC MCFC AFC SOFC PAFC	PEMFC DMFC
Example	• Small "movable" APUs (camper-vans, boats, lighting) • Military applications (portable soldier-borne power, generators) • Portable products (torches, battery chargers), small personal electronics (mp3 player, cameras)	• Large stationary prime power and combined heat and power (CHP) • Uninterruptible power supplies (UPS) • Larger 'permanent' APUs (e.g. trucks and ships)	• Materials handling vehicles • Fuel cell electric vehicles (FCEV) • Trucks and buses • Rail vehicles • Autonomous vehicles (air, land or water)

Table 1.1: principal characteristics and applications of fuel cells. [3]

1.2.1 Market distribution

In recent times, fuel cells are gaining importance in the industrial and transportation market. This has influenced the field of study of these devices, that is increasing more and more.

Analysing the overall market is possible to see that PEMs lead both in units and MWs capacity. SOFCs, moreover, have seen a growth in MWs of almost 40% in only one year; the main actor is Bloom Energy, primary selling in the US and Korea, while other suppliers like Bosch and Ceres are influent for a smaller volume. This increase is due to the PEMs supply drop in initiatives like Ene-Farm, PACE and KfW 433, that is compensated by the doubling of the MWs capacity.

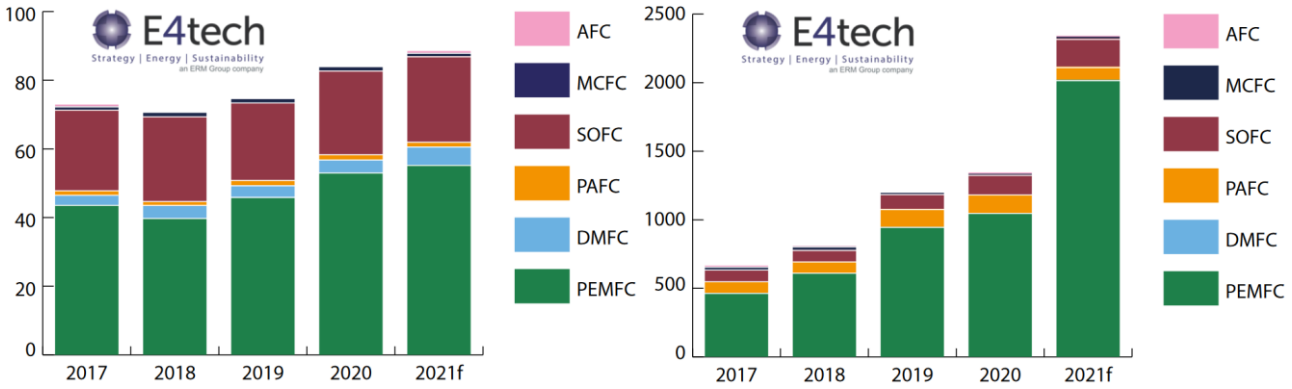

Figure 1.4: shipments by fuel cell type between 2017 and 2021 (1000 units) (sx); megawatts delivered by fuel cell type between 2017 and 2021 (dx).

For what concerns the other types of fuel cells, PAFCs have not met the expectation since the delay of translating Korea's initiative regarding hydrogen into a supportive fiscal action. MCFCs have not seen an increase in the unit sold, while DMFC technology is still stable both in units supplied and MWs shipped. Last but not least, AFCs are making a coming back, led by the Israeli company GenCell: in fact, during the only 2020 the company has delivered five times the amount of stacks produced in the occurred since its foundation. [3]

1.2.2 Proton Exchange Membrane fuel cells (PEMFCs)

The proton exchange membrane fuel cell is certainly the most known technology among the fuel cell types and it is considered as a potential replacement for internal combustion (IC) engines in the transport sector. [7] These devices are mainly based on a polymeric membrane, that acts as electrolyte and ensures the proton conductivity (while electron flow is blocked), bonded between two porous carbon electrodes; the principal compound used for this purpose is Nafion®, a sulfonated tetrafluoro-ethylene-based co-polymer.

The process involved in the cell operation is the combustion of H_2 with the consequent production of H_2O. Thus:

anode: $2H_2 \rightarrow 4H^+ + 4e^-$

cathode: $O_2 + 4H^+ + 4e^- \rightarrow 2H_2O$

overall process: $2H_2 + O_2 \rightarrow 2H_2O$

PEMs are able to reach efficiency of about 50%, with a power density comparable to an IC engine one (1.35 kW/L). [7] Nevertheless, the main advantage of these cell is its low operative temperature of about 60-80°C, that grants very quick start-and-stop operations thanks to the possibility to reach quickly the operating temperature regime. This is the principal reason that makes these cells suitable for portable applications, as the ones requests by the automotive industry.

The low operating temperature, however, is the cause for the slow chemical kinetics of these cells. For this reason, Platinum Group Materials (PGMs) are needed as catalysts for both anode and cathode reactions. PGMs are critical raw materials, with extremely low abundancy and located in specific geographic areas, that result in a high cost and an uncertain supply. Thus, the PEM field of study is now focusing on the research of new non-PGM catalysts.

1.2.3 Phosphoric Acid Fuel Cells (PAFCs)

In the last decade, phosphoric acid fuel cells have increased in popularity, thanks to their good reliability and efficiency (about 85%). [8] These cells are highly used where the energy supply cannot be stopped, even for a short period of time. Compared to the traditional power supply systems, this kind of devices ensures a reduction of fuel usage and pollution emissions. PAFCs' main characteristic is that the electrolyte is phosphoric acid (H_3PO_4), that ensures a cationic mobility.

The processes that grant the production of electrical energy are:

anode: $2H_2 \rightarrow 4H^+ + 4e^-$

cathode: $O_2 + 4H^+ + 4e^- \rightarrow 2H_2O$

overall process: $2H_2 + O_2 \rightarrow 2H_2O$

This device has a working temperature of about 200°C, thus a catalyst is needed; carbon-supported platinum is the most commonly used one, both for the oxidation of hydrogen fuel at the anode and oxygen reduction at the cathode. Its cons are platinum dissolution and carbon corrosion at voltages above 0.8 V, together with the kinetic hindrance of the oxygen reduction reaction. [8] More studies are then needed to optimize these types of catalysts.

1.2.4 Alkaline Fuel Cells (AFCs)

AFCs are probably, from a historical point of view, the most important type of fuel cells. In fact, one of these cells was installed by NASA during the Apollo program in the 60's, formerly calling it Bacon fuel cell after its British inventor and resulting in a leading technology to the first human landing on the Moon. [9] This device is characterized by an alkaline aqueous electrolyte made of potassium hydroxide (KOH), which assures high mobility of hydroxide anions (OH^-) but with some disadvantages, as its high sensitivity to CO_2, with which it reacts consuming itself and reducing its concentration. Moreover, KOH is highly corrosive and confers a short life cycle to the device.

The following processes are involved in the cell operation:

anode: $2H_2 + 4OH^- \rightarrow 4H_2O + 4e^-$

cathode: $O_2 + 2H_2O + 4e^- \rightarrow 4OH^-$

overall process: $2H_2 + O_2 \rightarrow 2H_2O$

The working temperature is about 100°C and the efficiency is relatively high (60-70%).

These devices are not suitable for commercial applications due to complication related to the alkaline electrolyte, but they're still used in boats and Space Shuttles. [9]

1.2.5 Direct Methane Fuel Cells (DMFCs)

These devices consist in an anode in which methanol is electro-chemically oxidized into CO_2 and a cathode in which oxygen, usually as air, is reduced to water (liquid or in steam form):

anode: $CH_3OH + H_2O \rightarrow CO_2 + 6H^+ + 6e^-$

cathode: $\frac{3}{2}O_2 + 6H^+ + 6e^- \rightarrow 3H_2O$

overall process: $CH_3OH + \frac{3}{2}O_2 \rightarrow CO_2 + 2H_2O$

The great advantage of this cell is the use of methanol, which is cheaper, safer, and easier to obtain and to process with relation to hydrogen. Moreover, the DMFC has a high volumetric theoretical energy density that makes it suitable for portable applications. [10]

In this kind of fuel cells, solid polymers represent an attractive alternative to the traditional liquid electrolytes. Nafion® polymers are the most attractive membranes for this device, although a methanol

transport across them has been observed, resulting in depolarization losses at the cathode site. In order to improve the performances, it is thus mandatory to eliminate or, at least, to reduce the loss of fuel across the cell, usually termed ‘‘methanol crossover’’. [11]

Other issues that need to be overcome are: [10]

- The slow kinetics of methanol electrochemical oxidation
- The low activity of the anode side, that needs to be improved by, for example, increasing the temperature
- The presence of noble metals in catalysts

1.2.6 Molten Carbonate Fuel Cells (MCFCs)

MCFCs are characterized by a working temperature above the melting temperature of the carbonates and the results is the charge transportation by the carbonate ion (CO_3^{2-}) within the liquid electrolyte. For the electrolyte, most developers have adopted an eutectic mixture of lithium and potassium carbonates (62 wt% Li and 38 wt% K), which has a melting point around 550°C. Thus, the operating temperature of these devices is around 650°C. This mixture is usually impregnated into a porous solid support matrix made of lithium aluminate ($LiAlO_2$). However, since both anode and cathode also need to be porous to allow the reacting gases to reach the electrode/electrolyte interfaces, the pore structure of the cell components needs to be carefully controlled so that electrolyte loss is minimised. [12]

The reaction involved at the electrodes are:

anode: $2H_2 + 2CO_3^{2-} \rightarrow 2H_2O + 2CO_2 + 4e^-$

cathode: $O_2 + 2CO_2 + 4e^- \rightarrow 2CO_3^{2-}$

overall process: $2H_2 + O_2 \rightarrow 2H_2O$

The electrical efficiency of this cell is about 47% and the total one is of 80%. [13]

Although the materials costs are relatively low if compared with other fuel cell types (no PGMs are required as electro-catalysts), there are major problems associated with degradation of materials and the poor lifetime of cells. So, nowadays research is focused both in the selection of materials to increase the operating life of the cell and system design to maximize the benefit of internal reforming.

1.3 Solid Oxide Fuel Cells (SOFCs)

SOFCs are based on a solid electrolyte, usually a mixed oxide, that can exhibit either ion conductivity (O^{2-}) or proton conductivity (H^+) but has to be electrically isolating. Both anode and cathode need to be porous, in order to guarantee an optimal gas diffusion between the cell sides. [14] The occurring reactions in an ideal cell, thus fuelled by hydrogen only, are:

anode: $2H_2 + 4OH^- \rightarrow 4H_2O + 4e^-$

cathode: $O_2 + 2H_2O + 4e^- \rightarrow 4OH^-$

overall process: $2H_2 + O_2 \rightarrow 2H_2O$

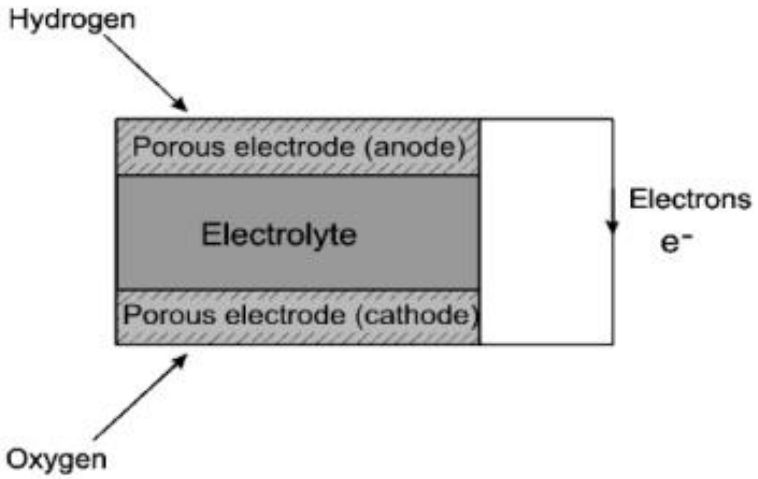

Figure 1.5: schematic representation of an electrolyte-supported SOFC.

SOFCs seem to be very promising as energy production technology, due to their numerous advantages, the most notable being:

- the possibility to tune the fuel in a flexible manner (for example, hydrogen, natural gas, biogas, methanol, dimethyl ether and ammonia)
- the wide operating temperature range, that goes from 400-600°C for gadolinium-doped ceria (GDC) electrolytes to 650-950°C for strontium and magnesium-doped lanthanum gallate (LSGM) [15,16]; due to the high working temperatures, PGMs catalysts are not required

Moreover, SOFC attractiveness comes also from their capability to be used in the reverse way, and so to produce hydrogen from water electrolysis using the excess of electric energy: ideally this device, the so-called Reverse Solid Oxide Cell (R-SOC), has the opposite working principle of the SOFC. [17] Solid Oxide Electrolysis Cells (SOEC) present some advantages over the standard electrolysers, such as their low internal resistances, that allow high production rates at low voltages, the high energy

payback ratio and high efficiency for electrolytic hydrogen production and also the high purity of the produced hydrogen. These devices are also useful from the pollutants point of view for two main reasons; in fact, they would possibly replace the actual way to produce hydrogen via methane steam reforming, thus reducing the vicious cycle of pollutants emission, and they can be used for the co-electrolysis of CO_2 with steam, allowing the possibility to produce C-based chemicals. [18]

1.3.1 Historical background

The solid oxide fuel cell was first conceived following the discovery of solid oxide electrolytes in 1899 by Nernst, [14,19] who reported that the conductivity of pure metal oxides rose only very slowly with temperature and remained only relatively low, whereas mixtures of metal oxides can possess dramatically higher conductivities. This result was in complete agreement with the behaviour of liquid electrolytes. Many mixed oxides which exhibit high conductivity at elevated temperatures were quickly identified, including the particularly favourable composition 85% zirconium oxide and 15% yttrium oxide (YSZ), patented by Nernst in 1899. In 1905 Haber filed the first patent on fuel cells with a solid electrolyte composed by glass and porcelain, while using platinum and gold as the electrode materials. [14,20] In 1916 Baur and Treadwell filed a patent on fuel cells with metal oxides as the electrodes and ceramic solids with salt melts in the pores as the electrolyte. It was not until 1935 that Schottky suggested that YSZ could be used as a solid fuel cell electrolyte. In 1943 Wagner recognised the existence of vacancies in the anion sublattice of mixed oxide solid solutions and hence explained the conduction mechanism of the Nernst device. Baur and Preis subsequently went on to demonstrate the solid oxide (or ceramic) fuel cell with an yttria-stabilised zirconia electrolyte, successfully running their cell at 1000 °C. [14,20] Lately, the focus of the research on SOFCs is on lowering the operating temperatures.

1.3.2 Cell components: the anode

The anode is the component of the fuel cell where the fuel oxidation reaction takes place and where the produced electrons are put in the external circuit. Thus, it is mandatory for the anodic material to have enough active sites to host this reaction. Although the oxidation of hydrogen is kinetically favoured in respect to the reduction of oxygen at the cathode side of the cell, the anode becomes particularly relevant assuming the use of different fuels, which may require special characteristics (e.g., avoiding catalyst poisoning by coke in the case of carbon-containing fuels).

From the theoretical point of view, it is desirable to have an anode material with the following characteristics [21]:

- High electrical conductivity
- Good ionic conductivity
- Thermal expansion coefficient matching the electrolyte
- Chemical compatibility with the electrolyte
- Good adhesion to the electrolyte
- Capacity to prevent coke formation at the active site, mandatory for C-containing fuels
- High porosity, in order to have a better gas diffusion

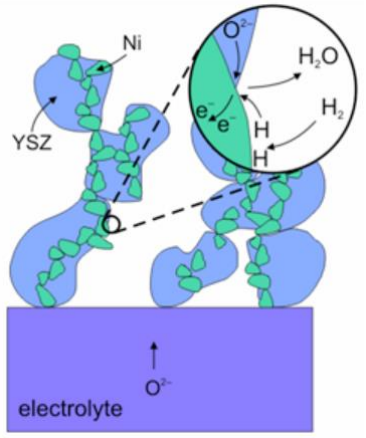

Figure 1.6: oxidation reaction on the surface of an anode made of Ni-YSZ. [22]

The state-of-the-art material is a cermet made of Ni and YSZ, as nickel alone is quite cheap and exhibits good electrochemical performances but its adhesion to the electrolyte is problematic, so it needs a ceramic material as support. This material is also useful to avoid the sintering between nickel particles and to have a thermal expansion coefficient that is the more similar to the electrolyte one; moreover, this material is known to have a good porosity (20-40%) and good conductivity, both ionic and electronic. [23,24] However, it is not a drawback-free material, as Ni particles aggregate and eliminate the triple-phase boundary (TPB) reducing the porosity of the anode and thereby decreasing cell performance at high temperatures. [25] Furthermore there are some losses due to the ohmic polarization at the interface electrode-electrolyte.

The research has later moved to novel ceramic materials, characterized by having a good conductivity, both ionic and electronic, the so-called Mixed Ionic and Electronic Ceramics (MIECs). Examples of these materials are Cu-CGO, Ni-CGO, Cu-Ni-CGO. [25] The real advantage of using MIEC materials is their ability to enlarge the Triple Phase Boundary (TPB) between fuel, anode and electrolyte. [13]

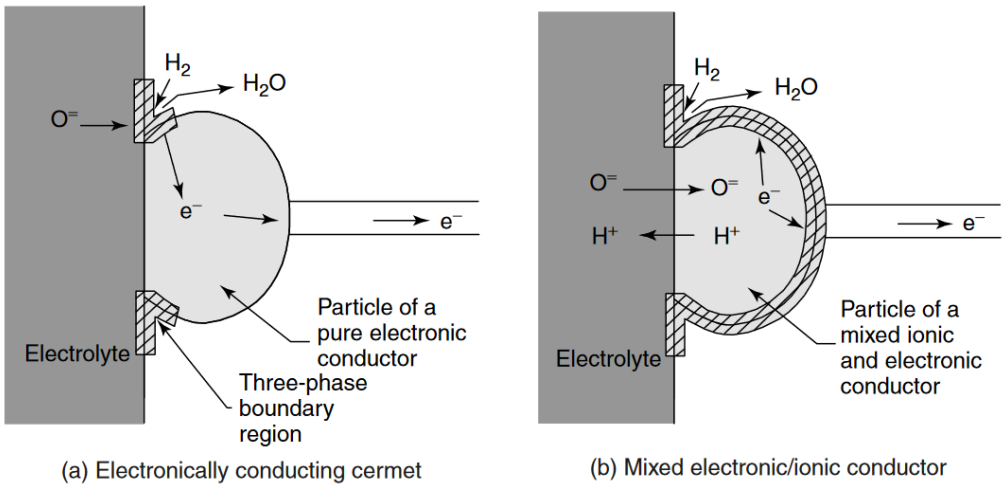

Figure 1.7: illustration of the three-phase boundary regions of different SOFC anode materials.

1.3.3 Cell components: the cathode

The cathode is the side of the cell where the oxygen reduction reaction takes place; this reaction is, usually, the rate-determining step of the cell working procedure, and thus it is mandatory for the materials used to this aim to have a good TPB regions. Taking into account that the non-stoichiometry and the defects of oxygen have a great effect on ionic and electronic transport properties of the material, perovskite-based materials are a suitable option for the cathode.

The state-of-the-art materials are A-doped lanthanum manganite, $La_{1-x}A_xMnO_3$, where A is a divalent cation. In this particular case, the effect of the dopants is to oxidize the manganese ion, increasing the electron-hole concentration and improving the electrical conductivity; dopant in A-site can, in principle, also contribute to the ionic conductivity. Among the possible dopants (Sr^{2+}, Ca^{2+} or others), Sr is the most used due to its size, similar to that of La. It is noteworthy that the linear increase of the electronic conductivity of LSM increasing the concentration of Sr^{2+}; this effect is present until a concentration of 50% mol, then the opposite effect starts to happen. [26]

The principal drawback of LSM is the interaction with YSZ at high temperature to form the isolating phase $La_2Zr_2O_7$ (LZ) at the interface, thus lowering the performances of the cell; moreover, the Sr concentration should not exceed the value of 30% mol, in order to avoid the formation of $SrZrO_3$ (SZ) from the interaction with the electrolyte. [26]

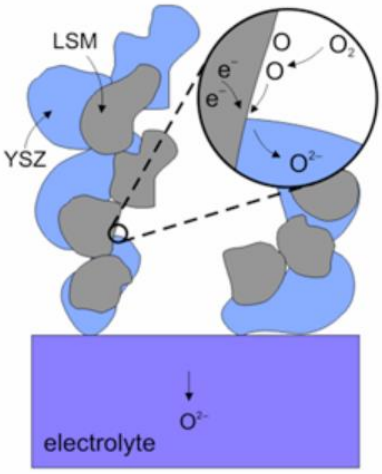

Figure 1.8: reduction reaction on the surface of a cathode made of LSM-YSZ. [22]

However, LSM materials cannot be used at temperatures below 800°C, due to the increasing cathode polarization while lowering the temperature and to the absence of oxygen vacancies, that restricts the reduction of oxygen to the TPB regions. [26] Consequently, two approaches were used to address this problem:

- Adding a second ionically conducting phase to LSM, extending the area where the oxidation of the oxygen can occur;
- Doping the LSM with a cation that can promote the formation of oxygen vacancies when Sr is used to dope the A-site.

1.3.4 Cell components: the electrolyte

The electrolyte, the middle part of the cell, should ensure to the device an optimal ionic conductivity while its electronic conductivity must be kept as low as possible to avoid leakage currents and thus worst overall performances.

The working temperature is a relevant variable in SOFCs operations, as the higher it is, the better will be the oxygen transportation and thus the performance; the lower limit is considered to be 600°C, at which the resistance related to oxygen transportation is no more negligible. [27]

The most known electrolyte materials are:

- Yttria-Stabilized Zirconia (YSZ), usually composed by zirconia (ZrO_2) doped with 8 to 10% mol of yttria (Y_2O_3); the result is a ceramic material stable both in oxidizing and reducing

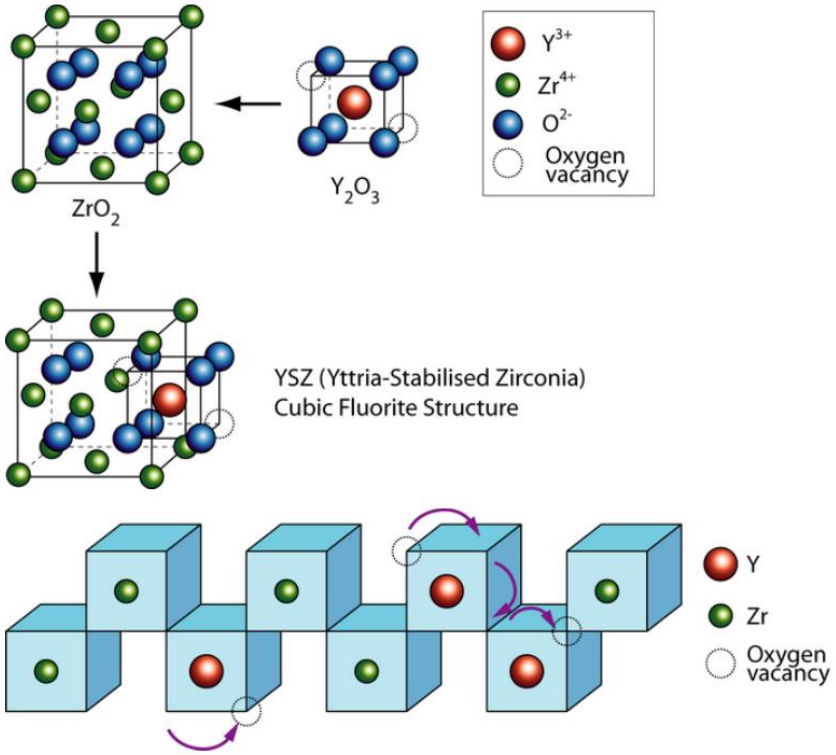

Figure 1.9: crystalline structure of YSZ (above) and oxygen transportation through vacancies (below).

environment. YSZ has an anionic conductivity: O^{2-} can be conducted through the material thanks to the fluorite crystal structure of zirconia in which some of the Zr^{4+} ions are replaced with Y^{3+} ions, resulting in some vacancies of oxide-ions in the structure. Oxide-ion transport occurs between those vacancies that are located at the tetrahedral sites. The ionic conductivity of YSZ at high temperatures is comparable with that of liquid electrolytes (0.1 S cm^{-1} at 1000°C). The main issue is the high ohmic losses related to the thickness of the electrolyte. A possible solution could be the reduction of the dimensions of the material; in that case, however, a small amount of alumina should be added to improve YSZ mechanical stability, that otherwise will not be enough to support the entire cell.

- Cerium Oxide, usually doped with trivalent cation (*Figure 1.10*) in order to suppress the oxygen vacancy ordering, consequent to the presence of the Ce (III)/Ce (IV) redox couple, thereby lowering the activation energy (E_a) and improving oxide ion conductivity at intermediate temperatures, that results, in fact, higher than the YSZ one; the most common dopants are Gd(III) (GDC) or Sm(III) (SDC), but relatively few investigations have been done using ceria based material, especially under electrolysis mode, possibly due to the partial reduction of Ce^{4+} to Ce^{3+} under operation. [28]

Another possibility is the doping with La (III) (LDC), which ion conductivity is higher than the standard ceria-doped materials' one; in particular, it has been seen that a percentage between 5 and 20% in lanthanum can increase the ionic conductivity up to $6 \cdot 10^{-3}$ S cm^{-1}. [29]

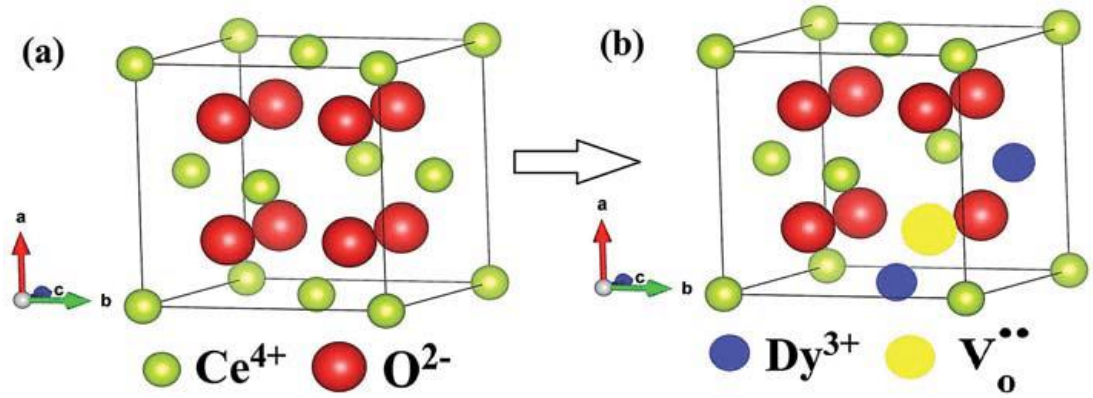

Figure 1.10: crystalline structure of Dy-doped ceria. [30]

- Strontium-Magnesium doped Lanthanum Gallate (LSGM), that in his composition $La_{0.8}Sr_{0.2}Ga_{0.8}Mn_{0.2}O_6$ presents an ionic conductivity at 800°C of the same magnitude order of YSZ at 1000°C.

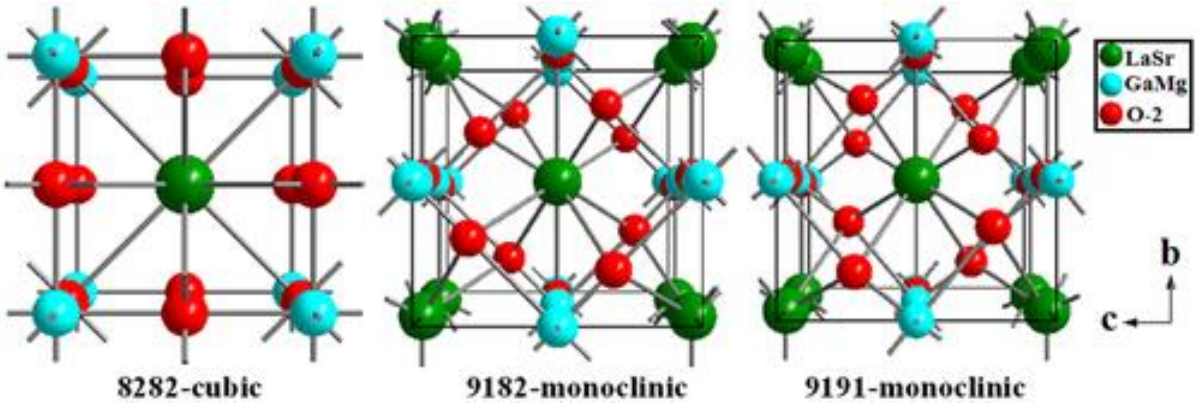

Figure 1.11: crystalline structure of LSGM. [31]

1.4 Reversible SOFCs

The reversible solid oxide fuel cell, usually abbreviated as R-SOFC, is an electrochemical device that can operate both as a fuel cell and as an electrolyser in an efficient way and inside a single unit. The SOEC can be seen as a SOFC that operates in the reverse mode, using nonetheless the same materials of the fuel cell from which it derives. In the electrolysis mode it operates by allowing a high temperature electrolysis that gives rise, for example, to hydrogen, if only water is supplied at the cell, or syngas, when the co-electrolysis with water and carbon dioxide takes place. The high temperatures are beneficial because they ensure a good ionic conduction through the electrolyte as well as a high electrolysis efficiency. Roundtrip efficiency is, in fact, as high as 55% if the heat generated from the fuel is re-used with the help of a thermal man-

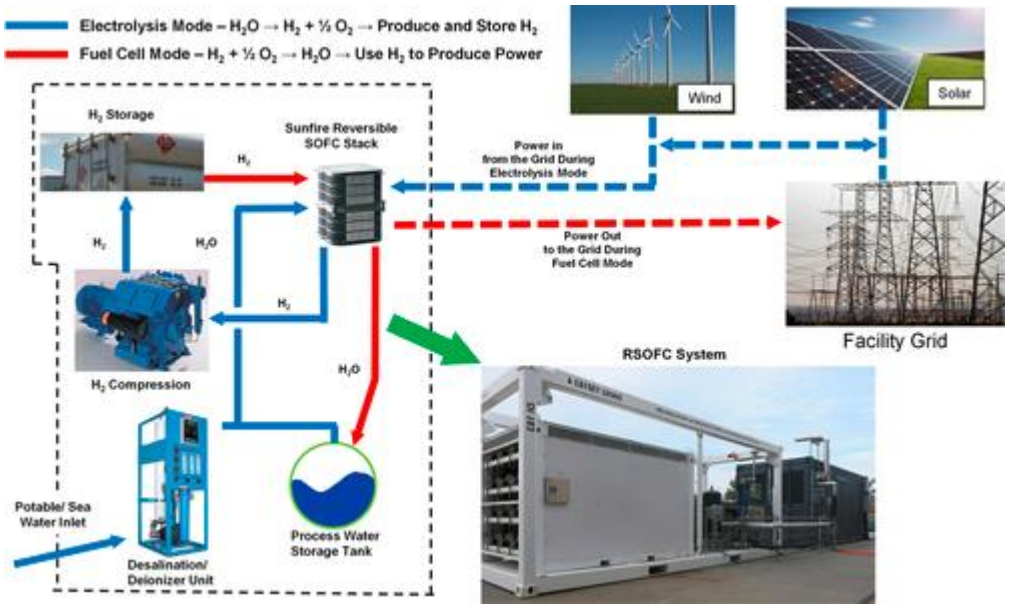

Figure 1.12: R-SOFC schematic representation. [32]

-agement process. Moreover, the R-SOFC system acts as an energy storage device to store the renewable energy into energy carriers, operating thus like a sort of battery and making this device a suitable approach to a sustainable energy system. As a manner of fact, recent works has shown that these cells might be an electric storage technology with a high roundtrip efficiency (>70%) and higher energy density than batteries. [33] Furthermore, the hydrogen produced can be used in the fuel cell itself, providing power when needed, with limitation due only by the stored hydrogen and not by the cell size.

Lastly, one of the great advantages of the R-SOFC is the fact that, by inverting the operational mode of the cell (from SOFC to SOEC and vice-versa) the effects of sulphur poisoning, carbon deposition

and delamination of the electrodes are decreased. The challenge is, however, finding materials that can work with a proper efficiency both in oxidizing and reducing environment.

The drawbacks associated with this technology are due to the thermal differences of the two operational modes: electrolysis is endothermic while the fuel cell has an exothermic process. Another issue is finding the operational condition that can permit good performances in both fuel cell and electrolyzer mode. Lastly, the reaction products are stored by compression to be used when the cell is reversed, so processes with a minimal energy waste are needed.

1.5 SOFCs challenges

The SOFC technology is a promising way to obtain energy in a clean and sustainable way, but many steps forward are needed to ensure its worldwide commercial diffusion. The state-of-the-art SOFC works only at high temperatures, it is expensive to produce and to sell, and consequently many efforts are necessary to obtain new materials that can decrease the working temperature as well as the production costs without affecting the performances and structural stability of the device.

A possible solution could be the study of new two-phases materials, with a nano-composition, thus permitting, for example, to lower the ohmic losses of the cell. Some studies have indeed shown that the two-phase nanocomposite approach can create a wide range of functional materials, as long as the selected two appropriate phases can create desired functions at interfaces. [34]

Another possible solution is the study of infiltration and impregnation of the state-of-the-art materials with dopants that can affect the conductivity of the materials.

In the past years, one of the biggest breakthroughs in developing new SOFCs technologies with lower operating temperature but still high power densities, was the development of anode supported cells. Thus, finding new supports that can enhance the performance of the electrode material could be a possible improvement. [35]

References

1 X. Li, *Principles of Fuel Cells*, CRC Press, 2005.

2 S. M. Haile, Materials for fuel cells, *Materials Today*, 2003, **6**, 24–29.

3 *The Fuel Cell Industry Review 2021*, E4Tech, 2022.

4 X. Wang, J. Zhu and M. Han, Industrial Development Status and Prospects of the Marine Fuel Cell: A Review, *JMSE*, 2023, **11**, 238.

5 M. Latapí, B. Davíðsdóttir and L. Jóhannsdóttir, Drivers and barriers for the large-scale adoption of hydrogen fuel cells by Nordic shipping companies, *International Journal of Hydrogen Energy*, 2023, **48**, 6099–6119.

6 R. Caponi, A. Monforti Ferrario, L. Del Zotto and E. Bocci, Hydrogen refueling stations and fuel cell buses four year operational analysis under real-world conditions, *International Journal of Hydrogen Energy*, 2023, **48**, 20957–20970.

7 M. W. Ellis, M. R. Von Spakovsky and D. J. Nelson, Fuel cell systems: efficient, flexible energy conversion for the 21st century, *Proceedings of the IEEE*, 2001, **89**, 1808–1818.

8 M. Neergat and A. K. Shukla, A high-performance phosphoric acid fuel cell, *Journal of Power Sources*, 2001, **102**, 317–321.

9 A. Kirubakaran, S. Jain and R. K. Nema, A review on fuel cell technologies and power electronic interface, *Renewable and Sustainable Energy Reviews*, 2009, **13**, 2430–2440.

10 A. Hamnett, Mechanism and electrocatalysis in the direct methanol fuel cell, *Catalysis Today*, 1997, **38**, 445–457.

11 A. Heinzel and V. M. Barragán, A review of the state-of-the-art of the methanol crossover in direct methanol fuel cells, *Journal of Power Sources*, 1999, **84**, 70–74.

12 A. L. Dicks, Molten carbonate fuel cells, *Current Opinion in Solid State and Materials Science*, 2004, **8**, 379–383.

13 J. Larminie and A. Dicks, *Fuel cell systems explained*, J. Wiley, Chichester, West Sussex, 2nd ed., 2003.

14 R. M. Ormerod, Solid oxide fuel cells, *Chem. Soc. Rev.*, 2003, **32**, 17–28.

15 H. Shi, C. Su, R. Ran, J. Cao and Z. Shao, Electrolyte materials for intermediate-temperature solid oxide fuel cells, *Progress in Natural Science: Materials International*, 2020, **30**, 764–774.

16 M. Morales, J. J. Roa, J. Tartaj and M. Segarra, A review of doped lanthanum gallates as electrolytes for intermediate temperature solid oxides fuel cells: From materials processing to electrical and thermo-mechanical properties, *Journal of the European Ceramic Society*, 2016, **36**, 1–16.

17 M. B. Mogensen, M. Chen, H. L. Frandsen, C. Graves, J. B. Hansen, K. V. Hansen, A. Hauch, T. Jacobsen, S. H. Jensen, T. L. Skafte and X. Sun, Reversible solid-oxide cells for clean and sustainable energy, *Clean Energy*, 2019, **3**, 175–201.

18 M. Torrell, S. García-Rodríguez, A. Morata, G. Penelas and A. Tarancón, Co-electrolysis of steam and CO_2 in full-ceramic symmetrical SOECs: a strategy for avoiding the use of hydrogen as a safe gas, *Faraday Discuss.*, 2015, **182**, 241–255.

19 W. C. Heraeus, Über die elektrolytische Leitung fester Körper bei sehr hohen Temperaturen, *Z. Elektrotech. Elektrochem.*, 1899, **6**, 41–43.

20 H.-H. Möbius, On the history of solid electrolyte fuel cells, *Journal of Solid State Electrochemistry*, 1997, **1**, 2–16.

21 J. Fergus, Oxide anode materials for solid oxide fuel cells, *Solid State Ionics*, 2006, **177**, 1529–1541.

22 Fuel Cells (all content), https://www.doitpoms.ac.uk/tlplib/fuel-cells/printall.php.

23 L. J. M. J. Blomen and M. N. Mugerwa, *Fuel Cell Systems*, Springer Science & Business Media, 2013.

24 B. Shri Prakash, S. Senthil Kumar and S. T. Aruna, Properties and development of Ni/YSZ as an anode material in solid oxide fuel cell: A review, *Renewable and Sustainable Energy Reviews*, 2014, **36**, 149–179.

25 S. P. S. Shaikh, A. Muchtar and M. R. Somalu, A review on the selection of anode materials for solid-oxide fuel cells, *Renewable and Sustainable Energy Reviews*, 2015, **51**, 1–8.

26 C. Sun, R. Hui and J. Roller, Cathode materials for solid oxide fuel cells: a review, *J Solid State Electrochem*, 2010, **14**, 1125–1144.

27 M. Biswas and K. Sadanala, Electrolyte Materials for Solid Oxide Fuel Cell, *Journal of Powder Metallurgy & Mining*, DOI:10.4172/2168-9806.1000117.

28 G. Cai, A. L.-S. Eh, L. Ji and P. S. Lee, Recent Advances in Electrochromic Smart Fenestration, *Advanced Sustainable Systems*, 2017, **1**, 1700074.

29 N. Momin, J. Manjanna, L. D'Souza, S. T. Aruna and S. Senthil Kumar, Synthesis, structure and ionic conductivity of nanocrystalline $Ce_{1-x}La_xO_{2-\delta}$ as an electrolyte for intermediate temperature solid oxide fuel cells, *Journal of Alloys and Compounds*, 2022, **896**, 163012.

30 D. L. Maricle, T. E. Swarr and S. Karavolis, Enhanced ceria - a low-temperature SOFC electrolyte.

31 J. Yu, H. Liu, X. Chen, J. Xing, B. Yuan, M. Wang and W. Ma, Ionic conductivity and crystal structure of LSGM with different element mole ratios, *Fuel Cells*, 2021, **21**, 149–154.

32 J. Mermelstein and O. Posdziech, Development and Demonstration of a Novel Reversible SOFC System for Utility and Micro Grid Energy Storage, *Fuel Cells*, 2017, **17**, 562–570.

33 P. Di Giorgio and U. Desideri, Potential of Reversible Solid Oxide Cells as Electricity Storage System, *Energies*, 2016, **9**, 662.

34 B. Zhu, Solid oxide fuel cell (SOFC) technical challenges and solutions from nano-aspects, *International Journal of Energy Research*, 2009, **33**, 1126–1137.

35 E. D. Wachsman and S. C. Singhal, Solid Oxide Fuel Cell Commercialization, Research, and Challenges, *Electrochem. Soc. Interface*, 2009, **18**, 38.

36 A. S. Bhalla, R. Guo and R. Roy, The perovskite structure—a review of its role in ceramic science and technology, *Materials Research Innovations*, 2000, **4**, 3–26.

2. Perovskite Materials

Perovskite oxide materials represents nowadays the state-of-the-art materials for electrodes in a solid oxide fuel cell, but their history is not so recent. In fact, their first discover is dated back in 1839, when Gustav Rose found a calcium titanium oxide mineral of formula $CaTiO_3$ in the Ural Mountains, naming it after the Russian mineralogist Lev Perovski. Since then, the materials that present the same crystal structure were named perovskites. [1]

2.1 Crystalline structure

The general structure of these material is ABO_3, where A and B are two different cations. The cell can accommodate many different chemical species (it is possible to accommodate inside the structure almost all the metals in the periodic system), giving to the perovskite materials different properties, useful in different applications.

The crystal structure of these materials consists of corner sharing octahedra of formula BO_6 where the A cation occupies the 12-fold coordination site formed in the middle of the cube of eight octahedra. It is noteworthy that the ideal cubic perovskite is not common in nature and the mineral perovskite is itself slightly distorted; this is principally due to size effects, deviations from the ideal composition and the Jahn-Teller effect. [2]

The size effect is related to the ionic radii of all the elements of which the material is composed. The cell axis (a), in fact, is described by the equation:

$$a = \sqrt{2}(r_A + r_O) = 2(r_B + r_O) \tag{2.1}$$

where r_A, r_B and r_O are, respectively, the ionic radii of the A-cation, B-cation and oxygen ion. Their effect on the structural distortion is given by the Goldschmidt tolerance factor (t):

$$t = \frac{r_A + r_O}{\sqrt{2}(r_B + r_O)} \tag{2.2}$$

The ideal cubic perovskite, strontium titanate ($SrTiO_3$), is characterized by a tolerance factor of 1.00, since r_A = 1.44 Å, r_B = 0.605 Å and r_O = 1.40 Å. [3]

If the A ion is smaller than the ideal value, then t becomes smaller than 1. As a result, the BO_6 octahedra will tilt in order to fill the space. However, the cubic structure occurs if $0.89 < t < 1$. Lower

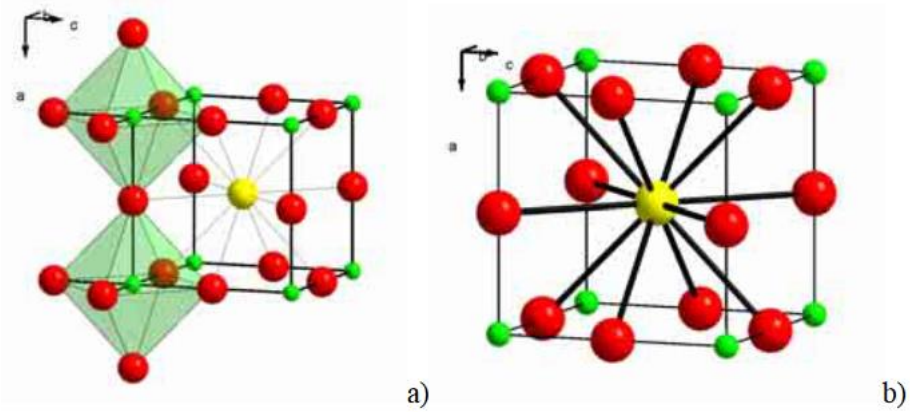

Figure 2.1: Outline of the ideal cubic perovskite structure $SrTiO_3$ that has (a) a three-dimensional net of corner sharing $[TiO_6]$ octahedra with (b) Sr^{2+} ions in the twelve-fold cavities in between the polyhedra.

values of t will lower the symmetry of the crystal structure. On the other hand, if t is larger than 1 due to a large A or a small B ion, then hexagonal variants of the perovskite structure are stable. [2]

The change in composition can be the result of a thermal treatment in an oxidizing or reducing atmosphere, that causes the change in oxygen content of the entire structure. As a result, a defective perovskite can be produced, characterized by different properties with respect to the stoichiometric one.

The Jahn-Teller effect is due to some active ions in the B site. This effect is a mechanism of spontaneous symmetry breaking in both solid state and molecular systems. The odd number of electrons in the e_g orbital causes an elongation of the BO_6 octahedra to decrease symmetry. [2]

2.2 Perovskite properties

The perovskite family presents a number of appealing properties. From the electronic point of view, these materials are mostly showing dielectric and ferroelectric properties, thanks to the easy chemical manipulation in the composition. Magnetism is observed in perovskites with transition metal ions (TMI) with unfilled 3d orbitals.

The superconductivity of some perovskites depends on super exchange and electronic correlations restricted to a two-dimensional, weakly doped plane. The crystal structure of the prototype and perovskite related compound is $YBa_2Cu_3O_{7-x}$.

From the operational point of view, it is possible to tune the properties of these materials by using specific elements in the B or A site of a perovskite: combinations of cobalt and iron can be placed on

the B sites, leading to different degrees of electronic conduction, ranging from metallic-like narrow-band conduction of pure Co to small-polaron conduction for Fe-based compositions.

The perovskites conductivity and stability properties are then ideal for SOFC electrode applications. Nonetheless, there are some challenges that still have to be overcome. For example, the working temperature of the cells should be lowered, thus resulting in a higher thermodynamic efficiency and better flexibility in the choice of materials, consequently lowering the overall costs and increasing the performances. [4] High temperatures are also the cause of the mismatch of thermal expansion coefficient between the electrode and the electrolyte; the possible consequences are ohmic losses and structural stability issues. [5]

Perovskites can be also used as electrolytes; for this aim, several requirements are needed, as fast ionic transport, negligible electronic conduction, mechanical and thermodynamic stability over a wide range of temperature and oxygen partial pressure, no volatilization of components and negligible interaction with electrode materials under operation conditions. [6]

2.3 Double perovskite materials

Double perovskite materials are the result of an ordered rock-salt-like arrangement of corner-sharing BO_6 and $B'O_6$ units in the crystal structure, with formula $A_2BB'O_6$ or $AA'BB'O_6$ and large amount of oxygen non-stoichiometry accommodated in the structure.

In the case of an A^{2+} cation, the total oxidation state of the B site will be four, which can also be adapted for B^{4+}/B^{4+}, B^{3+}/B^{5+}, B^{2+}/B^{6+}, and B^{+}/B^{7+}.

For pure perovskite structures, the relative size of the A and B site cations determines the stability of the perovskite slab. The A-O bond length is equal to √2 and B-O is normally 40% smaller than A-O bond length. In the case of double perovskites, the Goldschmidt tolerance factor (t) can be described by:

$$t = \frac{r_A/2+r_O}{\sqrt{2}[(r_B+r_{B'})/2+r_O]} \tag{2.3}$$

In $A_2^{2+}BB'O_6$, the A-site cation can affect only the volume of the unit cell, but the B-site cation involves the perovskite structure and space group. For the double perovskite structure, the B′ cation radii mismatch is very substantial. [7]

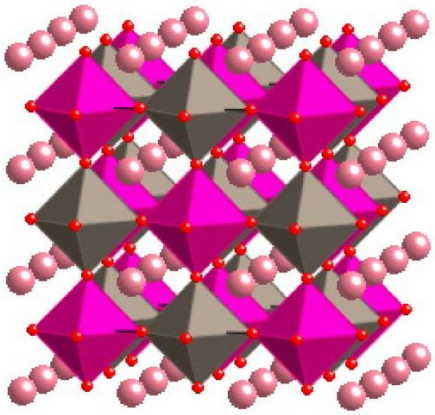

Figure 2.2: ideal 1:1 double perovskite in cubic symmetry (space group Fm-3m, a =$2a_p$).

It is also possible to obtain a layered structure if B and B′ can alternate in opposite direction, resulting in a monoclinic structure like the one of La_2CuSnO_6. [8] Layered type double perovskites with a large number of oxygen vacancies have been proved to be good electrode materials for the SOFC. Recent research focuses on lanthanide (Ln)-containing oxide materials doped with alkaline elements (Ba, Sr, Ca, etc.) and transition metals (Cr, Mn, Fe, etc.). Hence, their good mixed electronic and ionic conducting behaviour are recognized as very promising for electrode materials. However, these materials still exhibit slow oxygen transportation kinetics, specifically at intermediate temperatures.

Most of the double perovskite materials show insulating or semiconducting behaviour, as described in literature. The electronic conductivity of double perovskite materials depends mainly on the B-site cation ordering. Almost all the transition metals occupy the B-site, allowing to reach very interesting ionic and/or electrically conductive properties. The real challenge is to identify a good stable electrode material exhibiting a high conductivity in a reducing atmosphere for SOFCs operation.

Some of the double perovskite materials have recently been studied as anodes in SOFCs thanks to their flexibility in fuel utilisation and tolerance to impurities. It is, in fact, the case of $Sr_2Mg_{1-x}Mn_xMoO_6$ (SMMO) double perovskite family, that has been investigated by previous literature works that are the benchmark for this thesis, as it presents high activity toward oxidation of both hydrogen and methane, meaning that the system could easily switch and adapt to different composition in gas mixture as it can happen if the SOFC system is fuelled by biogas. Moreover, it has been observed a good tolerance to sulfur impurities, that are very common to find in gas mixture obtained by bio-fermentation processes (up to 50 ppm) with negligible degradation over 50 working cycles, resulting in cheaper manufacturing, as de-sulfurization is not mandatory, and more durable devices. [9,10]

References

1 A. S. Bhalla, R. Guo and R. Roy, The perovskite structure—a review of its role in ceramic science and technology, *Materials Research Innovations*, 2000, **4**, 3–26.

2 M. Johnsson and P. Lemmens, in *Handbook of Magnetism and Advanced Magnetic Materials*, eds. H. Kronmüller and S. Parkin, Wiley, 1st edn., 2007.

3 M. Kar, Electronic and optical properties of $SrTiO_3$ perovskite using semi-local and hybrid first principles density functional theory.

4 N. Bonanos, K. S. Knight and B. Ellis, Perovskite solid electrolytes: Structure, transport properties and fuel cell applications, *Solid State Ionics*, 1995, **79**, 161–170.

5 S. J. Skinner, Recent advances in Perovskite-type materials for solid oxide fuel cell cathodes, *International Journal of Inorganic Materials*, 2001, **3**, 113–121.

6 V. A. Kolotygin, E. V. Tsipis, A. L. Shaula, E. N. Naumovich, J. R. Frade, S. I. Bredikhin and V. V. Kharton, Transport, thermomechanical, and electrode properties of perovskite-type $(La_{0.75-x}Sr_{0.25+x})_{0.95}Mn_{0.5}Cr_{0.5-x}Ti_xO_{3-d}$ (x=0-0.5), *J Solid State Electrochem*, 2011, **15**, 313–327.

7 S. Afroze, A. Karim, Q. Cheok, S. Eriksson and A. K. Azad, Latest development of double perovskite electrode materials for solid oxide fuel cells: a review, *Front. Energy*, 2019, **13**, 770–797.

8 M. T. Anderson and K. R. Poeppelmeier, Lanthanum copper tin oxide (La_2CuSnO_6): a new perovskite-related compound with an unusual arrangement of B cations, *Chem. Mater.*, 1991, **3**, 476–482.

9 Y.-H. Huang, R. I. Dass, J. C. Denyszyn and J. B. Goodenough, Synthesis and Characterization of Sr_2MgMoO_6, *J. Electrochem. Soc.*, 2006, **153**, A1266.

10 Y.-H. Huang, R. I. Dass, Z.-L. Xing and J. B. Goodenough, Double Perovskites as Anode Materials for Solid-Oxide Fuel Cells, *Science*, 2006, **312**, 254–257.

3. Synthesis and Characterization of SMMO materials

The following chapter will be dedicated to the description of the main synthesis routes to obtain double perovskite materials, with a focus on the approach that has been used in this work, the so-called Pechini route.

Subsequently, all the characterization techniques performed on the obtained powders (XRD, H_2-TPR, SEM, EDX and XPS) will be presented and discussed.

3.1 Main synthesis routes

Double perovskites are usually prepared with the same approaches commonly used for the synthesis of perovksites, that can be divided in solid state or wet chemistry synthesis.

3.1.1 Solid state synthesis

In the solid-state synthesis method, the metal precursors are in the form of carbonates and oxides. The reaction is carried out by alternating thermal treatments at high temperature and mechanical grinding and mixing, usually done by ball milling. The desired phase is ultimately achieved by alternating repetitively these treatments until the target material is fully acquired.

This kind of treatment is easy to perform and relatively cheap, but the presence of the impurities inside the materials is difficult to control. Moreover, it is difficult to reach a good homogeneity of the final product.

3.1.2 Wet chemistry synthesis

Unlike the solid-state synthesis, the wet chemistry one involves a solution in which the cations composing the perovskite are dissolved and the precipitation of the precursor is induced by pH or temperature changes. This method is usually carried out in water, thus only water-soluble precursors as nitrates or acetates can be used.

The advantages of the wet chemistry approach over the solid-state one is a better control on the precursors that lead to a more homogeneous product, characterized by the exact desired stoichiometry.

One renowned wet chemistry method to synthesize perovskites is the sol-gel route, that allows to achieve a better homogeneity and crystal purity at lower temperatures, thanks to the homogeneous

distribution of the cations in the solution obtained by using complexing agents; the most common are citric acid, glycine and EDTA. The main difference among the sol-gel methods stands mostly on the complexing agent used.

3.2 The Pechini method

All the four materials (x=0, 0.2, 0.5, 1) have been synthesised by using the Pechini method, implying the use of citric acid ($C_6H_8O_7$) and ethylene glycol ($C_2H_6O_2$) as chelating agents. [1] Citric acid is particularly suitable for this aim due to the fact that it is a weak organic acid with three carbonyl groups that can act as anchoring points for cations, while the use of ethylene glycol results in a highly cross-linked gel containing a more uniform distribution of the reacting cations. The gel structures can be varied depending on the acid-to-alcohol ratio. [2] The main advantages in using this synthesis route stand in the temperature, as the organic components are eliminated as low as at 300°C, and in its relatively low cost. [3]

In this work, the used metal precursors were:

- $Sr(NO_3)_2$, Sigma Aldrich, >99%
- $Mg(OH)_2$, Sigma Aldrich, >95%
- $Mn(CH_3CO_2)_2 \cdot 4H_2O$, Sigma Aldrich, >99%
- $(NH_4)_6Mo_7O_{24} \cdot 4H_2O$, Sigma Aldrich, >99%

These compounds were solubilized separately in water keeping the solutions at 125°C and under continuous stirring, with the help of some drops of nitric acid in the case of magnesium hydroxide, and put in the same becker, together with citric acid and ethylene glycol, once the dissolution has taken place; it is noteworthy that the ideal ratio between cations, citric acid and ethylene glycol has been found to be 1:1.9:6 from previous attempted synthesis. The minimum quantity of nitric acid should be used, in order to have a good dissolution but a solution that is not too acidic. This is necessary to ensure the complete dissolution of each of the precursors and avoid undesired precipitation phenomena. The all-in-one solution was subsequently basified to pH 7 via a drop-wise addition of ammonia, thus avoiding undesired precipitation of hydroxides (see *Figure 3.1*).

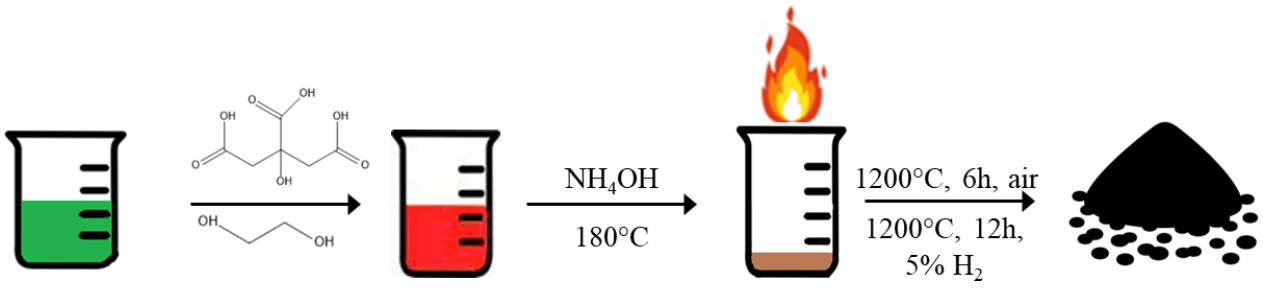

Figure 3.1: schematisation of the synthesis approach.

At that point, the stirring was stopped and the solution was heated to eliminate water and to induce the formation of a gel phase, that was later burnt through an auto-combustion process at about 350°C. Eventually, to eliminate residual organic compounds and to induce the formation of the right double perovskite phase, a calcination treatment at 1200°C for 6 hours and a reduction treatment at 1200°C for 12 hours, both with a heating and cooling ramp of 5°C/min, have been carried out. This sequence of treatments is mandatory to obtain the desired crystalline phase and porosity and also to avoid the formation of impurities, commonly observed in previous works. [4–7]

3.3 X-Ray Diffraction (XRD)

The XRD analysis were performed using a Brucker D8 Advance diffractometer with Bragg-Brentano geometry and a Cu Kα radiation (40 kV, 40mA, λ=0.154 nm). The data collecting was performed with 0.02°/step at a counting time of 0.35 s/step in the 2θ range from 20° to 80°. The crystalline phases were identified by search-match method using the Crystallography Open Database.

The following paragraphs will show the XRD patterns of the samples after the thermal treatment in two different atmospheres:

1. Air
2. Hydrogen

3.3.1 Air atmosphere

The first series of XRD pattern has been registered immediately after the calcination treatment of the SMMO materials; as previously said, the treatment was performed at 1200°C for 6 hours, with a temperature ramp of 5°C/min.

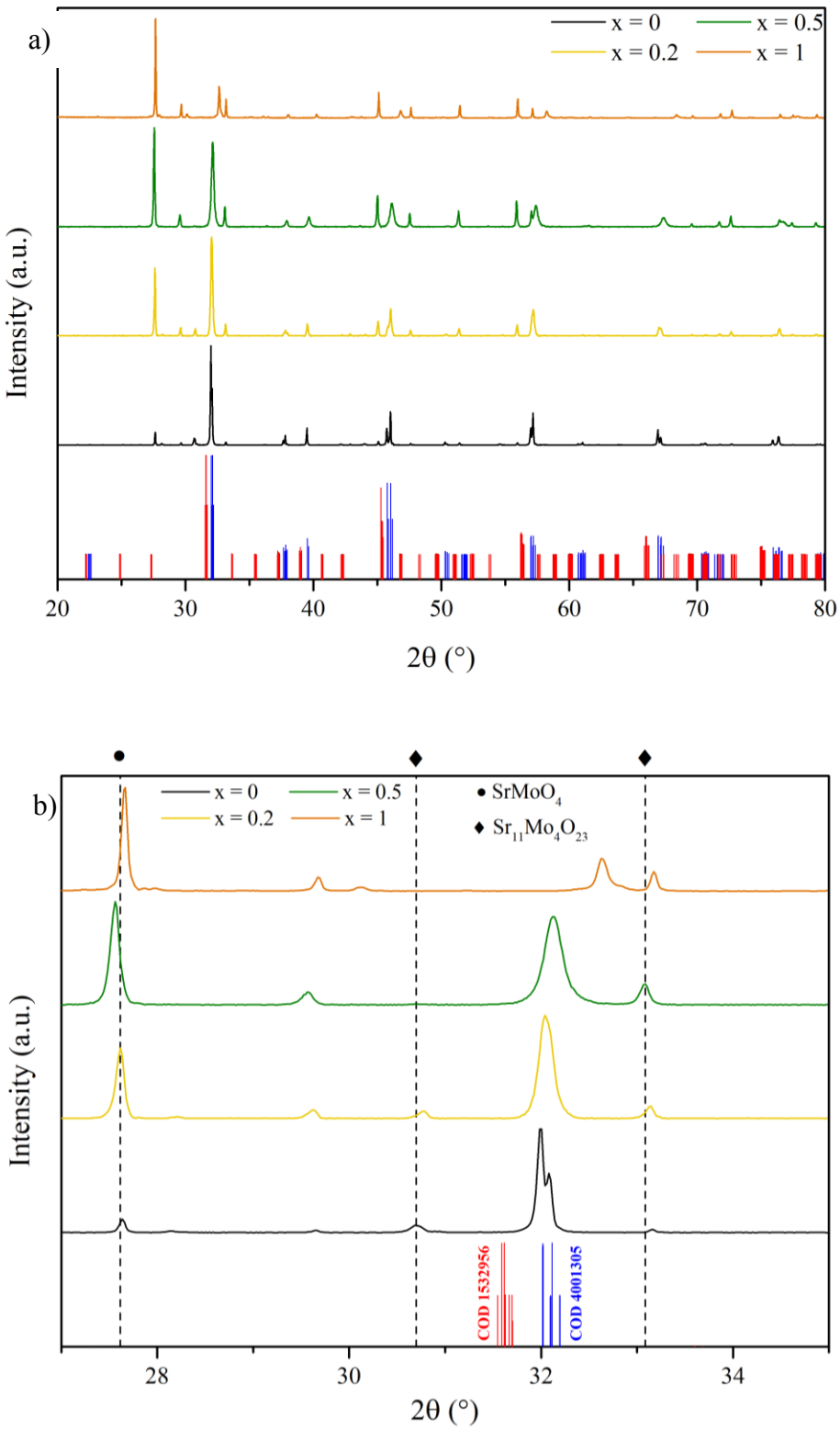

Diffractogram 3.1: (a) XRD diffractogram of the synthetised materials after the calcination treatment, with comparison to the relative CODs; (b) zoom on the spectral region containing the main reflexes, underlining the presence of impurities.

The resulting XRD pattern (see *Diffractogram 3.1*) has confirmed that the principal phases formed after the calcination treatment were the desired ones, as it can be visualised in *Diffractogram 3.1 (a)*. Nevertheless, the presence of two impurity phases is not negligible, and thay can easily be seen in *Diffractogram (b)*; in particular, the most relevant impurity phase is an insulating strontium molybdate, $SrMoO_4$, that is characteristic of this materials' family and commonly evinced in previous literature works. [6,8–10] Although strontium molybdate is known to be an insulating material, its presence is not always a drawback, as it helps avoiding the evaporation of molybdenum precursors at temperatures about 800°C, conferring thus thermal stability to SMMO compounds until temperatures about 1500°C; moreover, it can easily be reduced to $SrMoO_3$, a perovskite-like material known for relevantly contributing to the electro-catalytic activity due to its high electrical conductivity. [11]

The other impurity phase is $Sr_{11}Mo_4O_{23}$, a strongly defective double perovskite material which formula can be rewritten as $Sr_{1.75-\alpha}SrMoO_{6-\delta}$, thus with the presence of strontium cation both in A- and B-site. Going into detail, the presence of vacancies in the A-site generates a relevant ionic conductivity, already studied in literature. This double perovskite material can be obtained after a calcination treatment at 1200°C, but it is unstable under reducing atmosphere, thus limiting its applications as anode for SOFCs. [12]

Moreover, the search-match function of the XRD database has detected the presence of a third impurity, magnesium oxide, that cannot be visualised in the XRD patetrn as its relative intensity is low with respect to the main reflexes; this impurity is easily formed and is difficult to remove because temperatures above 2500°C are required to reduce magnesium oxide to its metallic form, that goes under oxidation very easily. [13]

Comparing the main reflexes with the reference from crystallography databases, it can clearly be seen that the reflexes of manganese-containing samples located at about 32° are shifted at higher angles. The main hypothesis is that this is due to the presence of manganese (IV), both in the form of impurities, whose presence has been confirmed by the XRD analysis and widely discussed previously, and inside the perovskitic structure, thus with a partial presence of molybdenum in a lower oxidation state (5^+, most likely); in fact, as confirmed by *Shannon*'s work, manganese cation presents a ionic radius of 0.83 Å when in sixfold coordination and in 2^+ oxidation state, while its ionic radius decreases to 0.53 Å when hexa-coordinated manganese is in 4^+ oxidation state, resulting in a shrinkage of the cell parameter and so in the shifting of the reflexes to higher angles. [14] The presence of manganese (IV) has been investigated with a series of H_2-TPR analyses, that will be discussed later in this work.

3.3.2 5% H2 atmosphere

Given the consideration presented in the last section, a thermal treatment in reducing atmosphere was found to be mandatory to limit the presence of undesired phases, thus increasing the desired materials' yield. Thus, subsequently to the thermal treatment in hydrogen-containing atmosphere, another XRD analysis has been carried out to verify the eventual residual impurity phases and the formation of the desired materials.

The resulting XRD has confirmed the presence of the desired perovskitic phases and the reduction of the majority of the spurious compounds, as it can be visualised in *Diffractogram 3.2 (a)*. Nevertheless, some impurities are still visible in *Diffractogram 3.2 (b)*. In particular, a slight presence of magnesium oxide can be identified, in agreement with the un-reducibility of this compound at the temperature at which the treatment has been carried out (not visualised as its relative intensity is too low in comparison to the principal phases).

Manganese (II) oxide has been found to be present has impurity on all $x \neq 0$ samples, with an increasing relative intensity, coherent with the increase in manganese content. This is counterintuitive if compared to literature consideration, as manganese (II) oxide is reported to be completely reduced at 341°C. [15] This compound is expected to decrease the efficiency of the device being an insulator. [16]

The diffractogram has shown the presence of an additional spurious phase, i.e strontium oxide, with a relative intensity that decreases with an increasing content in manganese. For this purpose, several works have shown strontium tendency to segregate in the material surface, in the form of carbonates, hydroxides and oxides in the first 10 nm of material depth, but the driving force of the segregation is still not well understood, as its role on electro-catalytic performances of the material. [17–20] In particular, strontium oxide has been found to be reduced above 1100°C thanks to the help of a reducing agent (like aluminium or silicon [21]), not present in the investigated samples. It is also possible to decrease by almost 50% the degree of strontium segregation by means of an etching step, both using reactive ions or solutions (of HF, for example). [19,20]

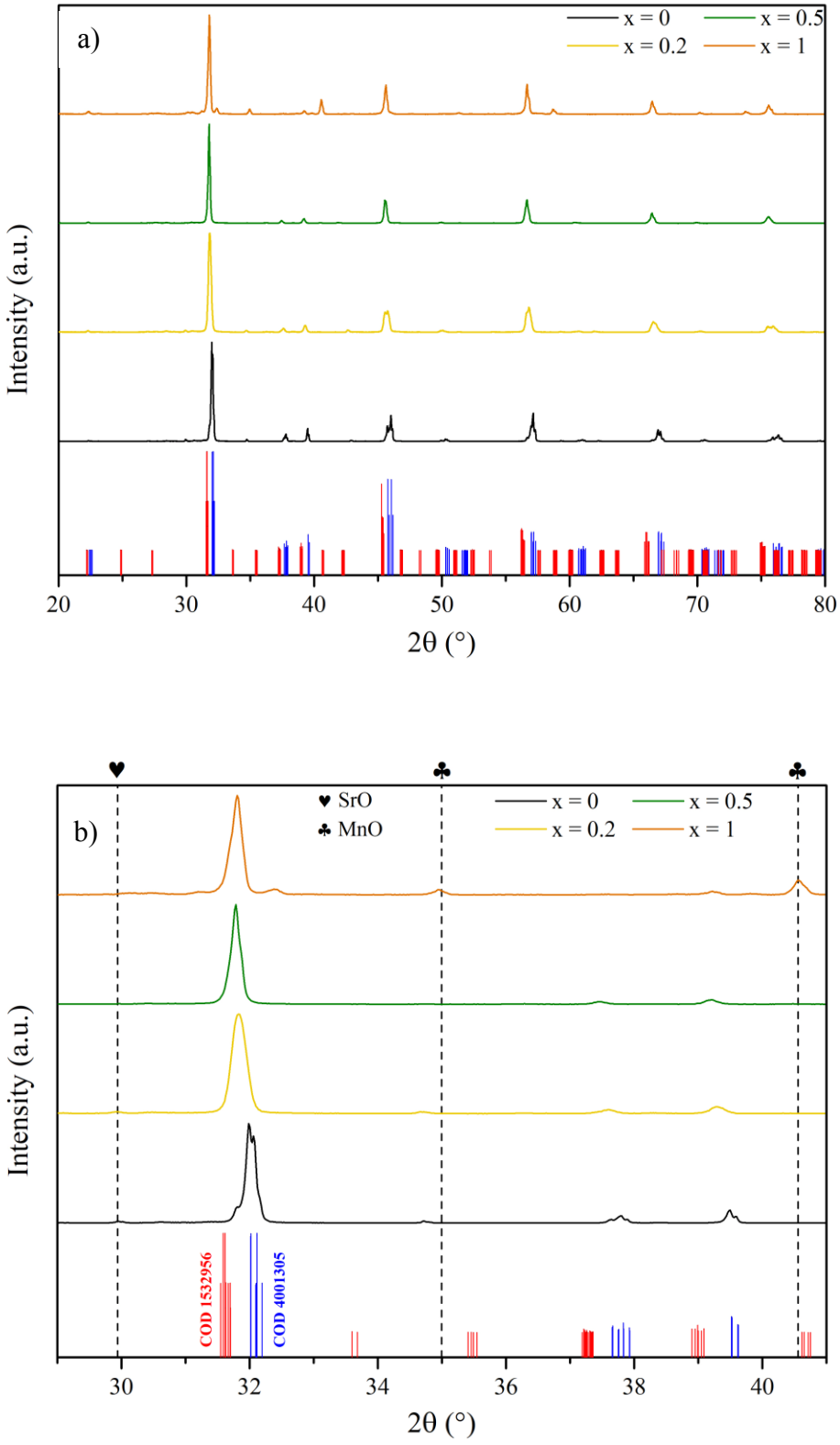

Diffractogram 3.2: (a) XRD diffractogram of the synthetised materials after the calcination treatment in a reducing atmosphere, with comparison to the relative CODs; (b) zoom on the spectral region containing the main reflexes, underlining the presence of impurities.

3.4 H_2 – Temperature Programmed Reduction (H_2 – TPR)

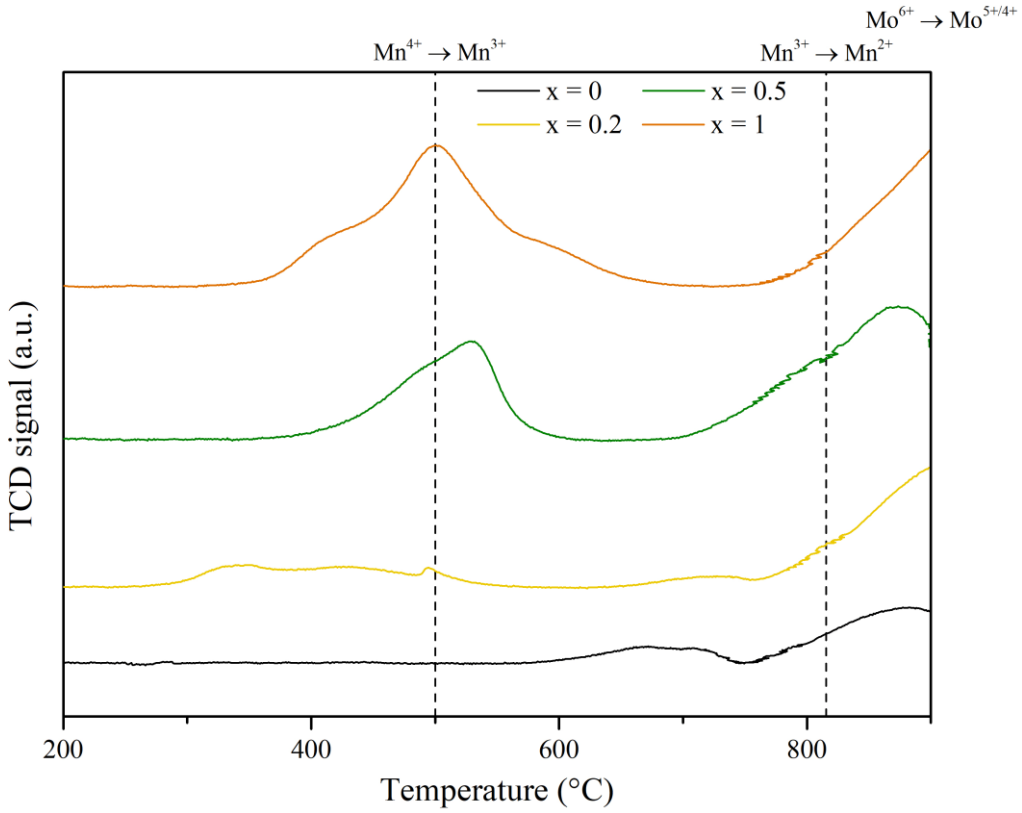

Graph 3.1: H_2 – TPR analysis of SMMO materials after the calcination treatment in air.

The Hydrogen-Temperature Programmed Reduction (H_2-TPR) analysis was performed using an Autochem II 2920 Micromeritics, equipped with a Thermal Conductivity Detector (TCD). The measurements were carried out in a quartz reactor by using 50 mg of sample and heating from the room temperature to 900°C with a linear ramp of 10°C/min under a constant flow of H_2 (5% in Ar, flow of 50 mL/min). In order to collect good data, the samples were previously outgassed with a flow of He (50 mL/min) at room temperature. This kind of analysis has been carried out on the air-calcined samples, with the aim of understanding the behaviour of the species and the necessity required to achieve the target materials.

The H_2-TPR profiles in *Graph 3.1* have shown two main features:

- the first peak, that is present in all $x \neq 0$ samples, is located around 500°C and is widely reported in literature to be related to the reduction of manganese (IV) to manganese (III); its intensity increases consistently, as manganese atomic percentage increases. [18] Going more into details, it can be seen that in x = 0.5 sample the peak is the result of the convolution of two contributions, that become three in x = 1 sample, resulting in the probable reduction of

	mol(H_2) theor.	mol(H_2) exp.
x = 0	-	-
x = 0.2	1.27E-5	1.09E-5
x = 0.5	3.09E-5	2.55E-5
x = 1	6.01E-5	4.62E-5

Table 3.1: theoretical and experimental hydrogen consumption of the Mn(IV) → Mn (III) reduction peak.

	mol(H_2) theor.	mol(H_2) exp.
x = 0	1.96E-4	4.73E-6
x = 0.2	2.03E-4	3.68E-5
x = 0.5	2.16E-4	4.91E-5
x = 1	2.40E-4	5.79E-5

Table 2.2: theoretical and experimental hydrogen consumption of the Mo (VI) → Mo (V/IV) + Mn(III) → Mn (II) peak

different species as the manganese presence becomes more important [22]; anyway, the deconvolution of the peaks and so the identification of the manganese (IV)-containing phases requires deeper investigation, so in first approximation is has all been considered to be inside the perovskitic structure.

- a wider peak at a temperature above 900°, thus not completely visible for instrumental limitations. More specifically, this is the result of the convolution of the contribution of the reduction of manganese (III) to manganese (II), that is reported in literature to take place at about 800°C [18], and the contribution related to the reduction of molybdenum (VI) to molybdenum (V/IV) at 900°C; this last peak, is reported in literature to be related to the reduction of octahedral molybdenum. [23]

It is also noteworthy, in the x = 0 sample, the presence of a broad low intensity peak at 700°C, whose origin is not very clear; in fact, it can both derive from the reduction of impurities containing molybdenum (VI), that are thus less stable compared to the perovskitic portion of this metal and so can be reduced at lower temperatures, or from the reduction of a small quantity of octahedral-coordinated molybdenum (VI) that has not undergone phase transition from octahedral to tetragonal at 400°C, as reported by *Ramírez et al*. [23] A final possible explanation is that this reduction peak is an artefact due to an instrumental drift that has led to an instability of the TCD baseline signal. Given for granted the uncertain origin of this peak, further analysis should be carried out; in-situ operando XRD analysis performed in the temperature range where the peak lies and in a reducing atmosphere (5% H_2 in Ar) could verify the effective composition and crystal structure of the sample but has not been carried out due to the absence of adequate instrument among the laboratory facilities.

For what concerns the hydrogen consumption, shown in *Table 3.1 and 3.2*, it can be seen that the experimental hydrogen consumption for the reduction of manganese (IV) to manganese (III) is slightly lower than the theoretical one (a part from the x = 0.2 sample, in which the difference is very

minimal and could be due to choice of the integration edges), meaning that part of this metal inside the perovskitic structure has not been reduced and is still in 4^+ oxidation state, effectively forcing part of molybdenum to have a 5^+ oxidation state. Things become more complex for the second feature, in which the experimental hydrogen consumption is more than two orders of magnitude less than the theoretical one, as reported in *Table 3.2*; the principal hypothesis, confirmed by the XRD analysis performed after the reducing treatment (see *Diffractogram 3.2*), is that mainly molybdenum impurities, i.e. $SrMoO_4$, are reduced while the perovskitic structure, and thus the reticular molybdenum (VI), is stabilized. This results in higher temperatures required to reduce molybdenum oxidation state to 5^+ or 4^+. Moreover, the reduction peak shifts at lower temperature in the case of the x = 0.5 sample, that is comparable to the behaviour of the manganese-free sample and can be indicative of the incomplete reduction of manganese (III) to manganese (II); for this hypothesis to be confirmed, again, further analysis (as an operando XANES analysis) should be carried out.

3.5 Understanding the morphology: Scanning Electron Microscopy (SEM)

Scanning Electron Microscopy (SEM) images were acquired with a Zeiss SUPRA 40VP microscope with an applied potential of 5 kV. In the following chapter, images at a magnification of 10000x will be shown, in order to have an understanding of the fresh materials' morphology.

The images in *Figure 3.2* have shown that all the samples show a very similar morphology, predominantly characterized by grains with polyhedral and faceted shapes. This phenomenon is presumably due to the presence of molybdenum: as can be seen from a comparison with the literature, several materials containing this transition metal show crystallites of comparable size and shape. [24,25] However, the high grain size, primarly due to the powder tendency to undergo sintering at the high temperatures required in calcination treatments, allows sufficiently porous structures to be obtained. More about the porosity of these materials will be depicted in *Appendix A*. A certain influence can be attributed to the utilisation of ethylene glycol as cross-linking agent for the cations in the synthesis step, but in order to have a better comprehension other synthesis methods should be carried out (for example, the Marcilly method, that involves the use of only citric acid as complexing agent [26]).

It is not to be overlooked that, in x = 0.2 and x = 0.5 samples, the images are characterized by an electrical charging of the samples, due to the electrons trapped in isolating domains, together with smaller and rounder grains, as it can be seen in *Figure 3.2 (b)* and *(c)*. However, it cannot be said

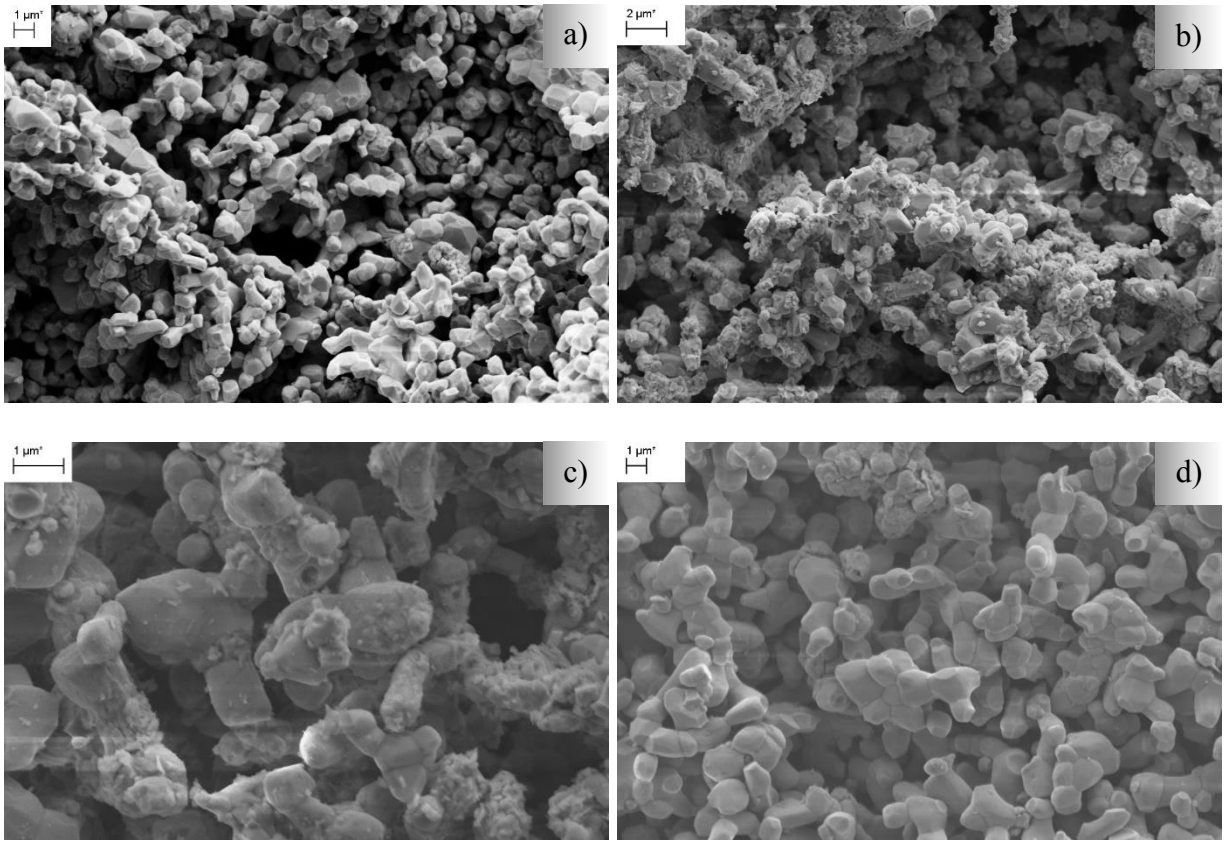

Figure 3.2: SEM images at 10000x magnification of x = 0 (a), x = 0.2 (b), x = 0.5 (c) and x = 1 (d) samples.

with certainty that these grains are indeed the oxide impurities mentioned in the previous paragraph, which would account for the insulating character of certain domains of the samples.

3.6 Understanding the composition: Energy Dispersive X-Ray (EDX) and quantitative X-Ray Photoelectron Spectroscopy (XPS)

Material	Element	Theoretical (%)	EDX (%)	XPS (%)
x = 0 **(Sr_2MgMoO_6)**	Sr	50.0	54.1	46.6
	Mg	25.0	20.7	36.4
	Mo	25.0	25.2	17.0
x = 0.2 **($Sr_2Mg_{0.8}Mn_{0.2}MoO_6$)**	Sr	50.0	48.2	41.5
	Mg	20.0	21.3	37.0
	Mn	5.0	6.9	3.4
	Mo	25.0	23.6	18.0
x = 0.5 **($Sr_2Mg_{0.5}Mn_{0.5}MoO_6$)**	Sr	50.0	40.0	55.4
	Mg	12.5	10.3	16.4
	Mn	12.5	14.6	5.4
	Mo	25.0	26.1	22.9
x = 1 **(Sr_2MnMoO_6)**	Sr	50.0	47.4	60.3
	Mn	25.0	29.3	22.1
	Mo	25.0	23.2	17.6

Table 3.3: comparison of theoretical and experimental percentage compositions of cations for the different samples.

The EDX and the XPS techniques were used to characterize the samples from the compositional point of view. The main difference between the two is their depth of analysis and this is linked to their working principles [27]:

- the EDX characterization is an analytical technique where a high energy beam of charged particles is focused into the sample being studied to stimulate the emission of characteristic X-Rays that can be collected and studied. The whole process is based on the unicity of the X-Ray spectrum of each element. This technique gives qualitative and quantitative information about elements present in a sample and its typical depth is in the order of micrometres. [28]
- the XPS analysis measure the characteristic photoelectrons emitted from a material by irradiating the sample with an X-Ray beam while simultaneously measuring the kinetic energy and number of electrons that escape from the first layers of the sample, thus making this technique useful for surface studies. Its typical depth is, in fact, considered to be between 1 and 10 nm. [29]

The two techniques are usually coupled, to achieve a good general understanding of the constituent elements of the material and their relative percentage in function of the depth, thus evaluating the presence of segregation phenomena. Moreover, by means of XPS it is possible to have an information concerning the oxidation state of the elements and their chemical environment.

The EDX analysis have been carried out using the same instrument used also for the acquisition of SEM images, the Zeiss SUPRA 40VP microscope, while XPS analysis have been performed with a Thermo Scientific ESCALAB OXi spectrometer, employing a monochromatized Al Kα source (hν = 1486.68 eV) and a charge compensation gun. The elemental quantification has been obtained by integration of the photopeaks, after Shirley-type background subtraction.

Analysing the comparison between the two techniques, it is possible to see that as the nominal manganese content was increased, strontium cation was more evident on the surface of the double perovskite cell, thus highlighting the presence of surface segregation and hypothesizing a correlation between composition and surface segregation; this is consistent with the considerations in *Paragraph 3.3.2*, where the XRD diffractograms have shown a decrease in strontium oxide intensity (and thus, content) with an increasing manganese content (X-Ray Diffraction is known to be not a surface specific analysis). The only exception was evident in the x = 0.2 sample, where the strontium percentage composition coming out from XPS quantitative analysis was the lowest. EDX percentage composition of molybdenum, instead, has shown a good agreement with the theoretical values, resulting in no segregation of the cation. A different consideration should be made for manganese; in fact, its composition from XPS analysis has shown to be lower than the nominal values in all samples, confirming, together with the compositional EDX values (in agreement with the nominal ones) the absence of surface segregation phenomena.

3.7 Understanding the surfaces: qualitative X-Ray Photoelectron Spectroscopy (XPS)

XPS technique has also been carried out in its qualitative way, in order to have a more specific understanding of the possible presence of spurious phases on the samples' surface by means of the cations' oxidation states.

The analysis has been performed again with the Thermo Scientific ESCALAB OXi spectrometer, employing a monochromatized Al Kα source (hν = 1486.68 eV). Survey spectra were acquired with

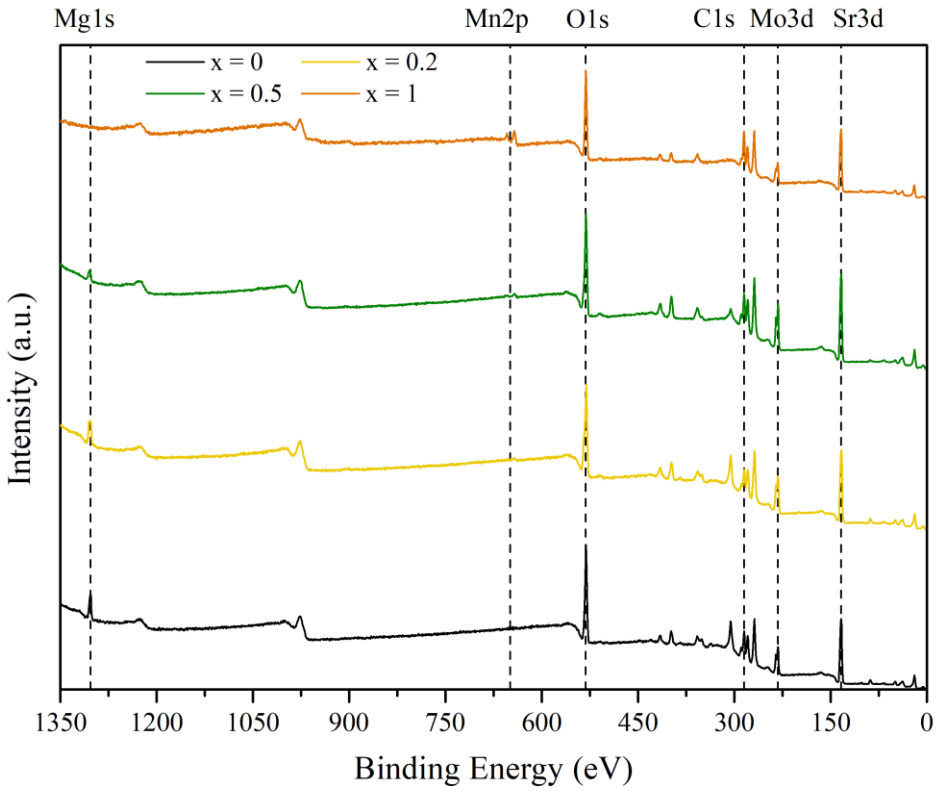

Spectrum 3.3: extended survey of SMMO materials.

a 100 eV pass energy, 0.5 eV/step and 25 ms/step dwell time, high resolution spectra have been collected at 20 eV pass energy, 0.1 eV/step and 25 ms/step dwell time.

The extended survey of SMMO materials has been reported in *Spectrum 3.3*. All expected peaks of the double perovskite are evident, with the only exception of manganese, as it can be visualised in *Spectrum 3.6*; this last element is visible only in the x = 1 sample spectra, while in other samples its shape is only suggested, probably because of its low concentration. Carbon was the only contaminant observed in the registered XPS spectra. To have a complete comprehension of the surface behaviour of the cations, a high-resolution analysis of the main features (Sr3d, Mg1s, Mn2p, Mo3d and O1s) has been carried out.

3.7.1 Strontium XPS spectra

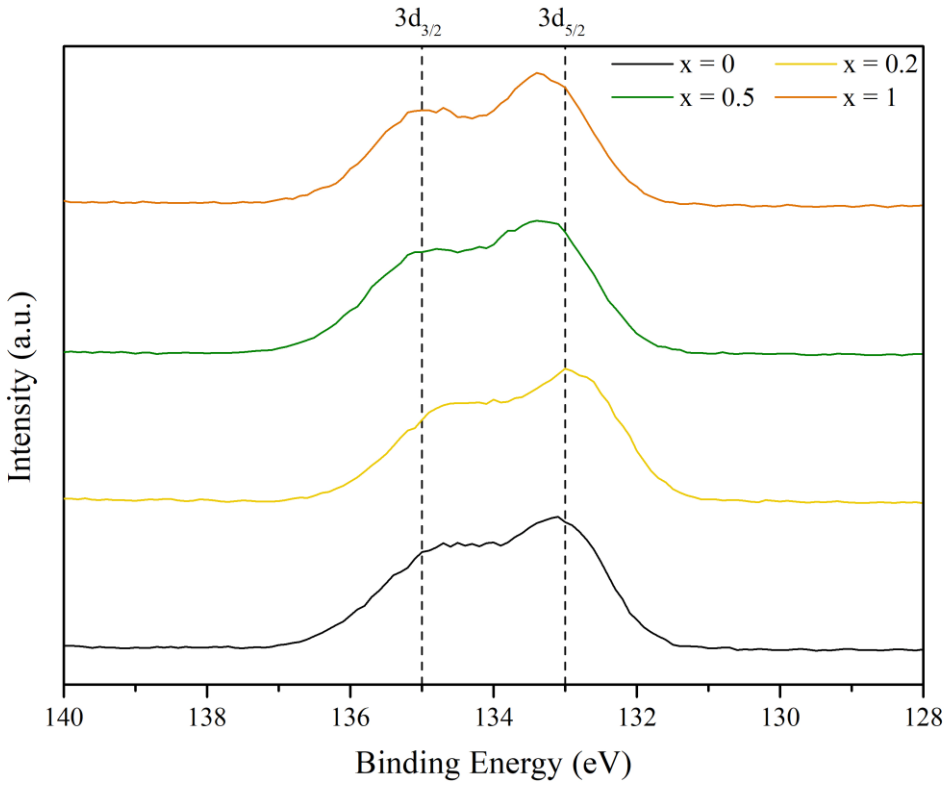

Spectrum 3.4: high resolution analysis of Sr3d peak.

The high resolution XPS analysis of Sr3d peak in *Spectrum 3.4* has shown two main features, as strontium cation is characterized by a spin-orbit splitting of its 3d peak, with a slight shift toward higher binding energy observed with increasing Mn content. The fitting procedure reveals two contributions to the Sr3d signal. A first contribution due to the presence of strontium oxide has been found at binding energies of 132.9 eV for the $3d_{5/2}$ feature and 134.6 eV for the $3d_{3/2}$ one, resulting in a spin-orbit splitting of 1.7 eV, in agreement with literature results. [30] The second feature, instead, was not uniquely attributed to a specific phase, as the position of the peak is common to both strontium carbonate and strontium molybdate phases [31,32]; again, a shift of 1.7 eV has been recorded in both $3d_{5/2}$ and $3d_{3/2}$ features. So, the comparison among the spectra suggests that molybdates/carbonates formation is enhanced in Mn-rich compounds.

3.7.2 Magnesium XPS spectra

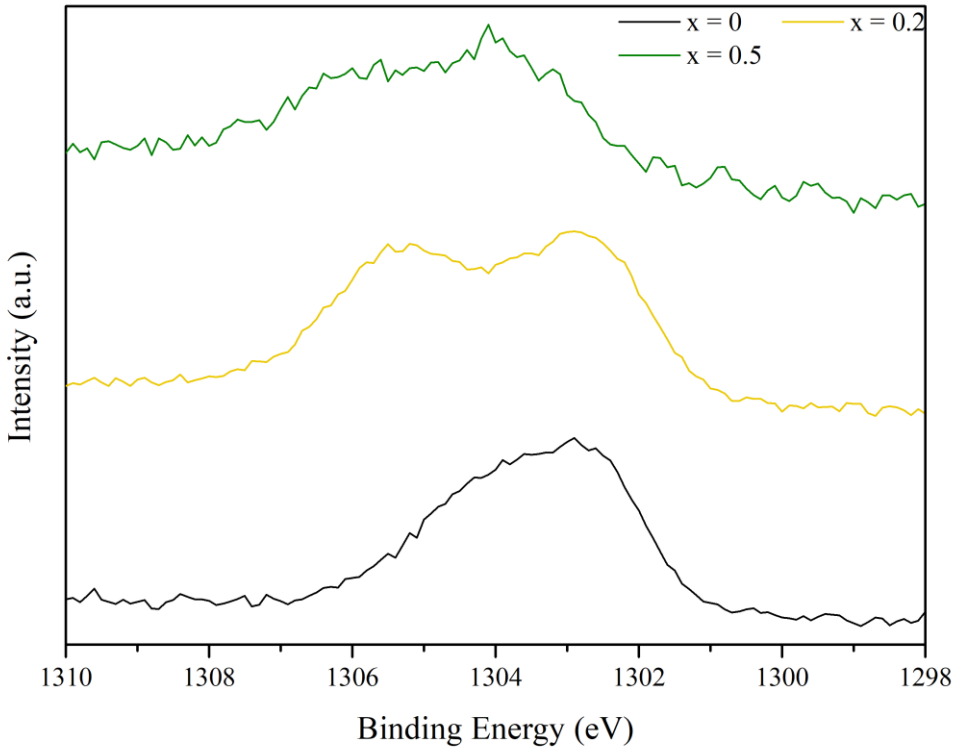

Spectrum 3.5: high resolution analysis of Mg1s peak.

The magnesium high resolution XPS spectra in *Spectrum 3.5* has shown decreasing intensity, together with the effective resolution of the features, with the decrease in magnesium content. The spectra revealed the presence of three features, corresponding to the presence of magnesium oxide, hydroxide and carbonate, respectively at binding energy of 1304.1 eV, 1302.6 eV and 1305.3 eV. These values are in good agreement with the values reported in literature works and suggest that the insertion of Mn enhances the formation of undesired surface species. [33–35]

3.7.3 Manganese XPS spectra

As discussed before, the high resolution XPS spectra reported in *Spectrum 3.6* have shown an increase in intensity because of the higher content in manganese; this is also consistent with the quantitative analysis discussed in *Paragraph 3.6*, from which it can be assumed that most of the manganese has not undergone surface segregation and consequently becomes detectable only in the sample in which its presence is prevalent over the other cations, i.e. Sr_2MnMoO_6.

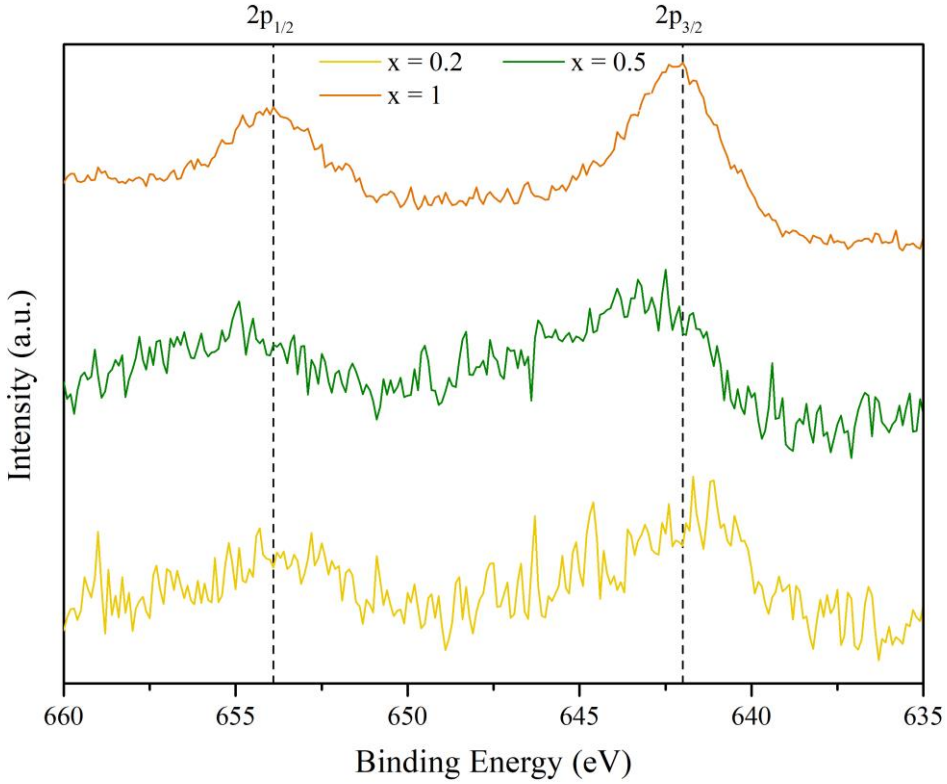

Spectrum 3.5: high resolution analysis of Mn2p peak.

In particular, the XPS spectra obtained from this compound have shown the presence of two main peaks, due to the spin-orbit splitting of the 2p orbital of manganese, related to the presence of a manganese (IV) oxide; the position of the peaks is, respectively, 642.0 eV for the $2p_{3/2}$ contribute and 653.8 eV for the $2p_{1/2}$ feature, with an optimal accordance with literature concerning both their relative position and the spin-orbit splitting (of 11.8 eV). [36,37]

However, the assignation of the peaks to Mn (II), Mn (III) or Mn (IV) is not certain, as the BEs characteristics of these manganese oxides are only a few fractions of electron volts apart one from the other. In fact, literature reports as characteristic values of manganese (III) oxide binding energies of 642.0 eV for the $2p_{3/2}$ contribute and 653.7 eV for the $Mn2p_{1/2}$ feature, while manganese (II) oxide has a binding energy of 642.5 eV for its $2p_{3/2}$ contribute. [38,39]

3.7.4 Molybdenum XPS spectra

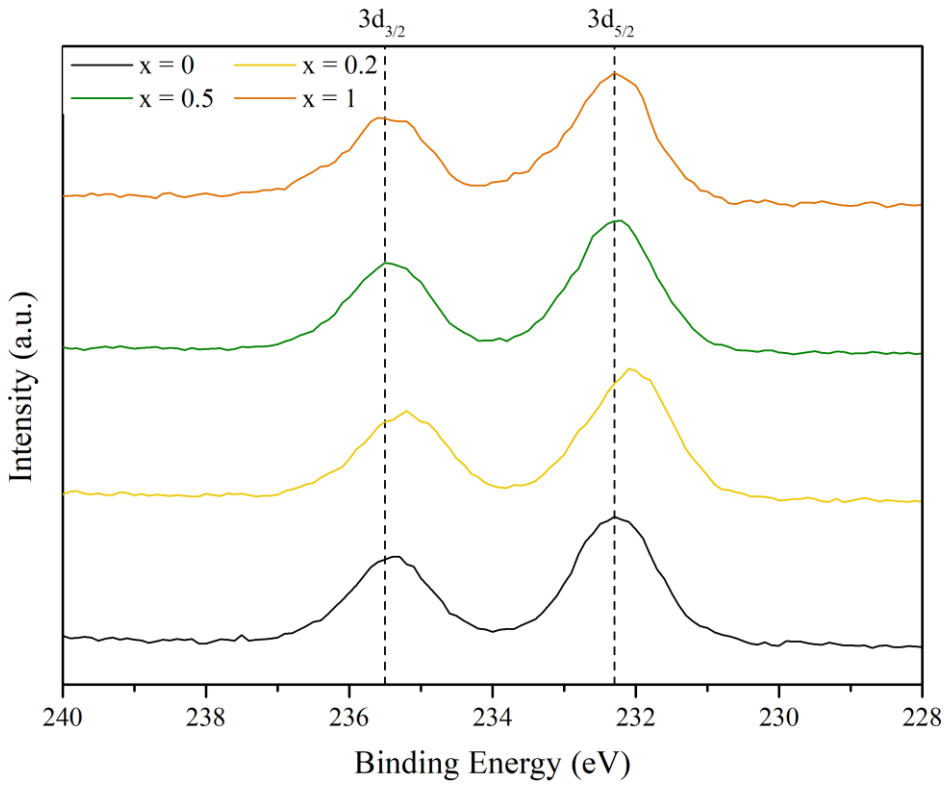

Spectrum 3.6: high resolution analysis of Mo3d peak.

The detailed XPS analysis described by *Spectrum 3.7* of molybdenum 3d and its spin-orbit splitting has confirmed, by meaning of a comparison with literature data, the presence of molybdenume (VI) oxide on the surface of all the samples, with good accordance with the relative position in binding energy of the photopeaks (respectively, 235.4 eV and 232.2 eV for $Mo3d_{5/2}$ and $Mo3d_{3/2}$ feature). The spin-orbit splitting, moreover, is calculated to be 3.2 eV, against 3.15 eV reported by other works. [40]

Overall, the influence of the different dopant on the B-site has not a significant effect on surface molybdenum, except for the x = 0.2 sample (i.e. $Sr_2Mg_{0.8}Mn_{0.2}MoO_6$); the registered photopeak for this compound has shown a shift of 0.3 eV toward lower BEs. The shift toward lower BEs is usually attributed to the presence of species in lower oxidation state (or in less oxidized environment) but it has to be considered that this shift is only slightly higher than the instrumental error (around 0.05-0.1 eV).

3.7.5 Oxygen XPS spectra

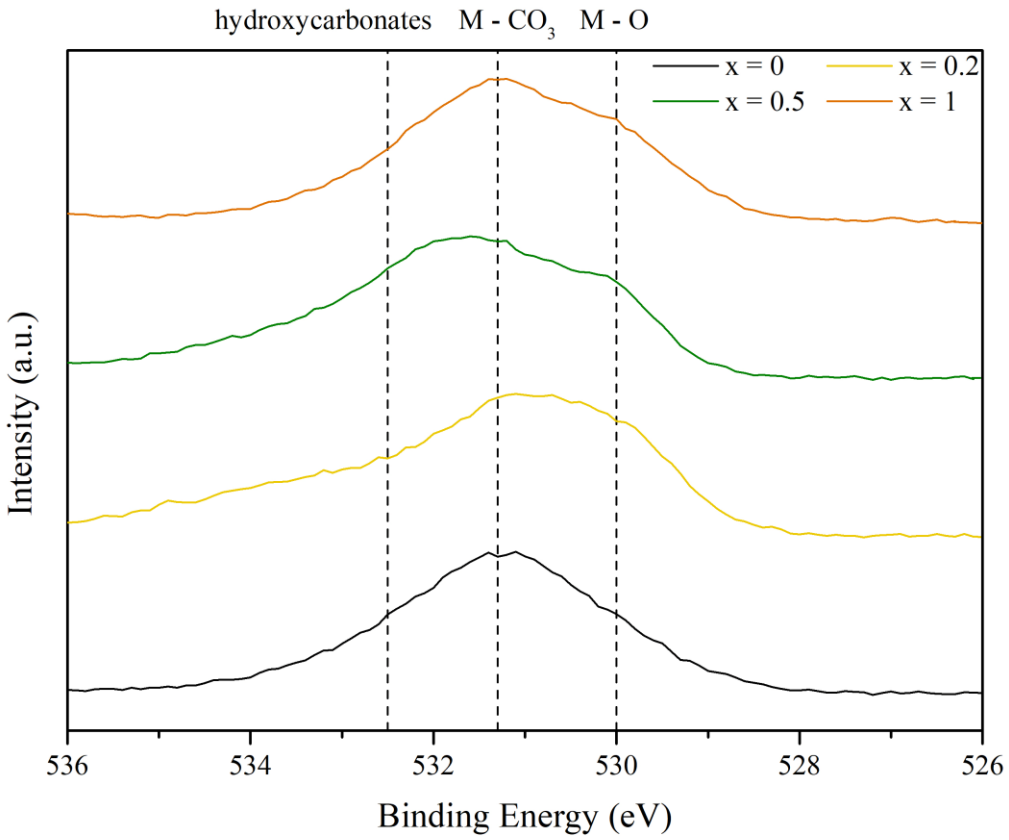

Spectrum 3.7: high resolution analysis of O1s peak.

The XPS spectra of oxygen, as it can be visualised in *Spectrum 3.8*, is characterized by three main contributions, due to metal oxides, carbonates/hydroxides and highly oxydrilate species. The binding energy values, respectively of 529.9 eV, 531.3 eV and 532.8 eV, are in agreement with what other works have reported. [41–43]

More specifically, the photopeak relative to carbonates has been found to be prevalent in all samples, thus denoting the characteristic of the different samples to be partially "passivated" on their surface by the formation of different carbonate phases, mainly strontium and magnesium, despite the reduction treatment that they have undergone. [44] The contribution due to the presence of strongly oxydrilate species, instead, is reported to be negligible in the x = 1 sample.

References

1 United States Patent Office, 3330697, 1967, 1–7.

2 T. O. L. Sunde, T. Grande and M.-A. Einarsrud, Modified Pechini Synthesis of Oxide Powders and Thin Films.

3 R. Shoja Razavi, M. Reza Loghman-Estarki, M. Farhadi-Khouzani, M. Barekat and H. Jamali, Large Scale Synthesis of Zinc Oxide Nano- and Submicro-Structures by Pechinis Method: Effect of Ethylene glycol/Citric Acid Mole Ratio on Structural and Optical Properties, *CNANO*, 2011, **7**, 807–812.

4 Y.-H. Huang, R. I. Dass, Z.-L. Xing and J. B. Goodenough, Double Perovskites as Anode Materials for Solid-Oxide Fuel Cells, *Science*, 2006, **312**, 254–257.

5 Y.-H. Huang, R. I. Dass, J. C. Denyszyn and J. B. Goodenough, Synthesis and Characterization of $Sr_2MgMoO_{6-\delta}$, *J. Electrochem. Soc.*, 2006, **153**, A1266.

6 D. A. Osinkin, E. V. Zabolotskaya, D. G. Kellerman and A. Yu. Suntsov, The physical properties and electrochemical performance of Ca-doped $Sr_2MgMoO_{6-\delta}$ as perspective anode for solid oxide fuel cells, *J Solid State Electrochem*, 2018, **22**, 1209–1215.

7 M. Kinoshitaa, K. Hara, T. Onozawa, K. Shin-mura, Y. Otani, S. Ogawa, E. Niwa, T. Hashimoto and K. Sasaki, in *Ceramic Engineering and Science Proceedings*, eds. M. Kusnezoff, N. P. Bansal, K. Shimamura, M. Fukushima and A. Gyekenyesi, John Wiley & Sons, Inc., Hoboken, NJ, USA, 2017, pp. 87–97.

8 D. Marrero-López, J. Peña-Martínez, J. C. Ruiz-Morales, M. C. Martín-Sedeño and P. Núñez, High temperature phase transition in SOFC anodes based on $Sr_2MgMoO_{6-\delta}$, *Journal of Solid State Chemistry*, 2009, **182**, 1027–1034.

9 A. K. Dorai, Y. Masuda, J.-H. Joo, S.-K. Woo and S.-D. Kim, Influence of Fe doping on the electrical properties of $Sr_2MgMoO_{6-\delta}$, *Materials Chemistry and Physics*, 2013, **139**, 360–363.

10 C. Bernuy-Lopez, M. Allix, C. A. Bridges, J. B. Claridge and M. J. Rosseinsky, $Sr_2MgMoO_{6-\delta}$: Structure, Phase Stability, and Cation Site Order Control of Reduction, *Chem. Mater.*, 2007, **19**, 1035–1043.

11 S. Vasala, H. Yamauchi and M. Karppinen, Role of $SrMoO_4$ in Sr_2MgMoO_6 synthesis, *Journal of Solid State Chemistry*, 2011, **184**, 1312–1317.

12 C. A. López, J. C. Pedregosa, D. G. Lamas and J. A. Alonso, The strongly defective double perovskite $Sr_{11}Mo_4O_{23}$: crystal structure in relation to ionic conductivity, *J Appl Crystallogr*, 2014, **47**, 1395–1401.

13 M. Calatayud, A. Markovits, M. Menetrey, B. Mguig and C. Minot, Adsorption on perfect and reduced surfaces of metal oxides, *Catalysis Today*, 2003, **85**, 125–143.

14 R. D. Shannon, Revised effective ionic radii and systematic studies of interatomic distances in halides and chalcogenides, *Acta Cryst A*, 1976, **32**, 751–767.

15 D. Sun, L. Peng, K. Cheng, Y. Zheng and S. P. Jiang, Comparative study of manganese oxides with different oxidation states for catalytic carbonylation of n-butylamine by CO_2, *Journal of CO_2 Utilization*, 2023, **68**, 102382.

16 V. G. Bhide and R. H. Dani, Electrical conductivity in oxides of manganese and related compounds, *Physica*, 1961, **27**, 821–826.

17 K. Rida, A. Benabbas, F. Bouremmad, M. A. Peña and A. Martínez-Arias, Surface properties and catalytic performance of $La_{1-x}Sr_xCrO_3$ perovskite-type oxides for CO and C_3H_6 combustion, *Catalysis Communications*, 2006, **7**, 963–968.

18 E. Brusamarello, G. Peron, F. Nigrelli and A. Glisenti, Manganese Based Perovskites in Soot Oxidation: Far from Noble Metals?, *Top Catal*, , DOI:10.1007/s11244-022-01726-y.

19 W. Jung and H. L. Tuller, Investigation of surface Sr segregation in model thin film solid oxidefuel cell perovskite electrodes, *Energy Environ. Sci.*, 2012, **5**, 5370–5378.

20 B. Koo, K. Kim, J. K. Kim, H. Kwon, J. W. Han and W. Jung, Sr Segregation in Perovskite Oxides: Why It Happens and How It Exists, *Joule*, 2018, **2**, 1476–1499.

21 M. Bugdayci, K. Taşyürek and O. Yucel, 2018, pp. 81–89.

22 C. Ramakrishna and G. Thakkallapalli, Degradation of diethyl sulfide vapors with manganese oxide catalysts supported on zeolite-13X: The influence of process parameters and mechanism in presence of ozone, *Journal of Environmental Chemical Engineering*, DOI:10.1016/j.jece.2017.02.029.

23 J. Ramírez, G. Macías, L. Cedeño-Caero, A. Gutierrez-Alejandre, R. Cuevas-García and P. Castillo, The role of titania in supported Mo, CoMo, NiMo, and NiW hydrodesulfurization catalysts: Analysis of past and new evidences, *Catalysis Today*, 2004, **98**, 19–30.

24 B. He, Z. Wang, L. Zhao, X. Pan, X. Wu and C. Xia, Ti-doped molybdenum-based perovskites as anodes for solid oxide fuel cells, *Journal of Power Sources*, 2013, **241**, 627–633.

25 Y.-F. Sun, Y.-Q. Zhang, B. Hua, Y. Behnamian, J. Li, S.-H. Cui, J.-H. Li and J.-L. Luo, Molybdenum doped $Pr_{0.5}Ba_{0.5}MnO_{3-\delta}$ (Mo-PBMO) double perovskite as a potential solid oxide fuel cell anode material, *Journal of Power Sources*, 2016, **301**, 237–241.

26 P. Courty and C. Marcilly, in *Studies in Surface Science and Catalysis*, Elsevier, 1976, vol. 1, pp. 119–145.

27 What is the difference between Xps and Edx spectroscopy techniques?, https://www.researchgate.net/post/what_is_the_difference_between_Xps_and_Edx_spectroscopy_techniques.

28 S. Ebnesajjad, in *Surface Treatment of Materials for Adhesive Bonding*, Elsevier, 2014, pp. 39–75.

29 H. Konno, in *Materials Science and Engineering of Carbon*, Elsevier, 2016, pp. 153–171.

30 C. S. Dandeneau, Y. Yang, B. W. Krueger, M. A. Olmstead, R. K. Bordia and F. S. Ohuchi, Site occupancy and cation binding states in reduced polycrystalline $Sr_xBa_{1-x}Nb_2O_6$, *Appl. Phys. Lett.*, 2014, **104**, 101607.

31 M. Wells, B. Zou, A. Mihai, R. Bower, A. Regoutz, S. Fearn, S. Maier, N. M. Alford and P. Petrov, Multiphase strontium molybdate thin films for plasmonic local heating applications, *Optical Materials Express*, , DOI:10.1364/OME.8.001806.

32 D. A. Pawlak, M. Ito, M. Oku, K. Shimamura and T. Fukuda, Interpretation of XPS O (1s) in Mixed Oxides Proved on Mixed Perovskite Crystals, *J. Phys. Chem. B*, 2002, **106**, 504–507.

33 N. C. Haider, J. Alonso and W. E. Swartz, Valence and Core Electron Spectra of Mg in MgO in Evoporated Thin Films, *Zeitschrift für Naturforschung A*, 1975, **30**, 1485–1490.

34 D. E. Haycock, M. Kasrai, C. J. Nicholls and D. S. Urch, The electronic structure of magnesium hydroxide (brucite) using X-ray emission, X-ray photoelectron, and auger spectroscopy, *J. Chem. Soc., Dalton Trans.*, 1978, 1791.

35 Magnesium | Periodic Table - IT, https://www.thermofisher.com/uk/en/home/materials-science/learning-center/periodic-table/alkaline-earth-metal/magnesium.html.

36 B. N. Ivanov-Ehmin, N. A. Nevskaya, B. E. Zajtsev and T. M. Ivanova, Synthesis and properties of calcium and strontium hydroxomanganates (3), *Zh. Neorg. Khim.; (USSR)*.

37 G. C. Allen, S. J. Harris and L. Jutson, A study of a number of mixed transition metal oxide spinels using X-Ray Photoelectron Spectroscopy.

38 H. F. Franzen, M. X. Umaña, J. R. McCreary and R. J. Thorn, XPS spectra of some transition metal and alkaline earth monochalcogenides, *Journal of Solid State Chemistry*, 1976, **18**, 363–368.

39 B. J. Tan, K. J. Klabunde and P. M. A. Sherwood, XPS studies of solvated metal atom dispersed (SMAD) catalysts. Evidence for layered cobalt-manganese particles on alumina and silica, *J. Am. Chem. Soc.*, 1991, **113**, 855–861.

40 B. M. Garland, N. Fairley, N. C. Strandwitz, R. Thorpe, P. Bargiela and J. Baltrusaitis, A study of in situ reduction of MoO_3 to MoO_2 by X-ray Photoelectron Spectroscopy, *Applied Surface Science*, 2022, **598**, 153827.

41 Interpretation of XPS O (1s) in Mixed Oxides Proved on Mixed Perovskite Crystals, https://pubs.acs.org/doi/epdf/10.1021/jp012040a.

42 M. Rjeb, A. Labzour, A. Rjeb, S. Sayouri, M. Chafik, E. A., S. Massey and A. Adnot, Contribution to the study by X-ray photoelectron spectrocsopy of the natural aging of the polypropylene, *Morrocan Journal of Condensed Matter*, 2004, **5**, 168–172.

43 M. Mullet, V. Khare and C. Ruby, XPS study of Fe(II)/Fe(III) (oxy)hydroxycarbonate green rust compounds, *Surface and Interface Analysis*, 2008, **40**, 323–328.

44 Oxygen | XPS Periodic Table - IT, https://www.thermofisher.com/uk/en/home/materials-science/learning-center/periodic-table/non-metal/oxygen.html.

4. Thermo-valorisation of the gas mixture: CO_2 reduction to CO

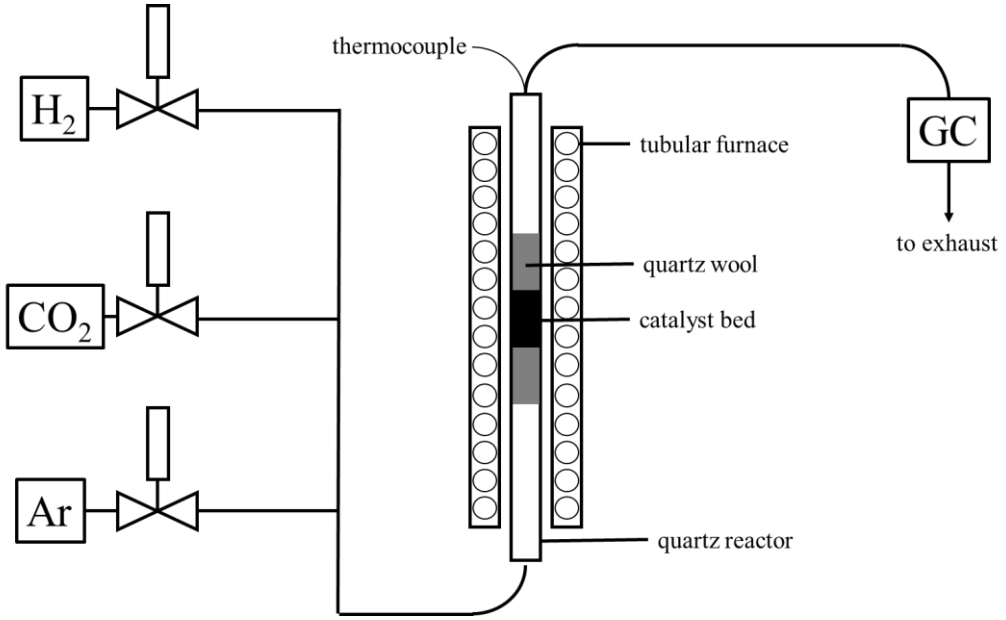

Figure 4.1: schematic representation of the set-up utilised for the thermo-catalytic reduction of CO_2 to CO.

Chapter 4 will be dedicated to the explanation of the use of SMMO materials as catalysts for the Reverse Water-Gas Shift reaction (RWGS), both from the architectural point of view, thus with a brief description of the experimental apparatus, and from the pure chemical point of view, regarding firstly the results but also the analysis of post-reaction samples and the relative considerations in respect to the fresh ones. The depicted reaction is summarised as:

$$CO_2 + H_2 \xrightarrow{\Delta} CO + H_2O \qquad (4.1)$$

The catalytic set-up utilised for the aim of this work, represented in *Figure 4.1*, was composed by a fixed reaction bed, in which the reduced powders were deposited in a 6 mm quartz tube between two layers of quartz wool. The reactor, finally, was inserted into a tubular furnace, which temperature was controlled by a K-type thermocouple on the upper end of the tube, in which the connection to the Gas Chromatographer was located. The inlet gas fluxes were managed by three mass-flow controllers (MFCs), in order to have a H_2/CO_2 ratio of 4:1 (and be coherent with the 80% H_2 - 20% CO_2 gas mixture), while argon was used as carrier gas.

The exhaust gasses analysis was carried out by an Agilent Technologies 7890A GC System, equipped with a Porapak Q and a Molsieve column, while the gas detection was controlled by a TCD detector. The sampling time was equal to 12 minutes, to have a complete evaluation of all the output gasses.

4.1 Catalytic results

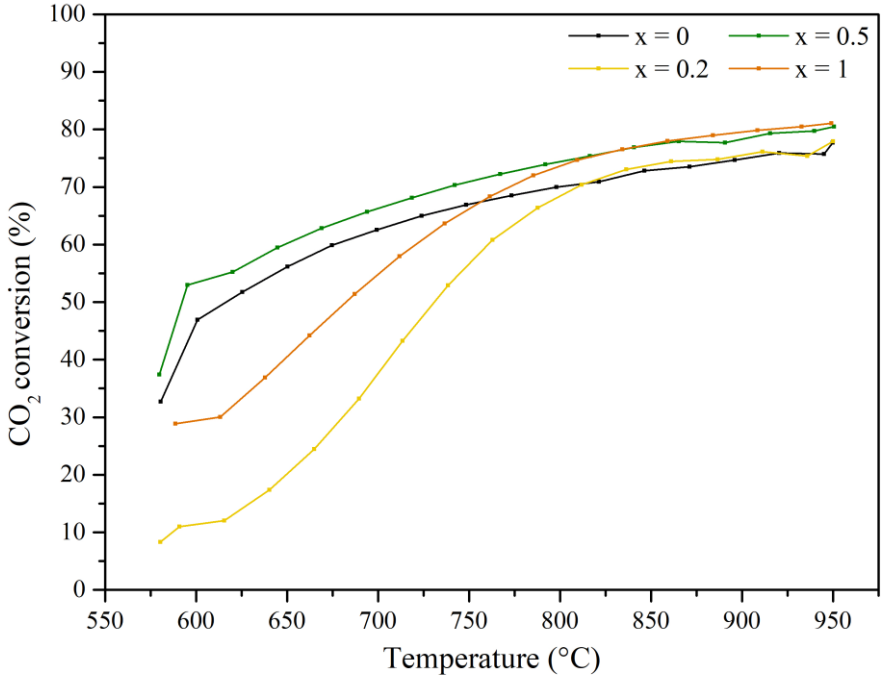

Graph 4.1: CO_2 conversion percentage with respect to reaction temperature.

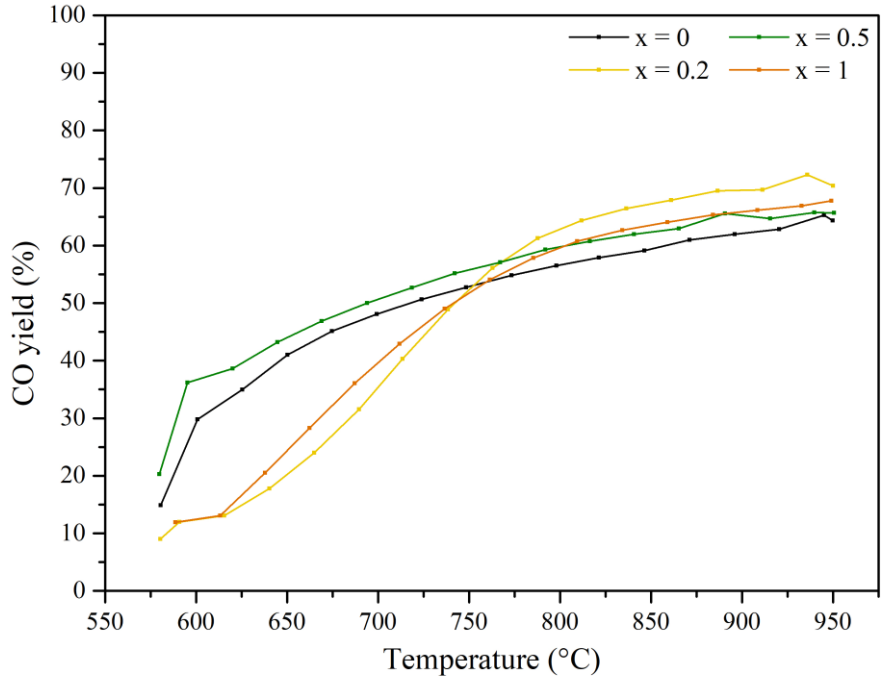

Graph 4.2: CO yield percentage with respect to reaction temperature.

Graphs 4.1 and *4.2* have shown a temperature on-set of the RWGS reaction, that for all the SMMO materials is about 580°C, independently of the doping degree in B-site: this value is quite accurate, since the temperature has been measured at the time that the produced gas were injected into the GC system; however, to maximize the precision on this temperature value, shorter connection between the furnace and the GC system should be arranged, making sure that the instrument is not in need of "calibration" by increasing the injection speed.

It can easily be noted that the catalytic activity of the samples towards CO_2 reduction to CO follows a "twins"-like behaviour, in which x = 0 and x = 0.5 samples are coupled, and so x = 0.2 and x = 1 samples. The principal hypothesis in support, following the consideration discussed in *Paragraph 3.4* about the H_2-TPR profile, is that in x = 0.5 the predominant contribution from manganese cation comes from its 3^+ oxidation state and it is in balance with the property of Lewis base of magnesium (II) cation. [1,2] In fact, as seen in *Graph 3.1*, x = 0 and x = 0.5 samples has shown a similar behaviour regarding the second reduction peaks, hypothetically due only to the molybdenum cation reduction, allowing to postulate the partial absence of manganese (II) in the x = 0.5 sample.

In support, it is known in literature by previous works that have investigated the role of manganese in perovskite-based catalyst, that this cation in its 3^+ oxidation state is the active and responsible redox site for oxygen exchange [3,4]. This property conferred to the material is fundamental because the adsorption of the CO_2 can thus happen both in the Lewis basic magnesium (II) cations and via exchange between the reticular perovskite oxygen and the carbonylic oxygen of CO_2 and justifies the higher activity of the x = 0.5 sample towards CO_2 reduction. This synergistic effect was lost in x = 0.2 sample, in which the H_2-TPR profile has suggested the complete reduction of manganese (III) to (II), and x = 1 sample, that is magnesium-free and thus not containing a basic cation in which the CO_2 can be coordinated. In both these materials, the active redox site is only molybdenum, for whose activity toward the RWGS reaction literature has not suggested a clear mechanism.

A deeper analysis of the adsorption mechanism of CO_2 by magnesium (II) cation has been carried out by *Song et al.* [5], who have identified and explained the two characteristic steps of the CO_2 chemisorption process. The first step - and the fastest one - was attributed to the diffusion from the bulk gas phase to the superficial MgO while the second - and slowest – has been correlated to the high intra-particle diffusion resistance, due to the small dimension of the pores. Thus, a good magnesium-containing catalyst should have both high surface area and a good pore size distribution.

From the overall evaluation to the trend of CO_2 conversion and CO yield, it can be seen that the difference in performance is no longer evident at high temperatures, since after 750°C the curves showned a plateau in which all materials were contained within a range of about 4% (from 77.7% of Sr_2MgMoO_6 to 81.1% of Sr_2MnMoO_6). It is noteworthy that the CO yield followed the same trend as the CO_2 conversion, but with lower values: for example, for the x = 0 sample, CO_2 conversion value was 46.9% and, instead, CO yield value was 29.8% but this behaviour is common in all samples; the hypothesis, still not confirmed by experimental evidences, is that the SMMO materials were not selective only for the CO_2 reduction to CO and presented a not negligible catalytic activity towards the formation of a short chain hydrocarbon, most likely CH_3OH, that was condensed in the chiller (together with water) placed right before the entrance into the GC system.

The accomplished results are quite promising if compared to the state-of-the-art materials. In fact, the catalysts used as promoters for the RWGS reaction are usually ceria or alumina-supported noble metals (in particular platinum, gold and ruthenium [6–9]) nanoparticles, with conversion degree of about 50% at 450°C. This value is comparable to the one achieved by the x = 0.5 sample but at 600°C, thus requiring a higher operating temperature; however, the main benefit of changing the active material is the non-utilisation of PMGs materials, that are for instance very expensive, of uncertain supply and not environmentally sustainable.

4.2 Post-reaction Characterization of SMMO materials

All the sample were again characterized, after their use as catalysts for the RWGS reaction, in order to have a better comprehension of eventual structural and/or surface modification and also to give some considerations about the possibility for these materials to be re-used in CO_2 reduction reaction cycles.

4.2.1 X-Ray Diffraction (XRD)

The XRD analysis were performed keeping unchanged the experimental parameters used for the fresh samples and described in *Paragraph 3.3*.

The resulting patterns, reported in all the *Diffractograms 4.1-4.4*, have shown no significant differences between the fresh samples and the same materials after a RWGS reaction cycle; among the

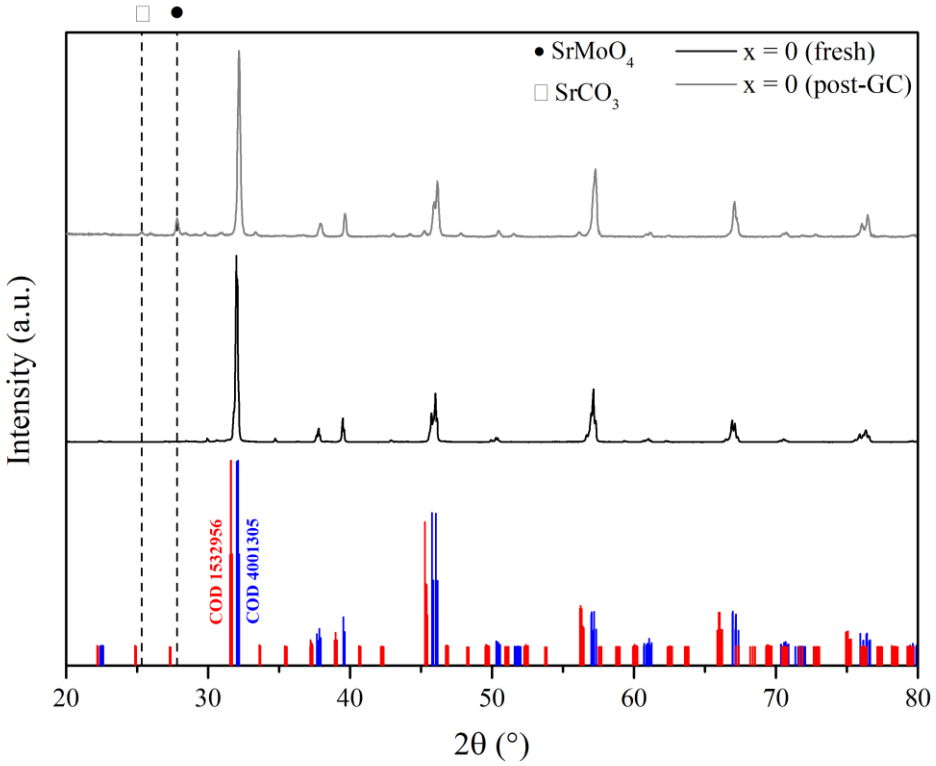

Diffractogram 4.1: XRD pattern of the fresh and post-reaction x = 0 sample.

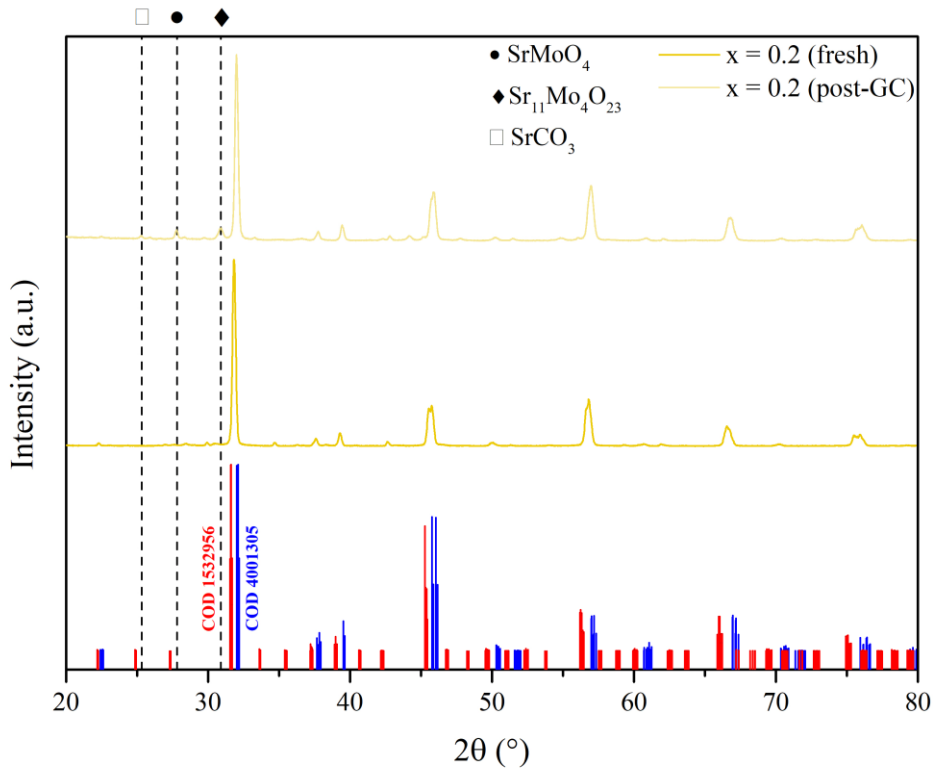

Diffractogram 4.2: XRD pattern of the fresh and post-reaction x = 0.2 sample.

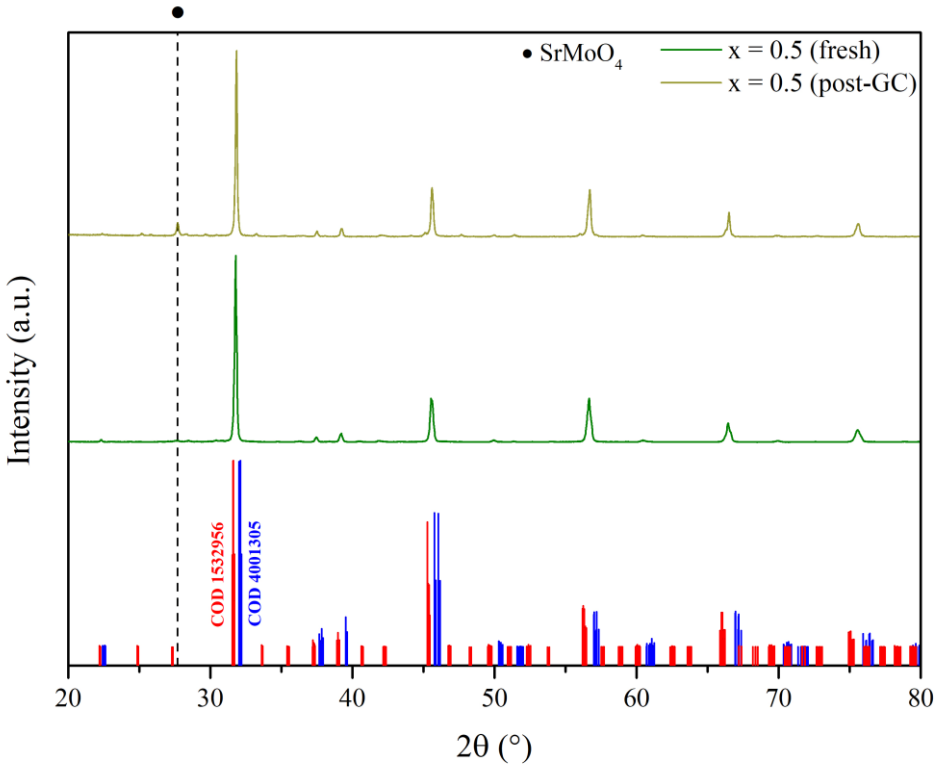

Diffractogram 4.3: XRD pattern of the fresh and post-reaction x = 0.5 sample.

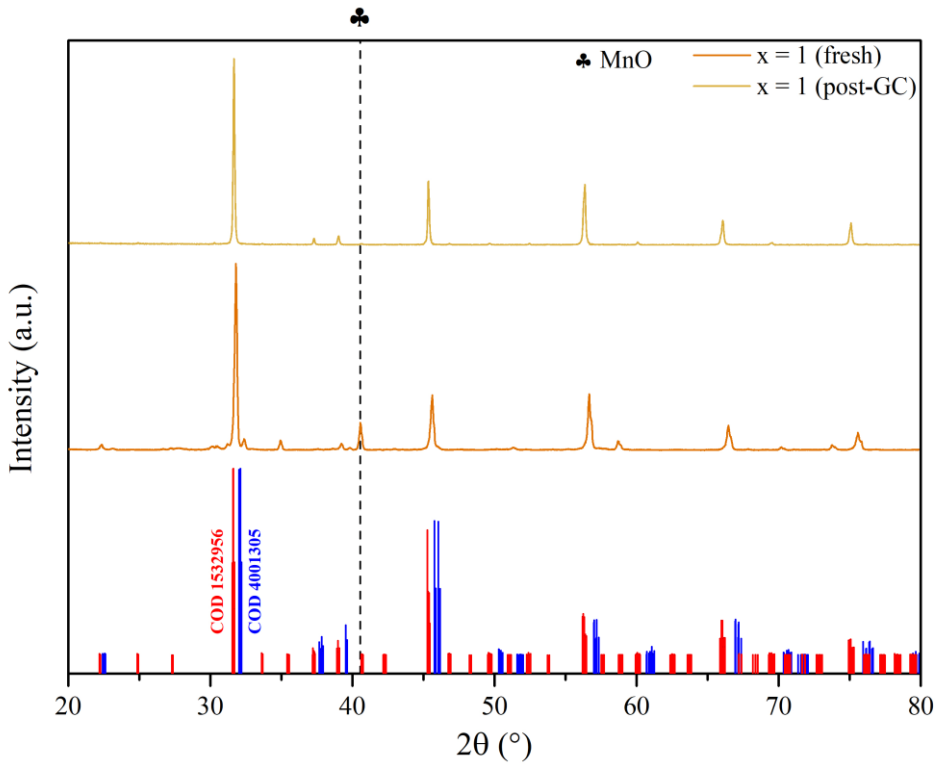

Diffractogram 4.4: XRD pattern of the fresh and post-reaction x = 1 sample.

noticeable features, it is relevant underlining the re-formation (in small amount) of spurious phases due to the oxidant atmosphere, the most peculiar being $SrMoO_4$. [10,11] Strontium carbonate presence in the bulk phase was instead observed only in strontium-rich samples (*Diffractogram 4.1* and *4.2*), i.e. Sr_2MgMoO_6 and $Sr_2Mg_{0.8}Mn_{0.2}MoO_6$ materials, thus hypothesizing an influence of magnesium cation on the surface segregation of strontium in its carbonate phase. The x = 0.2 sample, after being exposed to the reaction atmosphere, has also shown the re-formation of $Sr_{11}Mo_4O_{23}$, the strongly defective double perovskite structure depicted in *Paragraph 3.3.1*.

A peculiar thing was the reduction of manganese (II) oxide after exposure to the reaction atmosphere of the x = 1 sample, as evidenced by *Diffractogram 4.4*; this is consistent with the high hydrogen presence in the reaction atmosphere, that above 340°C should reduce this kind of impurity. [12] No other impurities in appreciable quantities have been shown by the XRD analysis of this sample.

Resuming the previous considerations, the XRD analyses have shown that SMMO materials are good candidates for replacing PMGs materials as catalysts for the RWGS reaction, as they show comparable activity, even if at higher temperatures. The negligible coking (confirmed by XPS analysis in the following paragraphs), evinced by the appearance of small intensity reflexes, and the presence of impurities in small quantities is also indicative of a possible use over a longer reaction period, but further and longer duration measurements should be carried out in order to have a better comprehension of the long-term catalytic behaviour. Other works in literature have studied the activity toward RWGS reaction by means of Ni-doped lanthanum cobaltate (Ni-$LaCoO_3$), underlining the influence of Ni-doping on the B site both on the on-set temperature and the activity of the catalyst; in fact, both the phenomena were optimal with a 10% load in nickel, while the on-set temperature increased to the Ni-free $LaCoO_3$ one (and CO selectivity decreased) with higher nickel load. [13]

4.2.2 Understanding the post-reaction morphology: Scanning Electron Microscopy (SEM)

The SEM images acquired after the RWGS reaction cycle have shown no significant modification to the morphology and porosity of the samples; the polyhedric-like structure was maintained in all the SMMO family, together with the closed porosity (see considerations in *Paragraph 3.5*).

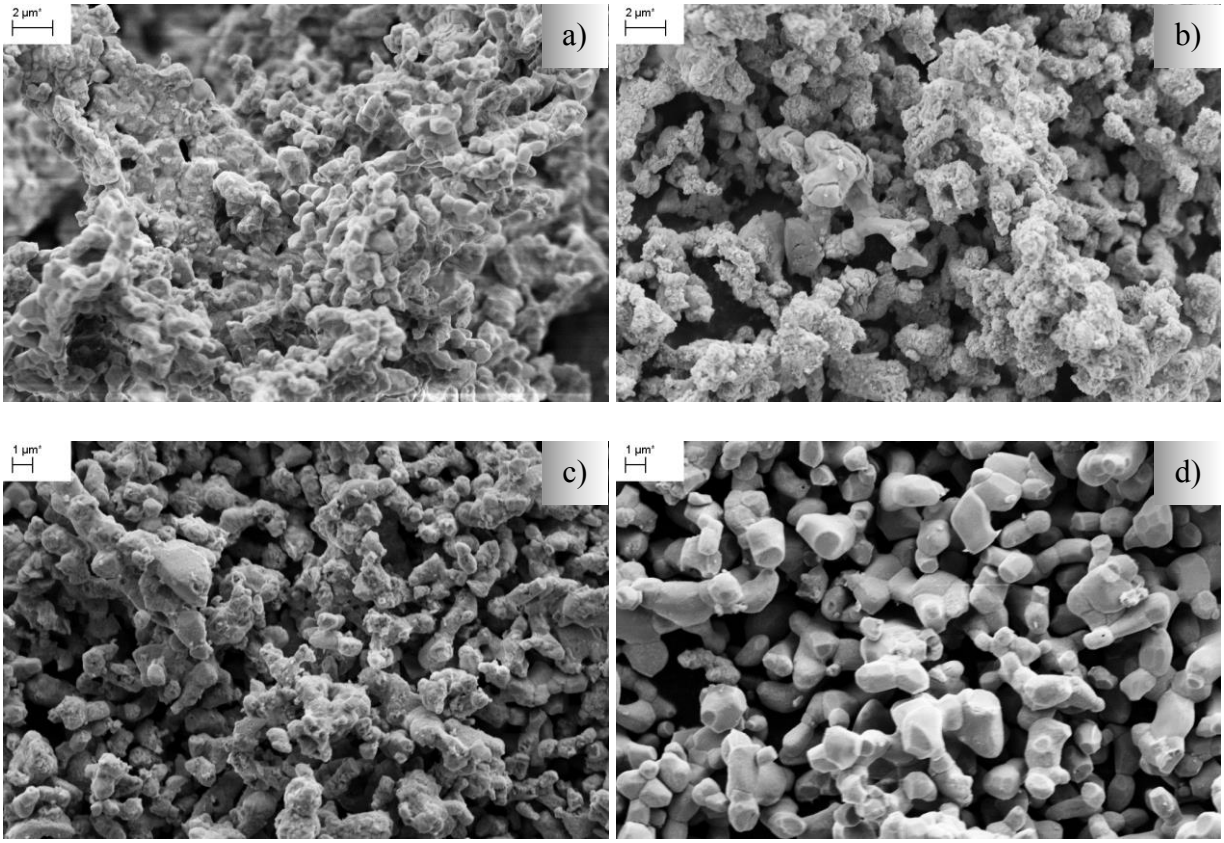

Figure 4.2: SEM images at 10000x magnification of x = 0 (a), x = 0.2 (b), x = 0.5 (c) and x = 1 (d) samples after their utilisation as catalyst for RWGS reaction.

It should be noted that the image of x = 0.2 sample has also shown the increased presence of rounded-like particles; if the hypothesis of correlation between these particles and the presence of impurities was correct, their presence would be coherent with the XRD pattern of the sample (see *Diffractogram 4.2*), that has shown the formation of multiple spurious phases after the reaction cycle, of which the predominant is strontium carbonate (consistently with the tendency of this cation, if exposed to an oxidizing atmosphere, to form carbonate and oxide impurities [14,15]).

4.2.3 Understanding the post-reaction composition: Energy Dispersive X-Ray (EDX) and quantitative X-Ray Photoelectron Spectroscopy (XPS)

The composition of all samples has again been studied after the RWGS reaction cycle, in order to better understand eventual segregation phenomena by means of a comparison between the fresh materials and the post-reaction ones. The more evident phenomenon observed after reaction was the surface segregation of strontium cation, in the samples with lower manganese content (x = 0, 0.2) which is substituted by the molybdenum

Material	Element	Theoretical (%)	EDX fresh (%)	EDX post-GC (%)
x = 0 (Sr_2MgMoO_6)	Sr	50.0	54.1	54.4
	Mg	25.0	20.7	20.4
	Mo	25.0	25.2	25.2
x = 0.2 ($Sr_2Mg_{0.8}Mn_{0.2}MoO_6$)	Sr	50.0	48.2	49.3
	Mg	20.0	21.3	19.1
	Mn	5.0	6.9	6.8
	Mo	25.0	23.6	24.9
x = 0.5 ($Sr_2Mg_{0.5}Mn_{0.5}MoO_6$)	Sr	50.0	40.0	49.4
	Mg	12.5	10.3	12.0
	Mn	12.5	14.6	12.2
	Mo	25.0	26.1	26.4
x = 1 (Sr_2MnMoO_6)	Sr	50.0	47.4	49.1
	Mn	25.0	29.3	27.1
	Mo	25.0	23.2	23.8

Table 4.1: comparison of EDX percentage composition of cations for different samples before and after the RWGS reaction.

surface segregation when the amount of manganese increases (x = 0.5, 1). It has to be considered, however, that molybdenum has shown a slight increase after reaction in spite of the significant strontium segregation. The behaviour of strontium is consistent with what is expected consequently to the partial re-oxidation of the samples, also shown in *Diffractogram 4.1 - 4.4*. Molybdenum surface segregation has suggested a possible role in RWGS reaction. The behaviour of this cation was only revealed by XPS thus indicating that this phenomenon only interests few outermost monolayers. Notably, the strontium amount revealed by the EDX was higher in the sample x = 0.5 in which molybdenum segregation has begun to prevail. Further considerations on the eventual presence of superficial impurities will be reported in *Paragraph 4.2.4*, by means of comparison of before and after reaction qualitative XPS analysis.

Material	Element	Theoretical (%)	XPS fresh (%)	XPS post-GC (%)
x = 0 (Sr_2MgMoO_6)	Sr	50.0	46.6	51.7
	Mg	25.0	36.4	33.2
	Mo	25.0	17.0	15.1
x = 0.2 ($Sr_2Mg_{0.8}Mn_{0.2}MoO_6$)	Sr	50.0	41.5	54.6
	Mg	20.0	37.0	17.6
	Mn	5.0	3.4	7.1
	Mo	25.0	18.0	20.7
x = 0.5 ($Sr_2Mg_{0.5}Mn_{0.5}MoO_6$)	Sr	50.0	55.4	56.6
	Mg	12.5	16.4	14.8
	Mn	12.5	5.4	0.6
	Mo	25.0	22.9	28
x = 1 (Sr_2MnMoO_6)	Sr	50.0	60.3	63.0
	Mn	25.0	22.1	7.4
	Mo	25.0	17.6	29.5

Table 4.2: comparison of XPS percentage composition of cations for different samples before and after the RWGS reaction.

Material	Element	XPS fresh (%)	XPS post-GC (%)
x = 0 (Sr_2MgMoO_6)	C ($M - CO_3$)	7.7	4.8
	O ($M - CO_3$)	33.5	12.9
x = 0.2 ($Sr_2Mg_{0.8}Mn_{0.2}MoO_6$)	C ($M - CO_3$)	6.6	5.2
	O ($M - CO_3$)	25.2	8.9
x = 0.5 ($Sr_2Mg_{0.5}Mn_{0.5}MoO_6$)	C ($M - CO_3$)	7.2	5.5
	O ($M - CO_3$)	25.1	11.7
x = 1 (Sr_2MnMoO_6)	C ($M - CO_3$)	6.6	7.1
	O ($M - CO_3$)	20.9	24.6

Table 4.3: comparison of XPS percentage composition of carbon and oxygen derived from the fitting of the carbonate contribution.

No substantial variations in composition were reported for magnesium cation by the EDX analysis; on the contrary, the XPS analysis have shown a percentage decrease, thus resulting in a less prevalent surface segregation phenomena. This could be counterintuitive, if considered the tendency of magnesium cation to undergo superficial segregation because of a mismatch between dopant and matrix,

but is probably a consequence of more relevant presence of Sr (XPS can only furnish relative compositions). [16]

Manganese cation was not essentially subject to changes in bulk composition after its catalytic utilisation, as visualised in *Table 4.1*. The same thing cannot be said about the XPS analysis results, that have shown different behaviours in different samples. x = 0.2 sample, in fact, is characterized by an evident segregation phenomenon, as manganese percentage is reported to be double the nominal value; differently, in x = 0.5 sample, manganese was almost not detected by the instrumental apparatus, denoting the almost complete absence of segregation. Sr_2MnMoO_6 material, eventually, was characterized by a decrease of one third of manganese content, thus underlining the manganese tendency to be present prevalently in the crystalline cell. This characteristic is in agreement with the surface segregation of molybdenum with which can be related.

Lastly, molybdenum EDX were not influenced by the reaction environment and changed by values around the percentage unit; on the contrary, an increasing tendency to undergo segregation with the increase in manganese content was shown in *Table 4.2*. This phenomenon could be due to the higher ionic radius of sixfold-coordinated manganese (II) cation, that Shannon has reported to be bigger than sixfold-coordinated molybdenum (VI) cation; its higher atomic percentage may have generated a compressive stress in the cell structure, forcing the smaller cation to migrate to the surface. [17]

Table 4.3 reportes the percentage quantities obtained from the quantification of the carbonate contribution both for C1s photopeak and O1s one, in comparison to the fresh samples. A decrease in carbonate species content was observed, as the relative contributions have dramatically decreased; this is consistent with a thermal removal of the spurious species, due to the high operating temperatures. The only exception is reported to be the x = 1 sample, in which the carbonate phase content has increased, mainly because of strontium surface segregation. It is also noteworthy underlining again the increase in carbonate contribution as more manganese is present, consistently with the considerations above.

4.2.4 Understanding the post-reaction surfaces: X-Ray Photoelectron Spectroscopy (XPS)

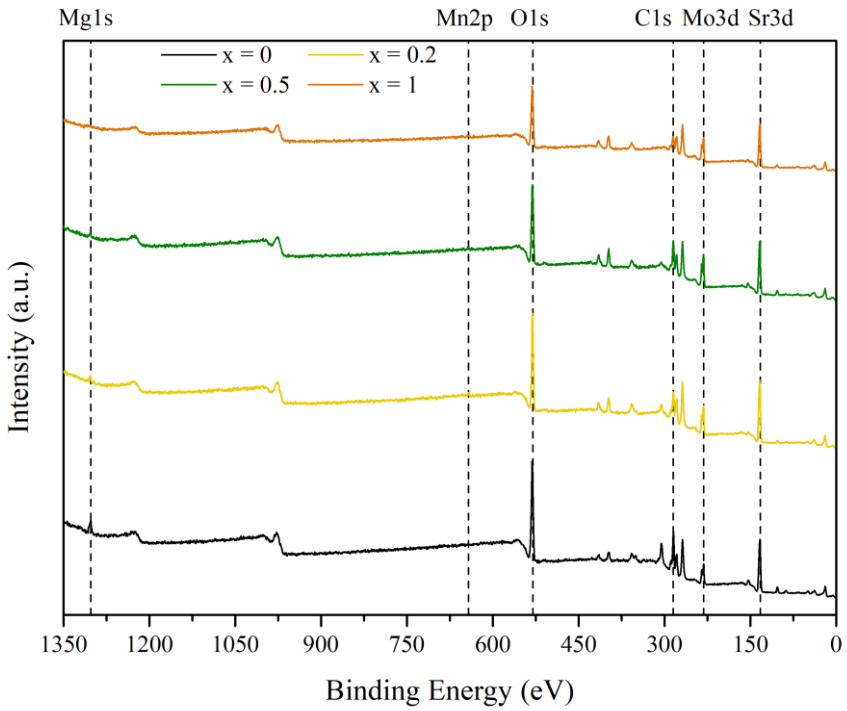

Spectrum 4.1: extended survey of SMMO materials after reaction.

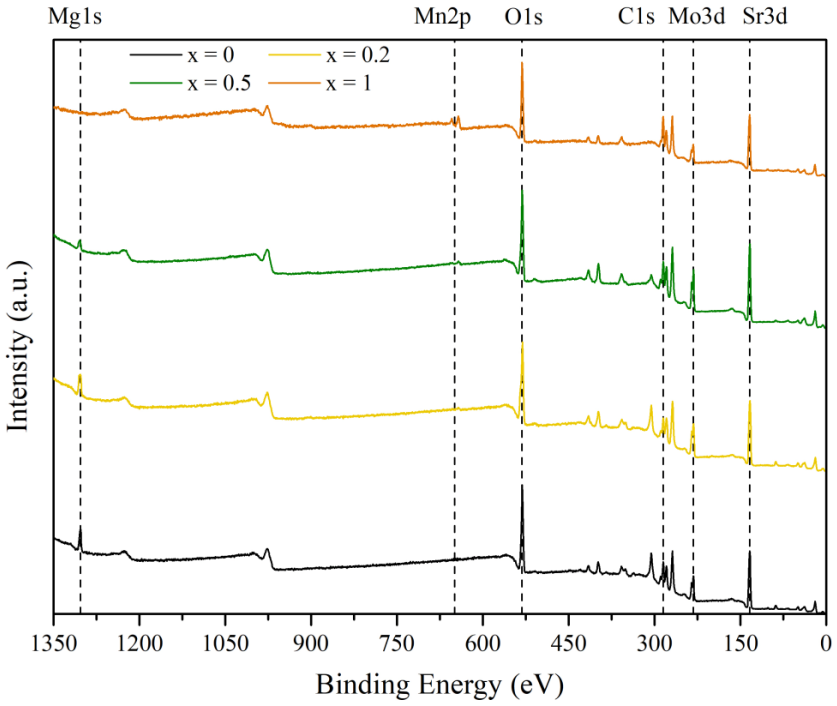

Spectrum 4.2: extended survey of SMMO materials before reaction.

Further XPS investigations on the post-reaction samples have been carried out, to have a better understanding of possible de-activation by means of surface carbon deposition or, in general, surface modification of the samples.

The extended survey of post-reaction SMMO materials has been reported in *Spectrum 4.1*, in comparison with the fresh ones in *Spectrum 4.2*. Again, all the expected peaks are evident. Silicon is now reported to be an ulterior contaminant, whose presence is due to the quartz wool utilised for the catalytic bed preparation, while carbon was already observed. To have a complete comprehension of the surface modification of the cations, a high-resolution analysis of the main spectral regions (Sr3d, Mg1s, Mn2p, Mo3d and O1s) has been carried out.

4.2.4.1 Strontium XPS spectra

The detailed analysis of the Sr3d photopeak has shown a variation in shape between fresh and post-reaction samples, due to the increase on the superficial molybdate/carbonate phase after the exposure in a carbon-rich environment. The result is a peak in which the $3d_{5/2}$ and $3d_{3/2}$ contribution are less distinguishable, apart from the x = 1 sample, in which strontium carbonate (or molybdate) is reported to be present in a lower quantity, comparable to the fresh sample.

The relative position of the photopeaks has not changed, as it is reported to be 132.9 eV ($3d_{5/2}$) and 134.6 eV ($3d_{3/2}$) for the molybdate/carbonate phase, while the oxide phase is located at 133.9 eV ($3d_{5/2}$) and 135.6 eV ($3d_{3/2}$), with a maintaining in the spin-orbit splitting value of 1.7 eV that was also confirmed by literature. [18–20]

Taking into consideration also the quantitative results, reported in *Table 4.1*, it can be hypothesized that strontium is segregated on the surface mainly as carbonate in the samples x = 0 and x = 0.2 whereas in the samples x = 0.5 and x = 1, in which the mainly moving specie is molybdenum, the attitude of molybdenum toward the formation of Mo (VI)-oxides could be reflected.

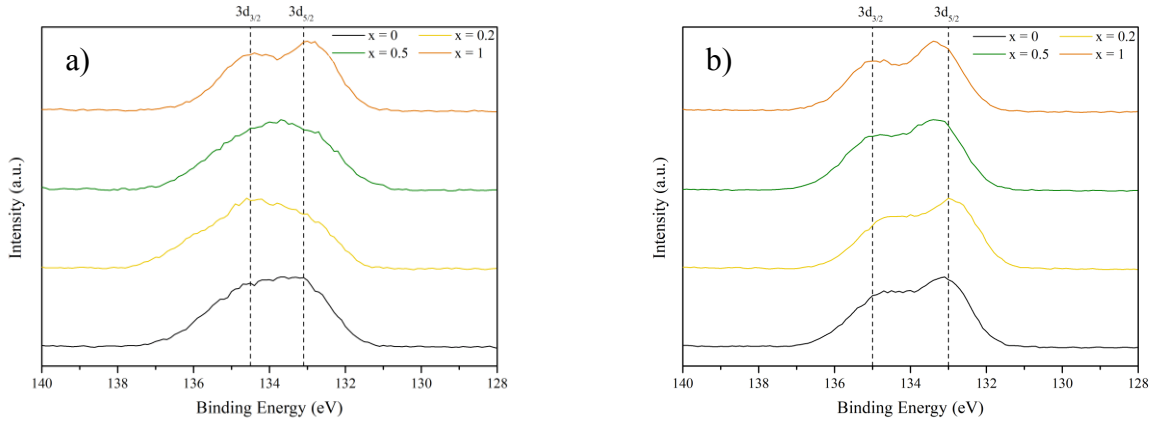

Spectrum 4.3: high resolution analysis of Sr3d peak after (a) and before (b) reaction.

4.2.4.2 Magnesium XPS spectra

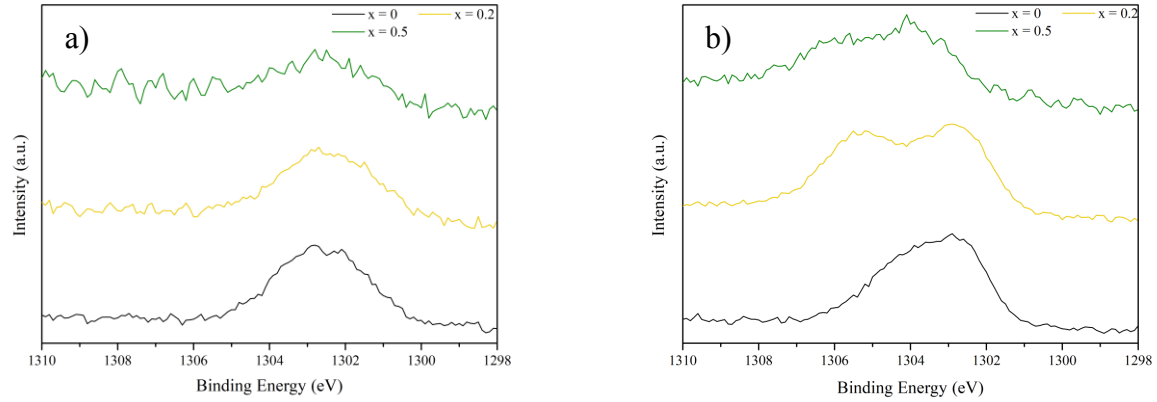

Spectrum 4.4: high resolution analysis of Mg1s peak after (a) and before (b) reaction.

The XPS detailed spectra of Mg1s after reaction has shown a decrease in the carbonate and hydroxide contributions, located respectively at binding energies of 1304.1 eV and 1305.3 eV; this is consistent with the reaction operating temperature, that were sufficient to lower the magnesium carbonate/hydroxide species content. The relative position of the photopeaks, moreover, were not subjected to binding energy shifts following the reaction cycle.

4.2.4.3 Manganese XPS spectra

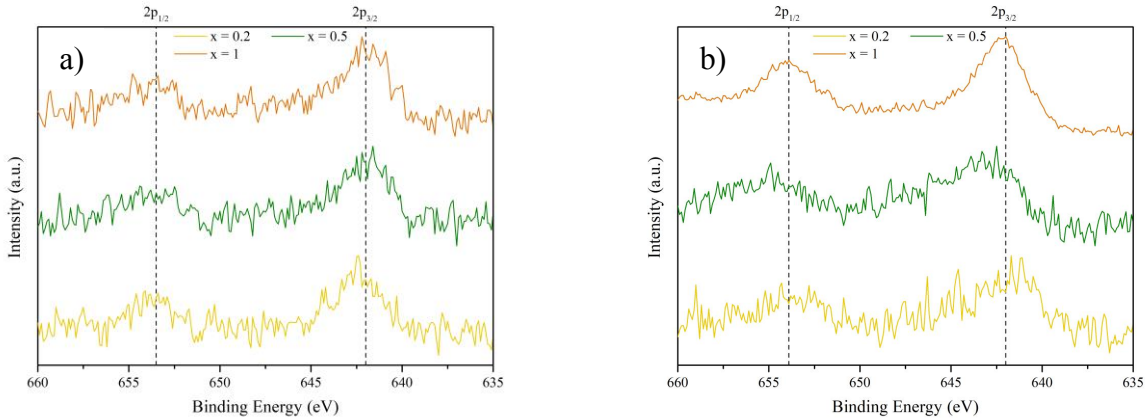

Spectrum 4.5: high resolution analysis of Mn2p peak after (a) and before (b) reaction.

The detailed analysis of Mn2p photopeaks has confirmed what previously considered in *Paragraph 4.2.3*, that is the less prevalent segregation character in the x = 1 sample after the RWGS reaction, especially if compared to the fresh sample. This can support the considerations reported in *Paragraph 4.2.1* of reduction of the MnO impurities by means of the hydrogen-rich reaction atmosphere.

As observed in *Table 4.1* the amount of manganese in the fresh samples is lower than the expected value and a further decrease is observed after reaction, except for sample x = 0.2. The position of $2p_{3/2}$ and $2p_{1/2}$ features were reported to be 642.2 eV and 653.1 eV, so with a shift at lower binding energy of both the contributes in respect to the fresh sample XPS spectra. The assignation of the position, although, is not easy as the signal intensity is not high. However, the shift toward lower binding energies suggests a less oxidized environment, that could be consistent with the surface segregation of molybdenum as oxide.

4.2.4.4 Molybdenum XPS spectra

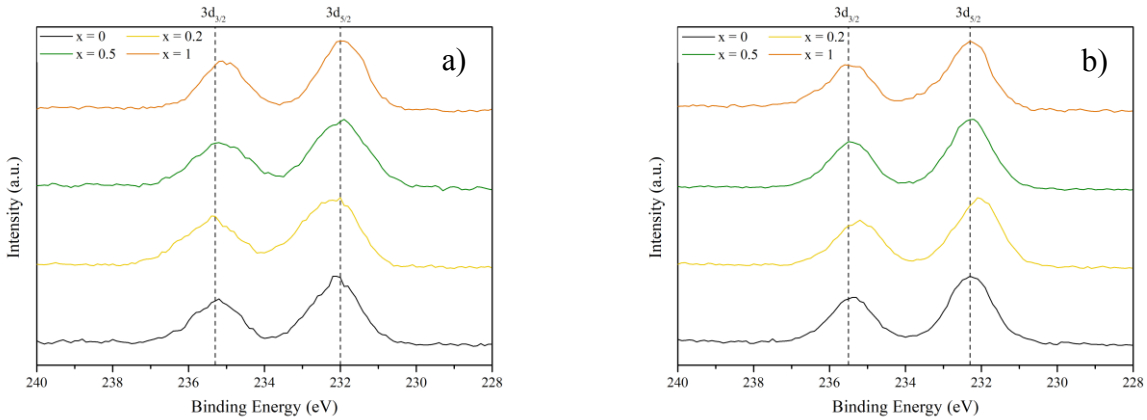

Spectrum 4.6: high resolution analysis of Mo3d peak after (a) and before (b) reaction.

The comparison of the 3d photopeak of molybdenum cation (*Spectrum 4.6*) before and after reaction indicates that the peaks positions have not changed and are reported to be at binding energy values of 232.2 eV and 235.4 eV, respectively for the $3d_{5/2}$ and $3d_{3/2}$ components and correspond to the presence of Mo (VI) in oxides.

4.2.4.5 Oxygen XPS spectra

The XPS spectra of oxygen, as it can be visualised in *Spectrum 4.7*, is again characterized by three main contributions, due to metal oxides, carbonates and other contributions due to oxygen coming from the quartz wool. The binding energy values, respectively of 529.9 eV, 531.3 eV and 532.8 eV are in agreement with what other works have reported. [21]

The metal carbonate contribution was the main one in all samples, but the quantification of the carbonate contribution, reported in *Table 4.3*, has shown a dramatic decrease in carbonate-oxygen content, denoting an overall decrease in carbonate impurities. It is also noteworthy underlining the increase of the contribution located at 532.8 eV. While in the fresh sample analysis it was correlated with the presence of highly oxydrilated species [22] (that have been thermally removed in the reaction environment), after the reaction it can be correlated with the oxygen coming from the quartz wool used for the reaction bed preparation. [23]

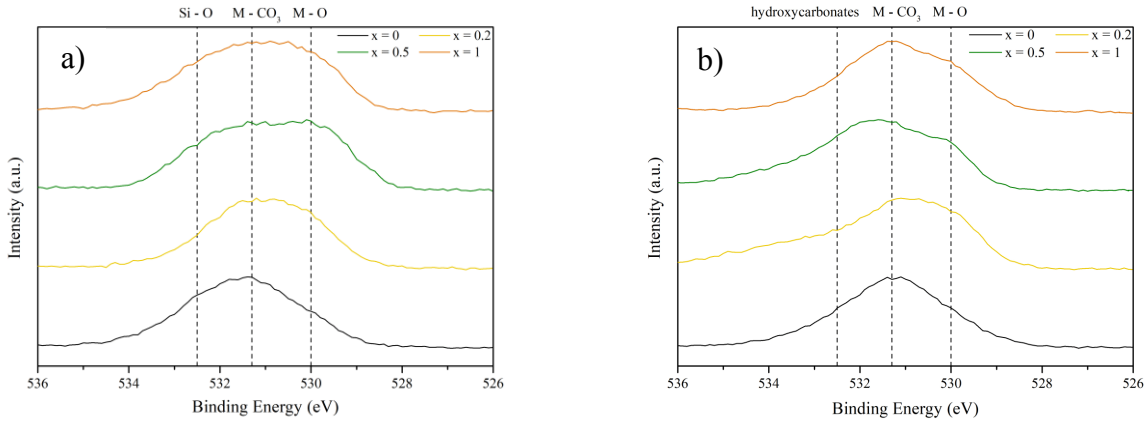

Spectrum 4.7: high resolution analysis of O1s peak after (a) and before (b) reaction.

4.2.4.6 Carbon XPS spectra

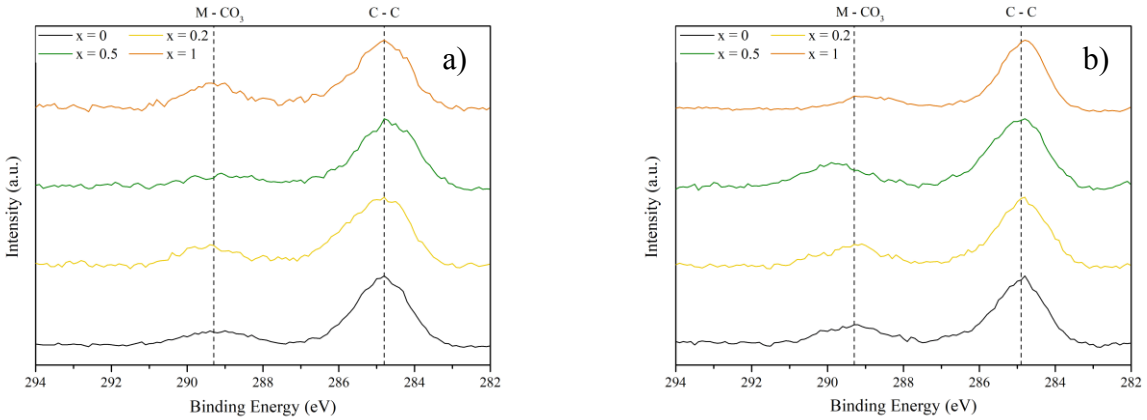

Spectrum 4.8: high resolution analysis of C1s peak after (a) and before (b) reaction.

Two main features were shown by the detailed analysis of C1s photopeak in *Spectrum 4.8*. The relative positions of the two features, being the one at 284.8 eV related to C – C bond and the one at 289.5 eV related to metal carbonate species on the sample surface [24], have been kept, with the only exception of the x = 0.5 sample, in which the metal carbonate contribution has shifted at lower binding energy following the reaction treatment.

As reported in *Table 4.3* and already discussed in *Paragraph 4.2.3*, a general decrease in carbonate species has been observed, with the only exception of x = 1 sample, denoting its scarce cyclability. This result is again in support of the utilisation of the SMMO materials as catalyst for the RWGS reaction, as its carbonation after the first cycle is negligible; however, longer reaction cycles should be performed for better evaluate the durability of the sample.

References

1 D. Hong, T. Kawanishi, Y. Tsukakoshi, H. Kotani, T. Ishizuka and T. Kojima, Efficient Photocatalytic CO_2 Reduction by a Ni(II) Complex Having Pyridine Pendants through Capturing a Mg^{2+} Ion as a Lewis-Acid Cocatalyst, *J. Am. Chem. Soc.*, 2019, **141**, 20309–20317.

2 M. Isegawa and A. K. Sharma, CO_2 reduction by a Mn electrocatalyst in the presence of a Lewis acid: a DFT study on the reaction mechanism, *Sustainable Energy Fuels*, 2019, **3**, 1730–1738.

3 M. Ezbiri, V. Becattini, M. Hoes, R. Michalsky and A. Steinfeld, High Redox Capacity of Al-Doped $La_{1-x}Sr_xMnO_{3-\delta}$ Perovskites for Splitting CO_2 and H_2O at Mn-Enriched Surfaces, *ChemSusChem*, 2017, **10**, 1517–1525.

4 Q.-H. Wu, M. Liu and W. Jaegermann, X-ray photoelectron spectroscopy of $La_{0.5}Sr_{0.5}MnO_3$, *Materials Letters*, 2005, **59**, 1980–1983.

5 G. Song, X. Zhu, R. Chen, Q. Liao, Y.-D. Ding and L. Chen, An investigation of CO_2 adsorption kinetics on porous magnesium oxide, *Chemical Engineering Journal*, 2016, **283**, 175–183.

6 D. Kobayashi, H. Kobayashi, K. Kusada, T. Yamamoto, T. Toriyama, S. Matsumura, S. Kawaguchi, Y. Kubota, M. Haneda, S. M. Aspera, H. Nakanishi, S. Arai and H. Kitagawa, Boosting reverse water-gas shift reaction activity of Pt nanoparticles through light doping of W, *J. Mater. Chem. A*, 2021, **9**, 15613–15617.

7 M. Zhu, Q. Ge and X. Zhu, Catalytic Reduction of CO_2 to CO via Reverse Water Gas Shift Reaction: Recent Advances in the Design of Active and Selective Supported Metal Catalysts, *Trans. Tianjin Univ.*, 2020, **26**, 172–187.

8 R. Tang, Z. Zhu, C. Li, M. Xiao, Z. Wu, D. Zhang, C. Zhang, Y. Xiao, M. Chu, A. Genest, G. Rupprechter, L. Zhang, X. Zhang and L. He, Ru-Catalyzed Reverse Water Gas Shift Reaction with Near-Unity Selectivity and Superior Stability, *ACS Mater Lett*, 2021, **3**, 1652–1659.

9 M. D. Porosoff, B. Yan and J. G. Chen, Catalytic reduction of CO_2 by H_2 for synthesis of CO, methanol and hydrocarbons: challenges and opportunities, *Energy & Environmental Science*, 2016, **9**, 62–73.

10 D. A. Osinkin, E. V. Zabolotskaya, D. G. Kellerman and A. Yu. Suntsov, The physical properties and electrochemical performance of Ca-doped $Sr_2MgMoO_{6-\delta}$ as perspective anode for solid oxide fuel cells, *J Solid State Electrochem*, 2018, **22**, 1209–1215.

11 D. Marrero-López, J. Peña-Martínez, J. C. Ruiz-Morales, M. C. Martín-Sedeño and P. Núñez, High temperature phase transition in SOFC anodes based on $Sr_2MgMoO_{6-\delta}$, *Journal of Solid State Chemistry*, 2009, **182**, 1027–1034.

12 D. Sun, L. Peng, K. Cheng, Y. Zheng and S. P. Jiang, Comparative study of manganese oxides with different oxidation states for catalytic carbonylation of n-butylamine by CO_2, *Journal of CO_2 Utilization*, 2023, **68**, 102382.

13 H. S. Lim, M. Lee, Y. Kim, D. Kang and J. W. Lee, Low-temperature CO_2 hydrogenation to CO on Ni-incorporated $LaCoO_3$ perovskite catalysts, *International Journal of Hydrogen Energy*, 2021, **46**, 15497–15506.

14 W. Jung and H. L. Tuller, Investigation of surface Sr segregation in model thin film solid oxidefuel cell perovskite electrodes, *Energy Environ. Sci.*, 2012, **5**, 5370–5378.

15 B. Koo, K. Kim, J. K. Kim, H. Kwon, J. W. Han and W. Jung, Sr Segregation in Perovskite Oxides: Why It Happens and How It Exists, *Joule*, 2018, **2**, 1476–1499.

16 S.-Y. Chung, S.-Y. Choi, H.-I. Yoon, H.-S. Kim and H. B. Bae, Subsurface Space-Charge Dopant Segregation to Compensate Surface Excess Charge in a Perovskite Oxide, *Angewandte Chemie International Edition*, 2016, **55**, 9680–9684.

17 R. D. Shannon, Revised effective ionic radii and systematic studies of interatomic distances in halides and chalcogenides, *Acta Cryst A*, 1976, **32**, 751–767.

18 C. S. Dandeneau, Y. Yang, B. W. Krueger, M. A. Olmstead, R. K. Bordia and F. S. Ohuchi, Site occupancy and cation binding states in reduced polycrystalline $Sr_xBa_{1-x}Nb_2O_6$, *Appl. Phys. Lett.*, 2014, **104**, 101607.

19 M. Wells, B. Zou, A. Mihai, R. Bower, A. Regoutz, S. Fearn, S. Maier, N. M. Alford and P. Petrov, Multiphase strontium molybdate thin films for plasmonic local heating applications, *Optical Materials Express*, DOI:10.1364/OME.8.001806.

20 D. A. Pawlak, M. Ito, M. Oku, K. Shimamura and T. Fukuda, Interpretation of XPS O (1s) in Mixed Oxides Proved on Mixed Perovskite Crystals, *J. Phys. Chem. B*, 2002, **106**, 504–507.

21 Oxygen | XPS Periodic Table - IT, https://www.thermofisher.com/uk/en/home/materials-science/learning-center/periodic-table/non-metal/oxygen.html.

22 M. Mullet, V. Khare and C. Ruby, XPS study of Fe(II)/Fe(III) (oxy)hydroxycarbonate green rust compounds, *Surface and Interface Analysis*, 2008, **40**, 323–328.

23 J.-C. Lee, S.-J. Oh, M. Cho, C. S. Hwang and R. Jung, Chemical structure of the interface in ultrathin HfO_2/Si films, *Applied Physics Letters*, 2004, **84**, 1305–1307.

24 Carbon | XPS Periodic Table - IT, https://www.thermofisher.com/uk/en/home/materials-science/learning-center/periodic-table/non-metal/carbon.html.

5. Cell design and manufacturing processes

The following chapter will be dedicated to the description of the SOFCs' design and construction procedures, together with the technical issues that had to be overcome. In particular, a full description of the realisation of a symmetrical cell will be carried out.

5.1 SOFC configurations

The cell applications usually define the design of the device itself; nevertheless, among all the possible configurations two are the mostly used: the planar and the tubular design. In recent studies, however, it has been tried to overcome the limitations that are proper of these designs.

5.1.1 Tubular design

The tubular design is usually employed in high temperature SOFCs and is the most present in market-ready devices for stationary applications. It is made of a cathode tube, usually composed of $LaMnO_3$, covered by a layer of electrolyte that is in turn coated with an anode layer, as shown in *Figure 5.1*.

The management of the gas fluxes is easy, as the gases flow in the same direction (one internally of the cell and one externally). The current collector is placed alongside the tube so the current flows through the tube and can be collected at the ends of the cell, leading to easier cable management.

These types of cells can work for long periods under different operating conditions with less than 0.1% performance degradation per 1000 h of working-time, but with low power density (as high as 1 W/cm^2), making these devices not suitable for mobile applications.

Nevertheless, some drawbacks are also present, the principal being the difficulty in the production of the ceramic cylinder with a good uniformity between the different layers.

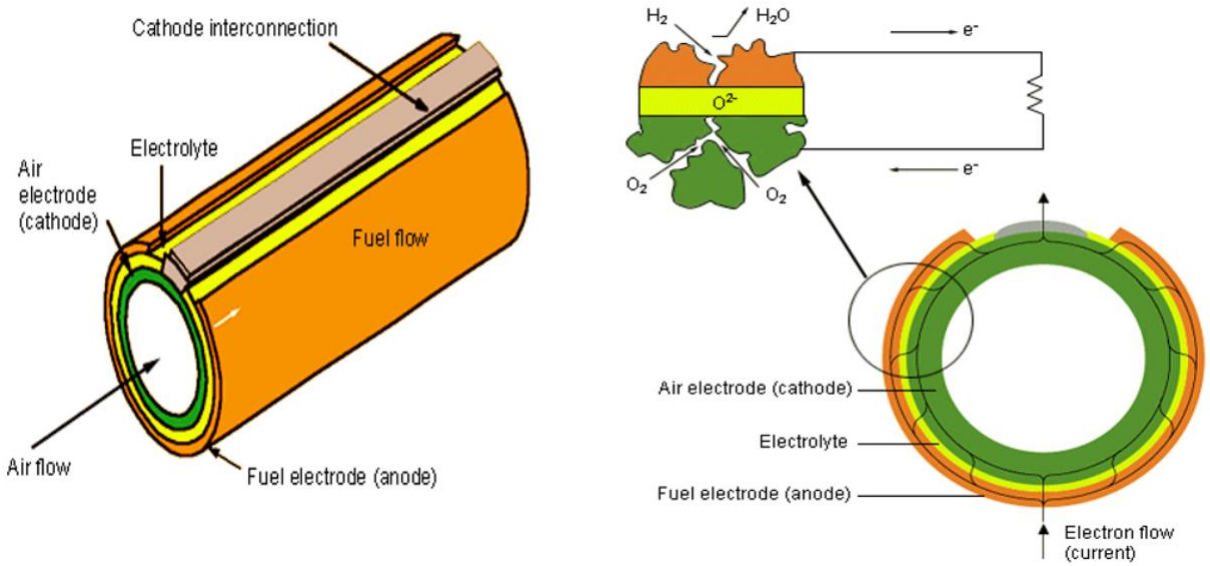

Figure 5.1: tubular configuration of a SOFC. [1]

5.1.2 Planar design

This configuration finds primary application in research due to its straightforward construction. Furthermore, it enables the attainment of a high-power density, approximately 2 W/cm^2, nearly twice that of tubular SOFC.

The planar arrangement comprises either a singular or multiple stacks, consisting of individual units or planar layers that are iteratively replicated. Illustrated in *Figure 5.2*, the individual layer is constituted by the cell positioned at the structure centre and two interconnects flanking the core. This arrangement provides both structural integrity and pathways for fuel to access the two electrodes. Additionally, the interconnects function as current collectors and serve as foundational components for stacking diverse cells atop one another. The design of the interconnects facilitates perpendicular flows of air and fuel, allowing for the creation of a compact stack.

Layer construction offers versatility through various techniques, including tape casting, screen-printing, slurry sintering, and even plasma spraying. Additionally, mechanical support for the layer can be provided from the anode, cathode, or electrolyte, achieved by utilizing support materials with bulkier dimensions compared to the other two. The most reliable and efficient configuration, however, has been demonstrated to be the anode-supported configuration. This preference is attributed to the inherent mechanical stability of commonly used anode materials.

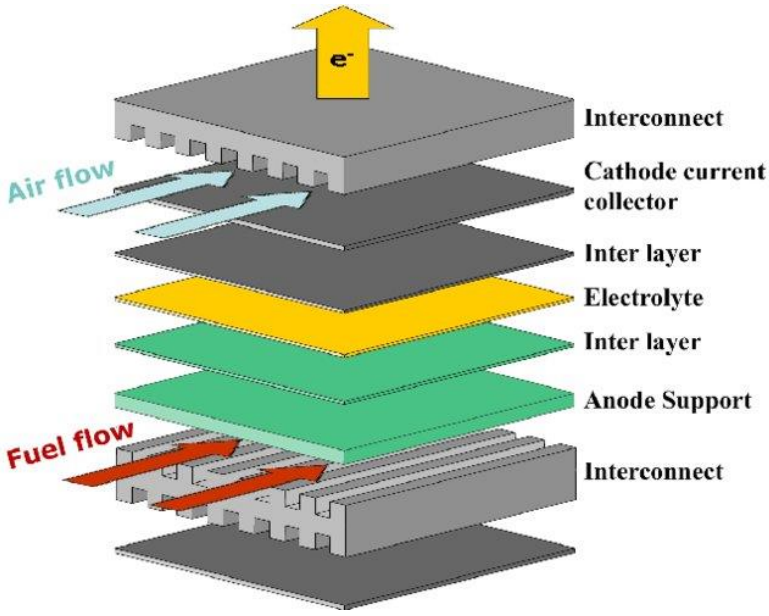

Figure 5.2: planar configuration of a SOFC. [2]

Furthermore, reducing the thickness of the electrolyte material not only enhances the cell mechanical stability but also decreases ohmic resistance, enabling a reduction in operating temperatures.

5.2 Cells construction

This work has opted for the button planar design due to its ease of implementation in the laboratory facilities. This configuration is commonly employed in research applications. The differences between this cell and the basic planar design are attributed to the smaller dimensions of the button planar and variations in electrical connections. Notably, the button SOFC functions is an independent device and is not part of any stack.

The primary advantage of adopting this design is the minimal quantity of materials required for constructing the device, making it suitable for laboratory-scale use but impractical for industrial applications due to its size. However, a drawback is the relatively high thickness of the electrolyte, which can compromise overall cell performance. Nevertheless, once optimal performance is achieved, there is the possibility of upscaling materials to construct a cell suitable for industrial use.

5.2.1 Choice of the electrolyte: compatibility and adhesion tests

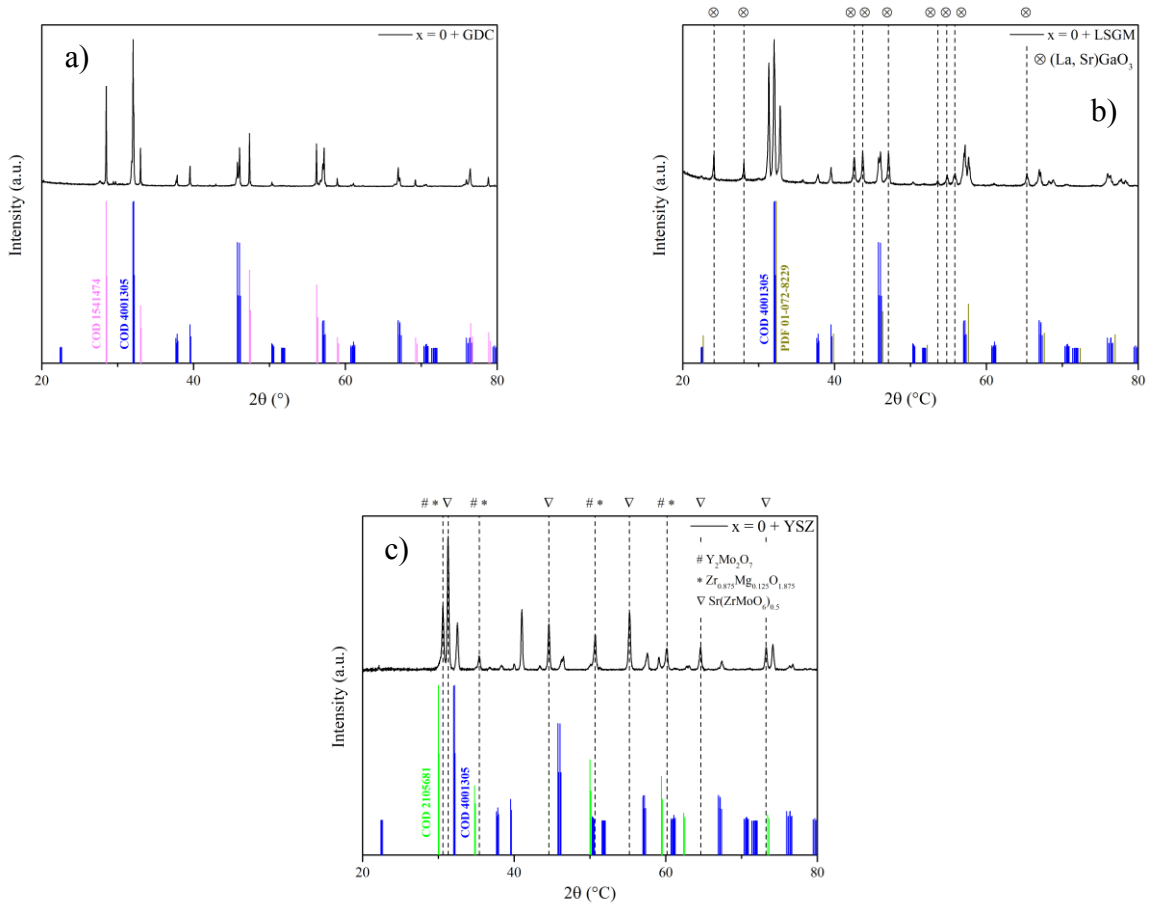

Diffractogram 5.1: XRD analysis of the SMMO materials and its compatibility with GDC (a), LSGM (b) and YSZ (c)

In order to have a full comprehension of the most suitable electrolyte for the cell construction, three different samples were prepared for a series of thermal and atmosphere treatments, thus allowing an evaluation of the optimal steps and conditions needed.

Specifically, the specimens were created through the manual blending and grinding of Sr_2MgMoO_6 material with laboratory-available anionic-conductive powders - namely LSGM (strontium and magnesium-doped lanthanum gallate), YSZ (Yttria-Stabilized Zirconia) and GDC (Gadolinium-Doped Ceria) - in a weight ratio of 50%-50%. The mixed powders were lately subjected to a calcination at 1200°C in air (ramp of 5°C/min), followed by a second calcination in a 5% H_2 reducing atmosphere (again ramp of 5°C/min).

The XRD analyses of the treated samples (*Diffractogram 5.1*) have given clear evidence of the impossibility of using YSZ as electrolyte, as all the perovskitic – and desired – phase has disappeared, and the formation of oxide phases (together with an unknown phase) was evinced (*c*). The LSGM + SMMO sample analysis (*b*) has shown, instead, the partial transition of the perovskitic phase to a

gallate – and insulator – phase; this phase is commonly reported in other works that imply the utilisation of SMMO materials as anode in SOFCs and it is responsible for the drop of about 50% of the cell performances. Being LSGM a promising electrolyte in SOFC applications, the solution of the compatibility issue is given by the application of a LDC buffer layer, that ensures a good conductivity, both ionic and electronic. [3] Eventually, GDC was found to be the optimal electrolyte material, as the diffractogram has shown the presence of no spurious phases (*a*).

The previous considerations have led to two construction routes, the first involving LSGM and the second involving GDC as electrolyte materials. Therefore, 2.5 g the two materials powders were uniaxially pressed into a circular pellet, with a 25 mm diameter; after some attempts made with the aim to optimize the applied pressure, these values turned out to be 4 tons for LSGM and 3.5 tons for GDC. The pellets were then sintered in air at 1500°C for 8 hours, but dividing the process in two steps: a first one from room temperature up to 1100°C with a ramp of 5°C/min and then from 1100°C/min to 1500°C/min with a ramp of 3°C/min. The sintered pellets were finally polished with a fine grit sandpaper until obtaining a smooth surface, and then cleaned in an ethanol with an ultrasonic bath before the electrode deposition.

The deposition process was made by tape casting of the electrode ink. The ink was prepared by mixing the electrode powder together with a polymer binder (α-therpineol) and carbon soot in a previously optimized ratio of 2:1:0.09. The deposition process, however, was different between the two electrolytes; the two methods have, however, not succeeded, both in terms of adhesion and mechanical resistance.

- LSGM: after the polishing and cleaning treatment, a layer of a LDC ink was deposited onto the pellet surface. The LDC ink was obtained following the same specification of the electrode ink. The buffer layer has then undergone sintering at 1275°C in air for 6 hours (ramp of 5°C/min) before the deposition of the electrode ink. A final sintering step was performed at 1200°C for 6 hours, in air and then in a 5% H_2 in Ar atmosphere.
- GDC: the electrode ink was directly deposited onto the pellet surface and then sintered at 1200°C for 6 hours (ramp of 5°C/min), in air and then in a 5% H_2 in Ar atmosphere.

Focusing on the LSGM-path, there was no evidence of mechanical failure of the pellet, but there was no adherence of the inks; a second attempt was performed, with a 3°C/min ascending and descending ramp, but the LDC buffer layer was completely removed during the deposition of the SMMO ink, showing again the evidence of no adhesion.

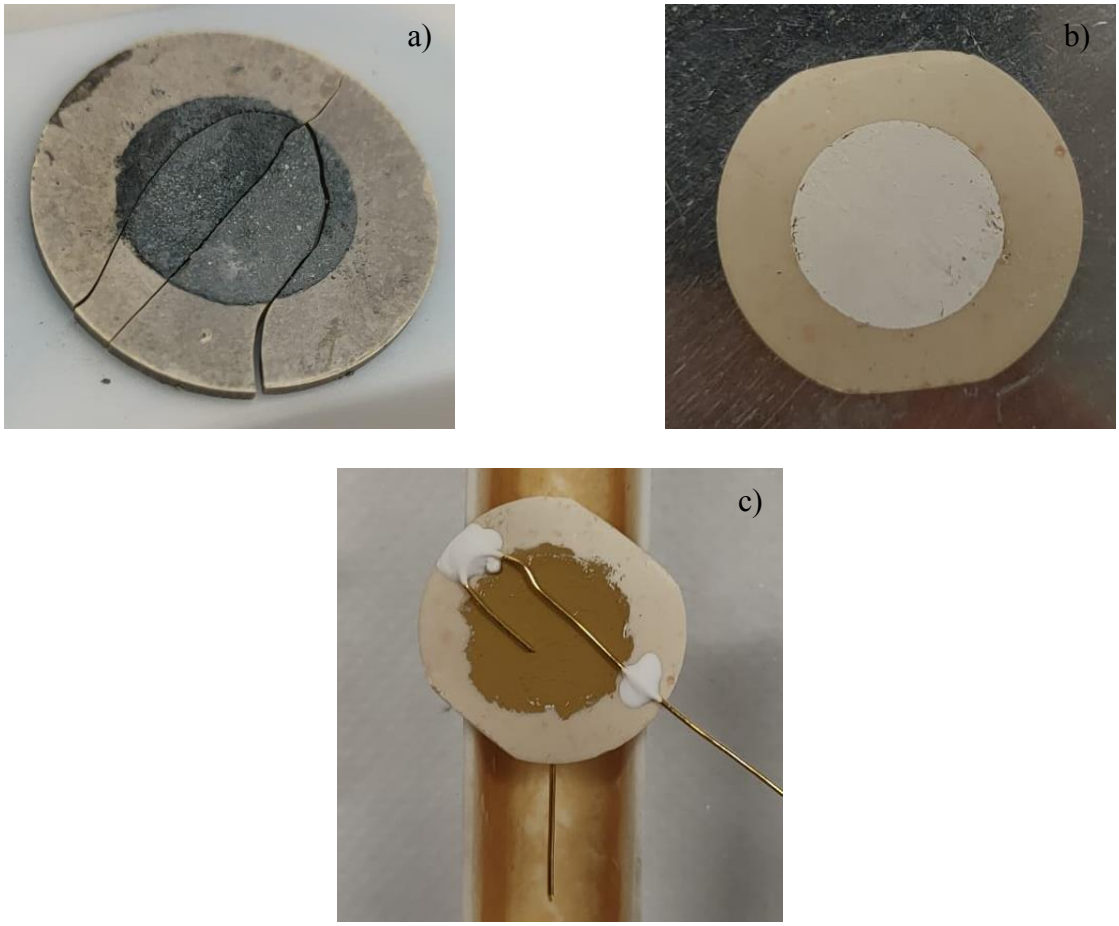

Figure 5.3: breaking of the 70-30 GDC-SMMO cell after the exposure to reducing atmosphere (a); in air-sintered 70-30 GDC-SMMO ink (b); final symmetrical cell (c).

For what concerns the utilisation of GDC, the reducing-sintering step has shown, together with the complete non-adhesion of the electrode ink, a dramatic mechanical failure of the pellet, showing the need of avoiding the use of a H_2-rich atmosphere at high temperatures. The responsible of the complete breaking of the pellet is possibly the reduction of Ce (IV) to Ce (III), that is reported to take place at around 900°C and is responsible for the enlarging of the crystalline cell, thus generating strain in the pellet [4]. The effects of the synthetised electrode powder on GDC reduction temperature are however unknown, as there was no possibility to investigate it. A second attempt has been made by sintering only in air, confirming the hydrogen-rich atmosphere to be responsible for the pellet breaking but again with scarce results in terms of sticking. Clearly, following the consideration made in *Chapter 3*, the oxidizing atmosphere leads to the formation of impurity phases, that could possibly lower the cell performances. Several attempts have followed, in which the variables were sintering temperature, electrode-electrolyte powder ratio and carbon soot content; this last two contributions have proved to be the key for the cell construction. In fact, the complete removal of carbon soot in the ink preparation was found to be mandatory to have a perfect sticking of the electrode. Moreover,

the adhesion was boosted by mixing electrode and electrolyte powders; the experimental value that was found to be optimal was 70% GDC and 30% SMMO powder.

The assurance of electrical contacts was achieved by applying a layer of gold paste onto the sintered ink, serving as a current collector. Two gold wires, mandatory to put in contact the cell and the impedance spectrometer used for electrochemical analysis of the cell, were then attached with a ceramic paste to both the cell sides. A final thermal treatment at 800°C (no dwell time, 3°C/min ramp both in ascending and descending) was carried out to eliminate organic residuals present in the gold paste.

5.3 Cell mounting

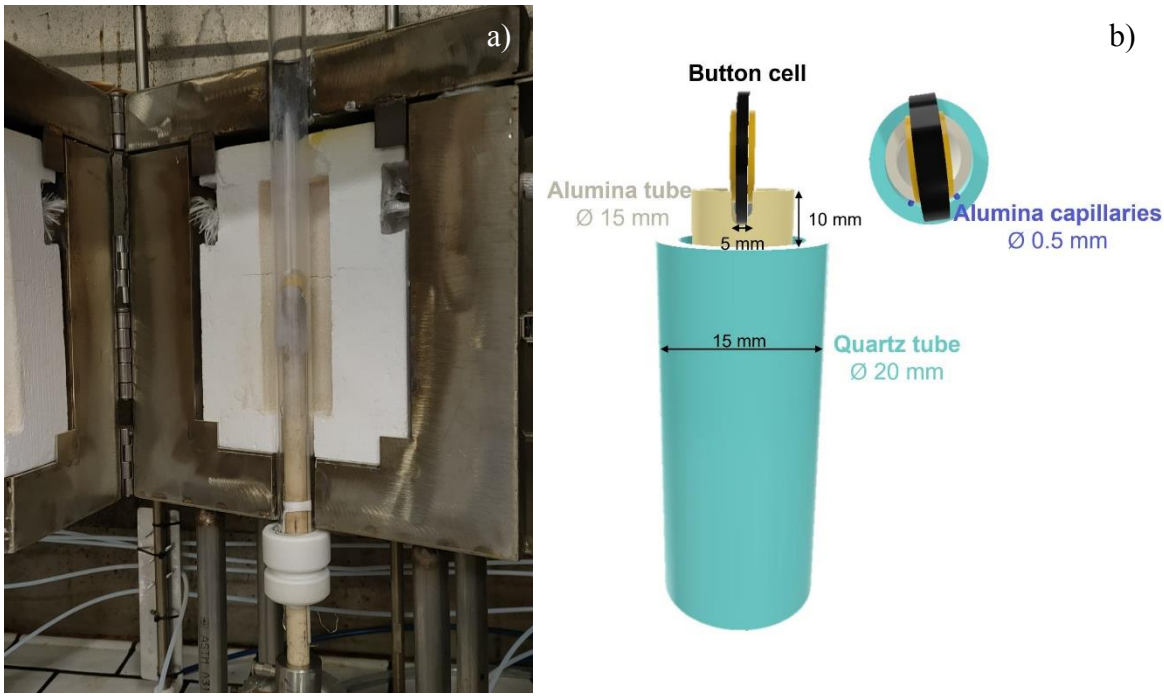

Figure 5.4: mounting of the single chamber set-up in the oven (a); details of the single chamber set-up (b).

The cell was finally mounted vertically in a dedicated single chamber set-up, in which the cell has been supported by an α-alumina DEGUSSIT AL23 tube covered by a quartz tube to isolate the chamber. The position of the cell is fundamental, because a good exposure to the fuel atmosphere is desirable. The fuel has been injected on the bottom of the chamber, while the exit is on top of it. Platinum wires present on the ceramic tube have been connected to the golden wires on the cell to establish a consistent electron pathway. A AISI 316 (austenitic steel with molybdenum alloy) oven has been utilized. This oven possesses an internal cavity, in which the chamber and two K-type thermocouple with the purpose of temperature control were inserted.

References

1 Y. Alyousef and K. Kendall, Characterization of the electrochemical performance of micro-tubular solid oxide fuel cell (SOFC), *Journal of Taibah University for Science*, 2009, **2**, 14–21.

2 D. Chen, H. He, D. Zhang, W. Hanzhi and M. Ni, Percolation Theory in Solid Oxide Fuel Cell Composite Electrodes with a Mixed Electronic and Ionic Conductor, *Energies*, 2013, **6**, 1632–1656.

3 Y.-H. Huang, R. I. Dass, J. C. Denyszyn and J. B. Goodenough, Synthesis and Characterization of $Sr_2MgMoO_{6-\delta}$, *Journal of The Electrochemical Society*.

4 I. Yentekakis, G. Goula, P. Panagiotopoulou, S. Kampouri, M. Taylor, G. Kyriakou and R. Lambert, Stabilization of catalyst particles against sintering on oxide supports with high oxygen ion lability exemplified by Ir-catalyzed decomposition of N_2O, *Applied Catalysis B: Environmental*, DOI:10.1016/j.apcatb.2016.04.011.

6. Electrochemical Impedence Spectroscopy (EIS) characterization of symmetrical cells

In this chapter, the electrochemical characterization of SMMO materials will be analysed and discussed.

The EIS measurements were performed in a single chamber device using a PGSTAT 302 Autolab Frequency Response Analyzer. The measuring facility set up was developed by IMPACT research group. Tests were carried out at steady state conditions (no DC current present) in the frequency range of 10^{-2}-10^{-6} Hz and with a signal amplitude of 20 mV.

6.1 EIS theory

Impedance spectroscopy stands as a crucial technique for assessing the electrochemical performance of materials in SOFCs. Its sensitivity is notably influenced by the configuration of the analysed cell and the fabrication procedures involved. For instance, the reliability of measurements hinges on the proper adhesion of all cell layers. Nonetheless, this method yields valuable data on the polarization processes within the studied material.

To enhance comprehension of the data obtained from SMMO materials, this paragraph briefly outlines essential concepts related to the Electrochemical Impedance Spectroscopy (EIS) procedure. Initiating the discussion with the portrayal of an ideal resistor is imperative. This resistor should consistently adhere to Ohm's law across various current and voltage levels, exhibit frequency-independent resistance, and ensure that the alternating current and voltage signals passing through it are in phase. Furthermore, Ohm's law should be representative of its typical behaviour:

$$R = \frac{V}{I} \tag{6.1}$$

However, actual resistors deviate from these ideal properties, displaying more intricate behaviours. Consequently, it becomes necessary to relinquish the simplistic notion of resistors in favour of a more comprehensive circuit parameter: impedance. Functioning as a form of resistance, impedance measures a circuit capacity to impede the internal flow of electric current, although with fewer constraints on its characteristics.

In impedance measurements, a sinusoidal alternating current potential is applied, resulting in the generation of a corresponding current. It is essential to maintain a small excitation signal to ensure

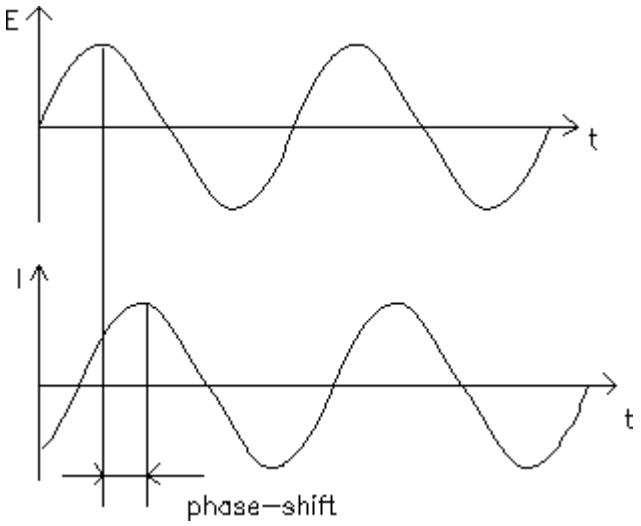

Figure 6.1: sinusoidal current response in a linear system (bottom), in relation to the excitation signal (top). [1]

a pseudo-linear cell response: the current reaction manifests as a sinusoid at the same frequency but with a phase shift (refer to *Figure 6.1*). Typically, the excitation signal is expressed as a time-dependent function (*Eq. 6.2*), where E_t represents the potential at time t, E_0 denotes the signal amplitude, and ω represents the radial frequency.

$$E_t = E_0 \sin(\omega t) \tag{6.2}$$

It is important to note that the relationship between the radial frequency (ω, expressed in rad/s) and the frequency (Hz) is linear:

$$\omega = 2\pi f \tag{6.3}$$

Therefore, within a pseudo-linear system, the responsive signal (I_t) should resemble the excitation signal but with a phase shift (φ). In this context, impedance (Z), acting as a resistance, can be characterized by an expression analogous to Ohm's law and expressed by terms of magnitude (Z_0) and phase shift (φ).

$$I_t = I_0 \sin(\omega t + \varphi) \tag{6.4}$$

$$Z = \frac{E_t}{I_t} = \frac{E_0 \sin(\omega t)}{I_0 \sin(\omega t + \varphi)} = Z_0 \frac{\sin(\omega t)}{\sin(\omega t + \varphi)} \tag{6.5}$$

Introducing the expression for the excitation potential (*Eq. 6.6*) and the Euler's relationship (*Eq. 6.7*),

$$E_t^c = E_0^c \exp(j\omega t) \tag{6.6}$$

$$\exp(j\varphi) = \cos(\varphi) + j \sin(\varphi) \tag{6.7}$$

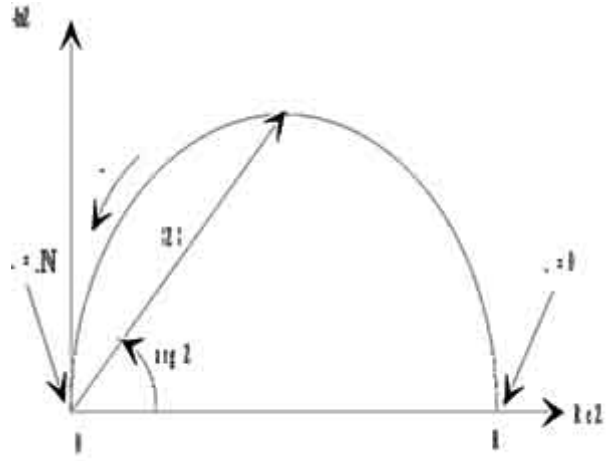

Figure 6.2: Nyquist plot with the impedance vector.

it is possible to re-arrange the expressions of current response and impedance by using complex numbers:

$$I_t^c = I_0^t \exp(j\omega t - \varphi) \tag{6.8}$$

$$Z = \frac{E_t^c}{I_t^c} = Z_0 \exp(j\delta) = Z_0[\cos(\delta) + j\sin(\delta)] \tag{6.9}$$

A useful method for the impedance analysis is the Nyquist plot (see *Figure 6.2*), in which the real part of impedance (*Eq. 6.10*) is placed on the x-axis while the imaginary part (*Eq. 6.11*) is located on the negative y-axis. The impedance can be represented as a vector of length *|Z|*, besides the angle between this vector and the x-axis is the "angle phase" and it is equal to the phase itself (φ). Each point of this plot corresponds to a precise frequency; higher frequencies are on the left-hand side of the plot, while lower frequencies stand on the right-hand side.

$$Z_{real} = Z_0 \cos(\delta) \tag{6.10}$$

$$Z_{imaginary} = j \cdot Z_0 \sin(\varphi) \tag{6.11}$$

The impossibility of registering the frequency at which every point was recorded is overcome by pairing the Nyquist plot with the Bode plot (*Figure 6.3*), in which impedance absolute value is plotted on the y-axis and the logarithm of the frequency stands on the x-axis.

The Nyquist plot provides lots of information, but this data is often challenging to directly visualize and comprehend. EIS data are typically analysed by fitting them with an equivalent electrical circuit model that incorporates conventional electrical components such as resistors, capacitors, and inductors. These elements serve as models to dissect the physical electrochemistry of the system [2]:

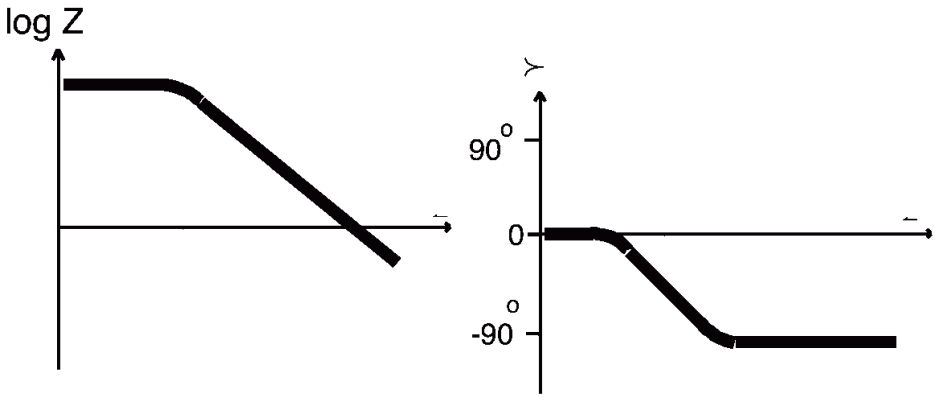

Figure 6.3: Bode plot; module (sx) and phase (dx).

- Resistors replicate ionic and electronic resistance, as well as charge and mass transfer resistance.
- Capacitors emulate dielectric polarization, double layer charge, and the accumulation of masses.
- Inductors simulate species absorption at the electrode surface.

When these standard elements fall short in replicating the Nyquist plot, two additional parameters, Warburg resistance and Constant Phase Elements (CPE), come into play:

- Warburg resistance mimics the contribution of diffusion phenomena to impedance.
- Constant Phase Elements (CPE) simulate phenomena associated with the roughness and porosity in a real electrode, including the uneven distribution of charges at the electrode. This parameter can even be employed to simulate the adsorption of impurities at the electrode sites.

The incorporation of the elements enables the extraction of key cell features such as Area Specific Resistance (ASR) or Capacitance (C). Furthermore, it provides a means to enhance understanding of the ongoing processes, for instance, by examining the frequency of the involved phenomena.

6.2 EIS anode characterization

Figure 6.4: equivalent circuit utilized for the curves fitting.

Symmetrical cells with SMMO-GDC electrodes and GDC as the electrolyte were tested to understand the electrochemical performances of the synthesized materials. Their configuration, following the consideration made in *Paragraph 5.2.1*, was 70% GDC/30% SMMO – GDC – 70% GDC/30% SMMO.

Two series of cell tests were performed: one with only Ar-diluted H_2 as fuel, to have a sort of benchmark of the materials' performances, and another with a gas mixture of 80% H_2/20% CO_2 diluted in Ar, to evaluate the effects of CO_2 presence in the fuel. The temperature range was between 600°C and 800°C, with 50°C steps in between; a stabilization of 15 minutes was needed in every step, in order to eliminate possible contributions derived from temperature.

The circuit that was utilized for the measurements (*Figure 6.4*) is composed of a resistor, in series with two sub-circuits made of a resistance in parallel with a CPE (this element can be also called R//CPE) and a resistance in parallel with a capacitor (R//C). The first resistance simulates the resistance of the electrolyte and it is given, in the Nyquist plot, by the intercept of the curve at high frequency, on the left of the spectra. The R//CPE and R//C circuits are used to describe some processes that are affected by different parameters, such as temperature, inlet fuel flux and even the inlet gas composition.

The low-frequency intercept, located on the right side of the spectra, provides the total resistance. This parameter encompasses the cell ohmic resistance, the resistance related to concentration polarization (an effect coming from mass-transfer or gas-diffusion phenomena), and the effective interfacial polarization resistance (a resistive contribution arising from electrochemical reactions at the interface between the electrode and electrolyte).

6.2.1 H_2 – in Ar – fuel

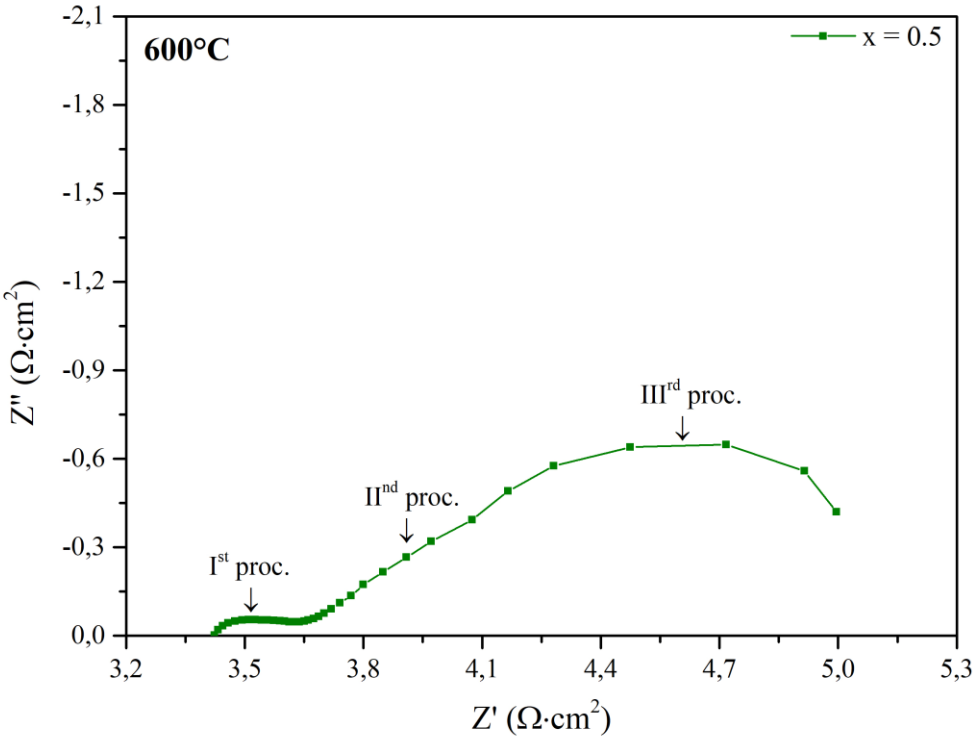

Graph 6.1: Nyquist plot of the x = 0.5 cell, in H_2 fuel, at 600°C.

As previously stated, the first series of electrochemical test were performed in a 10% H_2/90% Ar gas mixture, in order to have a first benchmark of the behaviour of the different materials. Moreover, the choice was to have a wet gas flux at the inlet, thus involving a bubbler in the gas path, to mitigate the effects of the reducing atmosphere on the GDC pellet. This is, although, negative in terms of cell performances, as supported by previous works. [3]

As reported in *Graph 6.1*, in which the specific x = 0.5 cell has been taken by example to better examinate the electrochemical behaviour of the device, three processes are visible. This tendency is present in all the different cells (with different composition concerning the electrode material), as shown in *Graph 6.2*. As a matter of facts, Nyquist plots are usually visualised with the same scale on both x- and y-axis, in order to fully evaluate the deviation from ideality of the device (an ideal conductor should be characterized by only the real part of impedance); in this particular case, a shorter scale was needed in y-axis because of the very small values of the imaginary part of impedance.

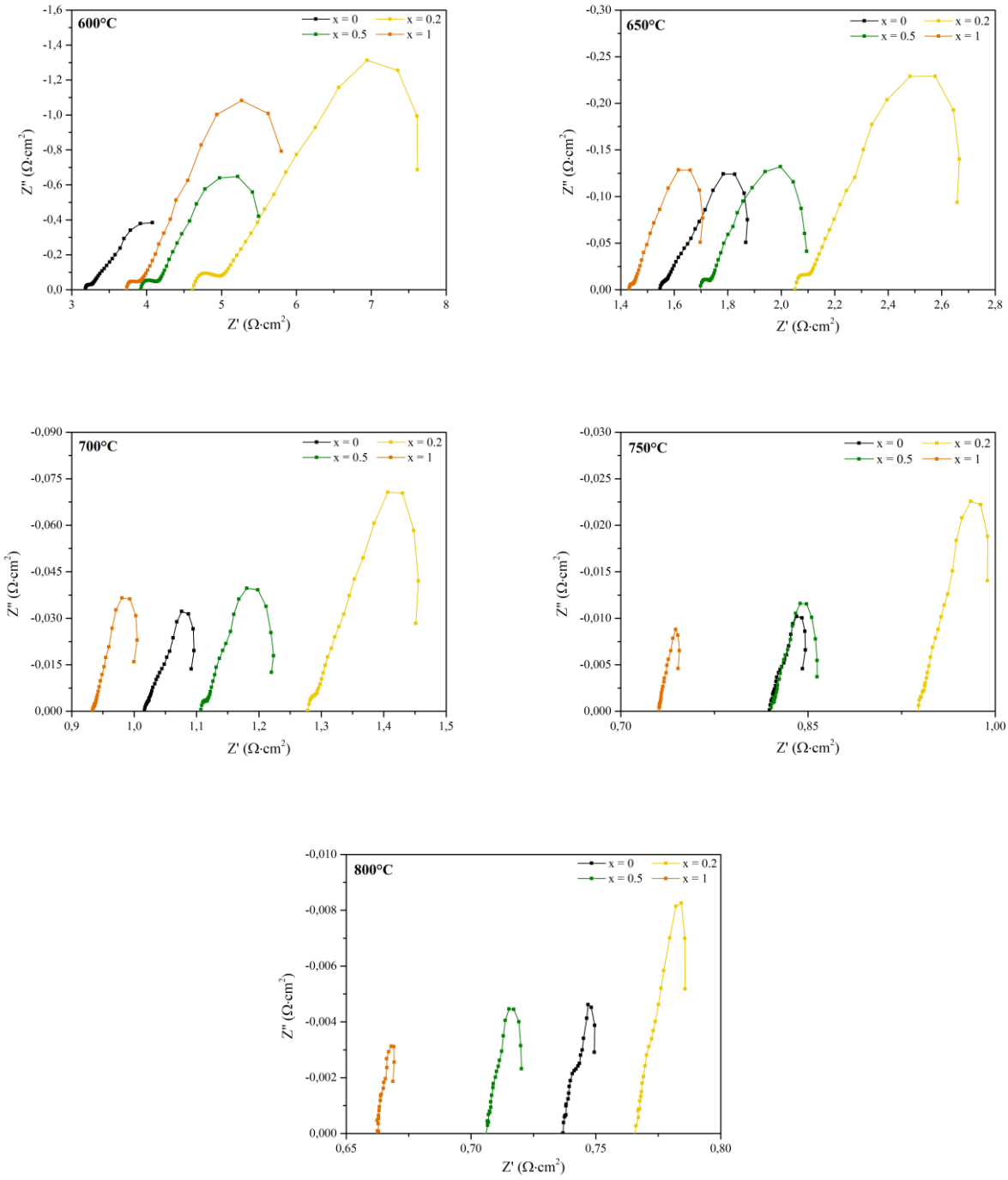

Graph 6.2: Nyquist plot of the SMMO materials' cells at different temperatures for a H_2-feeding gas mixture.

Nevertheless, this does not signify a resemblance to the behavior of an ideal resistor, given that the latter is defined by a resistance that is both linear and independent of frequency.

As every circuit associated to a process is related to a specific frequency, a proper way of comparison would be a Bode-phase plot, by means of which it is possible to evaluate how the processes behave with relation to the frequencies. However, being the Bode plot not easily distinguishable, they have

not been reported in this work. Another possible term of comparison could be the calculation of the capacitance value: to compare two phenomena, both of them should possess a similar capacitance (usually of the same order of magnitude). For this purpose, it is necessary to clarify the inclusion of a purely capacitive element in the equivalent circuit used for fitting EIS curves (*Figure 6.4*); as reported in the literature, it is quite common to observe supercapacitive behaviours in molybdenum-containing double perovskite structures, just as in the case of this work. [4,5] The inclusion of a capacitance, a necessary result to obtain the goodness of fit, is therefore useful to simulate this behaviour in SMMO materials.

The EIS spectra provide another parameter that can be derived, known as the Area-Specific Resistance (ASR) of the electrode corresponding to each process. ASR indicates the material resistance to the flow of electric current. Optimal ASR values for industrial use, especially with readily available materials, typically fall within the range of 10 $m\Omega \cdot cm^2$. [6]

The frequency results obtained has shown that the IInd and the IIIrd processes were characterized by the same frequencies in all cells, independently from the electrode materials; in particular, the IInd process, reported to take place at 0.2 Hz, is known in literature to be related to the slow dissociative hydrogen adsorption on the GDC surface [7,8], while the IIIrd one is related to supercapacitive phenomena typical of molybdenum-based double perovskite structures. [5] Furthermore, it is possible to theorize that this process is due to a reduction of the material driven by the reducing atmosphere, where the oxygen ions diffuse from the bulk to the surface of the material. For what concerns the Ist registered process, *Table 6.1* has shown that the characteristics frequency values are equal, with the only exception of the x = 0.2 cell, that has reported higher frequency values; moreover, the frequency value is reported to lower by increasing the temperature, and thus to be indicative of different electrochemical phenomena:

- at 600°C, the values in the range of kHz are related to charge transfer reaction; [9]
- at 650°C (and in general for T > 600°C in the x = 0.2 cell), a frequency in the range of the hundreds of Hz is indicative of Triple Phase Boundary (TPB) processes; [10]
- at T > 700°C, frequencies between 25 and 60 Hz indicates diffusion-related processes. [10]

Looking at the resistance values, *Graph 6.2* has clearly shown a non-constant value of the ohmic resistance, whose value is represented in the Nyquist plot by the x-axis intercept and should be characteristic of the electrolyte material at a given temperature, by changing the electrode material; this is an indication that the electrolyte conductive behaviour was strongly influenced by the exposure to the fuel atmosphere, that in principle should be equal in terms of time for all cells (even if an accuracy

	x = 0			x = 0.2		
Temperature (°C)	**Ist pr.**	**IInd pr.**	**IIIrd pr.**	**Ist pr.**	**IInd pr.**	**IIIrd pr.**
600	$1.6\cdot10^{3}$			$3.9\cdot10^{3}$		
650	$2.5\cdot10^{2}$			$4.0\cdot10^{2}$		
700	$6.0\cdot10^{1}$	$2\cdot10^{-1}$	$2.5\cdot10^{-2}$	$2.5\cdot10^{2}$	$2\cdot10^{-1}$	$2\cdot10^{-2}$
750	$4.0\cdot10^{1}$			$1.6\cdot10^{2}$		
800	$2.5\cdot10^{1}$			$1.0\cdot10^{2}$		

	x = 0.5			x = 1		
Temperature (°C)	**Ist pr.**	**IInd pr.**	**IIIrd pr.**	**Ist pr.**	**IInd pr.**	**IIIrd pr.**
600	$1.6\cdot10^{3}$			$3.9\cdot10^{3}$		
650	$2.5\cdot10^{2}$			$4.0\cdot10^{2}$		
700	$6.0\cdot10^{1}$	$2\cdot10^{-1}$	$2.5\cdot10^{-2}$	$2.5\cdot10^{2}$	$2\cdot10^{-1}$	$2\cdot10^{-2}$
750	$4.0\cdot10^{1}$			$1.6\cdot10^{2}$		
800	$2.5\cdot10^{1}$			$1.0\cdot10^{2}$		

Table 6.1: characteristic frequencies associated to the three processes in the cells.

to the second in starting the data acquisition was not possible to reach). [11] The ASR values have shown the typical decrease by increasing the operating temperature; in particular, a drop of one order of magnitude has been observed by increasing the operating temperature from 600°C to 650°C and could be related to a thermal-activated process. Nevertheless, a further hypothesis of short circuit of the devices at temperatures higher than 600°C has to be considered, even if the impedance spectra has shown three different processes; by looking at the current values with a multimeter, in fact, it seemed that the cell presence in the circuit was not influencing the current flow, but it is not clear if it is caused by an effective short circuit phenomena or by the low sensitivity of the multimeter itself.

The retrieved ASR values (*Table 6.2*) lie in the same magnitude order, and are thus comparable, to the ones reported for the state-of-the-art SOFCs anodes, i.e. Ni/YSZ. [12] It is mandatory to underline a short circuit phenomenon that has taken place above 700°C for the cell composed by a mixed GDC – Sr_2MnMoO_6 electrode, the cause of which is probably to be assigned to the reduction of Ce (IV) to Ce (III) and the consequent Mixed Ionic-Electronic Conductor (MIEC) behaviour of the electrolyte. However, no correlation between the manganese-doping degree and the cells' ASR was observed, meaning that the principal contribution to the cells' functioning is due to the MIEC behaviour of the electrolyte.

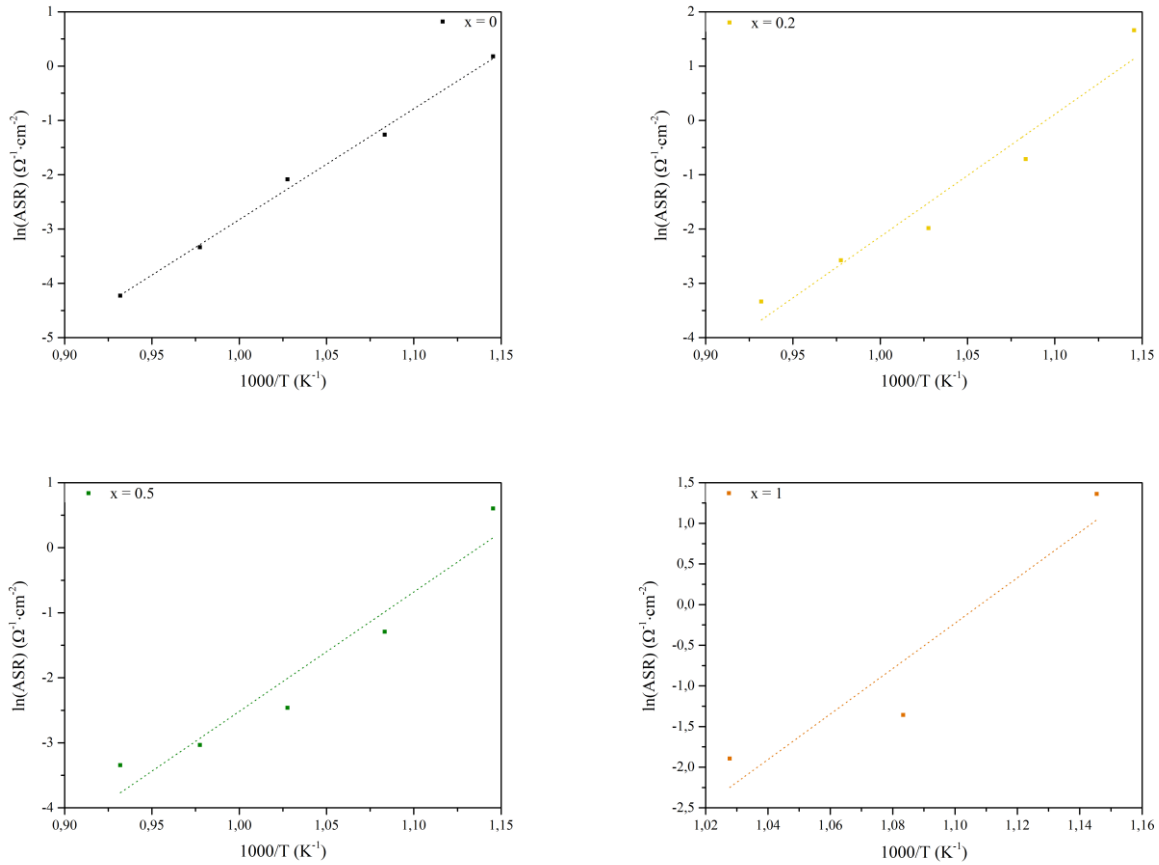

Graph 6.3: Arrhenius plots of the four different cells.

	ASR (Ω·cm²)			
Temperature (°C)	**x = 0**	**x = 0.2**	**x = 0.5**	**x = 1**
600	1.19	5.25	1.82	3.89
650	0.28	0.49	0.28	0.26
700	0.12	0.14	0.09	0.15
750	0.04	0.08	0.05	SC
800	0.02	0.04	0.04	SC

Table 6.2: ASR values of the different H_2-fed cells.

	E_a (eV)
x = 0	1.75
x = 0.2	1.94
x = 0.5	1.58
x = 1	2.40

Table 6.3: activation energy values calculated by the Arrhenius plots.

The activation energies (*Table 6.2*), retrieved by an Arrhenius Plot of the registered ASR values, are not in accordance with the literature values for the SMMO materials (around 0.95 eV); it is interesting observing the fact that E_a values are actually the sum of CGO and SMMO ones. [13,14]

A full evaluation of the performance of the electrode, however, is not possible for these devices because of the manufacturing method necessary for the cells production; to subtract the contribution of GDC, a "baseline" measurement should be carried out by testing only GDC as electrode.

6.2.2 $H_2 + CO_2$ – in Ar – fuel

The second part of the cells tests has implied the utilisation of an 80% H_2 – 20% CO_2 feeding gas mixture, again in an argon carrier atmosphere, with the aim to analyse the effects of CO_2 presence on the electrodes' performances. Again, a wet gas flux at the inlet was required, thus involving a bubbler in the gas path, to mitigate the effects of the reducing atmosphere on the GDC pellet.

As reported in *Graph 6.4*, in which the specific x = 0.5 cell has been taken as example to better examinate the electrochemical behaviour of the device, three processes are again visible in all the different cells (with different composition concerning the electrode material), as already discussed in the previous paragraph and again reported (a shorter scale was needed in y-axis because of the very small values of the imaginary part of impedance, however excluding the typical behaviour of ideal resistor because of the relation between resistance and frequency) in *Graph 6.5*.

The results, obtained by the fitting of the Nyquist plots (*Graph 6.5*) with the equivalent circuit characteristic also of the H_2 fuel, were characterized by the same three electrochemical processes reported in previous considerations (*Table 6.1*). Resuming the meaning of the processes:

- the Ist process is temperature dependent and thus involved different phenomena like
  - at 600°C, the values in the range of kHz are related to charge transfer reaction [9]
  - at 650°C (and in general for T > 600°C in the x = 0.2 cell), a frequency in the range of the hundreds of Hz is indicative of Triple Phase Boundary (TPB) processes [10]
  - at T > 700°C, frequencies between 25 and 60 Hz are symptoms of diffusion-related processes [10]
- the IInd process, reported to take place at 0.2 Hz, is known in literature to be related to the slow dissociative hydrogen adsorbtion on the GDC surface [7,8]
- the IIIrd one is related to supercapacitive phenomena typical of molybdenum-based double perovskite structures [5]

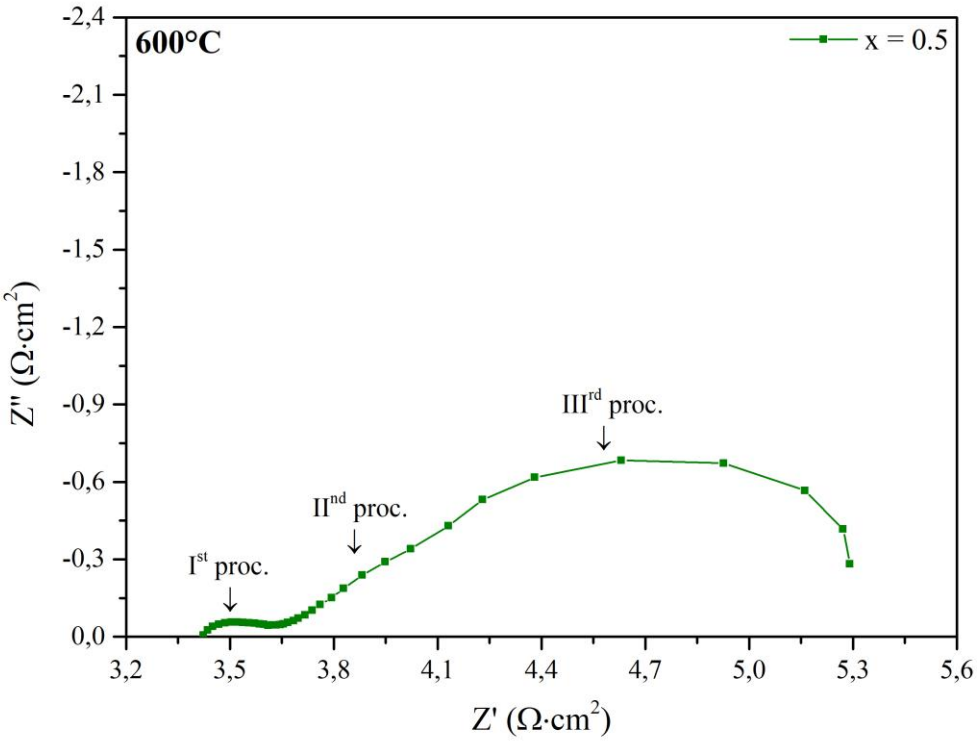

Graph 6.4: Nyquist plot of the x = 0.5 cell, in H_2 + CO_2 fuel, at 600°C.

	ASR (Ω·cm²)			
Temperature (°C)	**x = 0**	**x = 0.2**	**x = 0.5**	**x = 1**
600	2.10	2.02 *	2.24	1.81 *
650	0.32	1.11	0.36	1.28
700	0.08 *	0.57	0.12	0.58
750	SC	0.34	0.05	SC
800	SC	SC	0.02	SC

Table 6.4: ASR values of the different H_2 + CO_2-fed cells. SC stands for Short Circuit, while * indicates tests in which the 2nd process' resistance tends to infinity and its thus not considered.

From the resistances point of view, the first indication obtained graphically from the Nyquist plot in *Graph 6.5* is again the non-constant value of the x-axis intercept, namely the electrolyte resistance, meaning in a strong influence of the atmosphere exposure on the electrolyte behaviour. Moreover, the electrolyte resistances have shifted toward higher values with respect to the CO_2-free fuel; this is consistent with the partial utilization of the available hydrogen in the RWGS reaction, favoured by the previously observed and discussed catalytic activity of the electrode materials, and thus no more

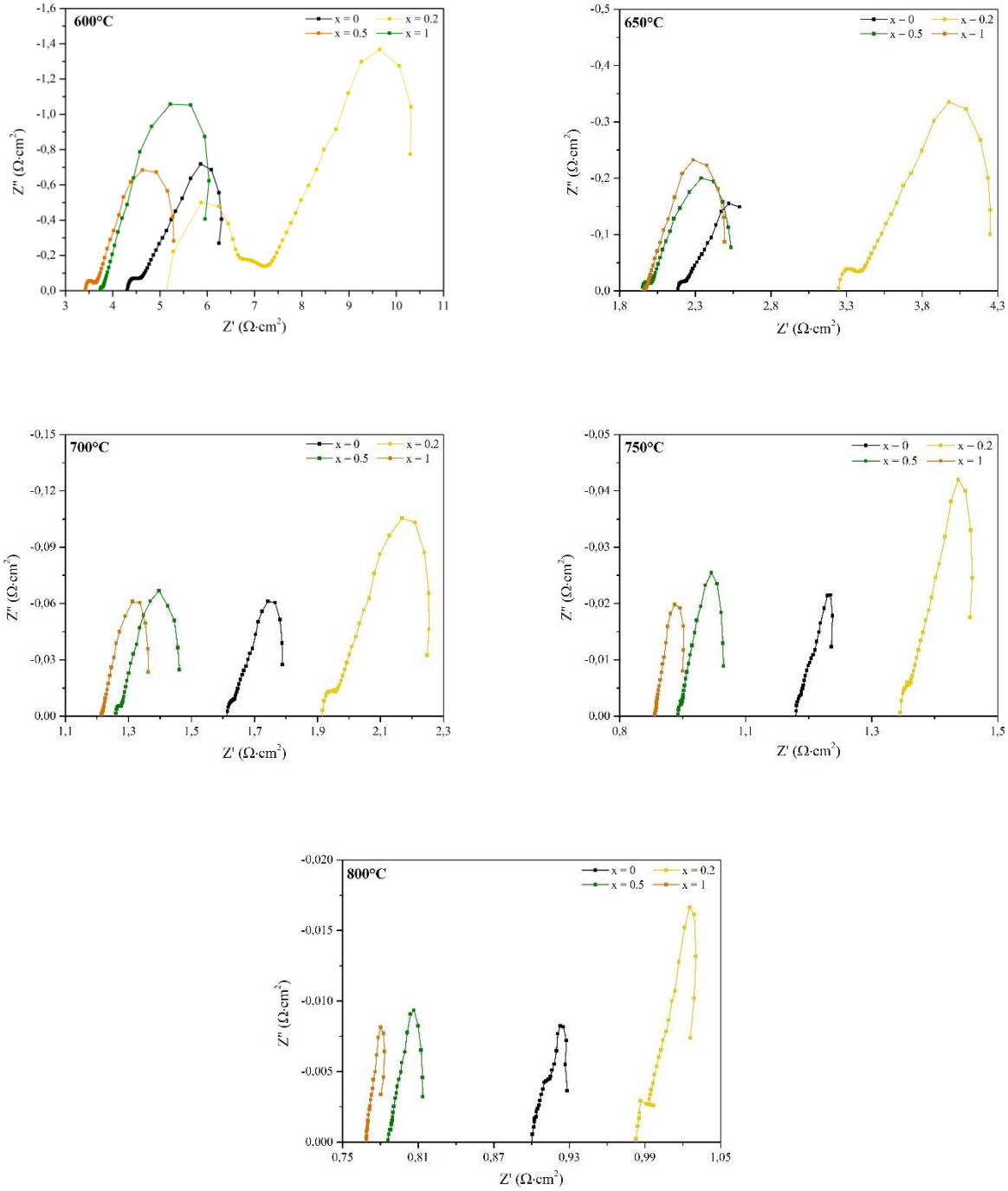

Graph 6.5: Nyquist plot of the SMMO materials' cells at different temperatures for a H_2-fuel.

available as proper fuel. No diluition by means of CO_2 was observed, as the absolute hydrogen quantity was kept equal in the two tests (10 sccm).

The phenomenon at the basis of these tests is not clear, principally because of the hypothetical short circuit caused by the exposure of GDC electrolyte to a H_2-rich atmosphere and the consequent reduction of Ce (IV) to Ce (III); in fact, beyond the already discussed short circuit phenomena at

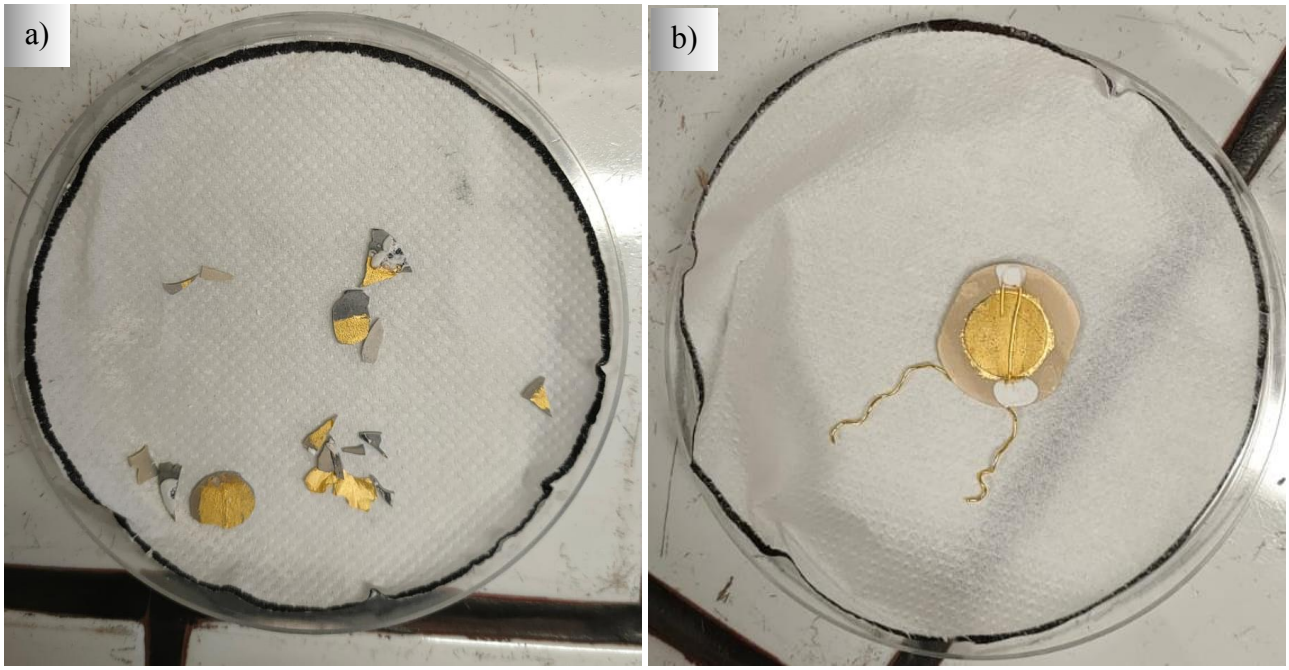

Figure 6.5: post-test image of x = 0.2 (a) and x = 0.5 (b) cells.

higher temperatures, in the x = 0.2 and 1 samples (signed with a * in *Table 6.4*) the second process was characterized by resistance tending toward infinity, a symptom of device failure. For these reasons, an activation energy analysis would be devoid of physical meaning, as not all processes could be included. The only cell that has not undergone short circuit phenomena was the x = 0.5 one, that was indeed the only one in which no breaking of the pellet was observed (*Figure 6.5*). In this cell, an average increase of 28% in ASR values was evinced by the fitting with the equivalent circuit in *Figure 6.4*, while above 750°C the ASR values were reported to lower. This consideration is once again supporting the utilisation of the x = 0.5 sample for this aim, but should clearly be supported by new cells tests, in order to fully evaluate the phenomena and the performance resulting from the employment of this material and to confirm the higher mechanical stability that the x = 0.5 possibly gives to the device. Nevertheless, deeper analysis on the other electrodes should be carried out to better understand the validity of the collected data.

References

1 Basics of EIS: Electrochemical Research-Impedance Gamry Instruments, https://www.gamry.com/application-notes/EIS/basics-of-electrochemical-impedance-spectroscopy/.

2 B.-Y. Chang and S.-M. Park, Electrochemical Impedance Spectroscopy, *Annual Review of Analytical Chemistry*, 2010, **3**, 207–229.

3 Y.-H. Huang, R. I. Dass, J. C. Denyszyn and J. B. Goodenough, Synthesis and Characterization of $Sr_2MgMoO_{6-\delta}$, *Journal of The Electrochemical Society*.

4 S. Dhinakaran, K. Kavitha, M. Vanjinathan, R. Kumaran, N. Anuradha, M. Swedha, R. Vasanthi, S. Prabu and K.-Y. Chiang, Double perovskite material of highly active, monoclinic, ordered Ni_2ZnMoO_6 for an effective quasi-solid state supercapacitor, *Colloids and Surfaces A: Physicochemical and Engineering Aspects*, 2023, 132747.

5 Y. Liu, Z. Wang, Y. Zhong, X. Xu, J.-P. M. Veder, M. R. Rowles, M. Saunders, R. Ran and Z. Shao, Activation-free supercapacitor electrode based on surface-modified $Sr_2CoMo_{1-x}Ni_xO_{6-\delta}$ perovskite, *Chemical Engineering Journal*, 2020, **390**, 124645.

6 J. C. Ruiz-Morales, D. Marrero-López, J. Canales-Vázquez and J. T. S. Irvine, Symmetric and reversible solid oxide fuel cells, *RSC Adv.*, 2011, **1**, 1403.

7 S. Primdahl and M. Mogensen, Mixed conductor anodes: Ni as electrocatalyst for hydrogen conversion, *Solid State Ionics*, 2002, **152–153**, 597–608.

8 S. Primdahl and Y. L. Liu, Ni catalyst for hydrogen conversion in gadolinia-doped ceria anodes for solid oxide fuel cells, *Journal of the Electrochemical Society*, 2002, **149**, A1466–A1472.

9 Y. M. Park, H. J. Lee, H. Y. Bae, J. S. Ahn and H. Kim, Effect of anode thickness on impedance response of anode-supported solid oxide fuel cells, *International Journal of Hydrogen Energy*, 2012, **37**, 4394–4400.

10 M. Rao, S. H. Jensen, X. Sun and A. Hagen, Unwinding Entangled Degradation Mechanisms in Solid Oxide Electrolysis Cells Through Electrode Modifications and Impedance Analysis, *Fuel Cells*, 2019, **19**, 445–457.

11 W. Zając and J. Molenda, Properties of doped ceria solid electrolytes in reducing atmospheres, *Solid State Ionics*, 2011, **192**, 163–167.

12 B. Shri Prakash, S. Senthil Kumar and S. T. Aruna, Properties and development of Ni/YSZ as an anode material in solid oxide fuel cell: A review, *Renewable and Sustainable Energy Reviews*, 2014, **36**, 149–179.

13 D. A. Osinkin, E. V. Zabolotskaya, D. G. Kellerman and A. Yu. Suntsov, The physical properties and electrochemical performance of Ca-doped $Sr_2MgMoO_{6-\delta}$ as perspective anode for solid oxide fuel cells, *J Solid State Electrochem*, 2018, **22**, 1209–1215.

14 N. S. C. Priya, K. Sandhya and D. N. Rajendran, Study on Electrical conductivity and Activation Energy of doped Ceria nanostructures, *Electrochemical Energy Technology*, 2018, **3**, 49–53.

Conclusions and outlooks

The increasing energy consumption is among the principal issues that afflict the modern World, together with the constant growth of waste and CO_2 production. The evidences are widespread, and involving different fields of the society, starting from the environment (being climate change the principal sign of this critical situation) and moving on to economy, with the market speculation of big companies.

Thus, being evident the need to maximize and improve the utilization of renewable energy sources and to re-valorise the produced CO_2, this work was focused on the synthesis, characterization and lab-scale testing of perovskite-based catalysts for both CO_2 thermo-reduction via Reverse Water Gas Shift (RWGS) reaction and electrodes for a $H_2 + CO_2$-fed Solid Oxide Fuel Cell (SOFC); in particular, the target material was the $Sr_2Mg_{1-x}Mn_xMoO_6$ (SMMO) double perovskite family, a promising electrode materials' family that bases its scientific appeal on its versatility towards different fuels (H_2 and CH_4 feeding gasses are reported not to influence the cell performance) and its tolerance to H_2S impurities, widely known to be responsible of poisoning phenomena of the catalyst.

For this aim an 80% H_2 and 20% CO_2 gas mixture, being a simulation of the one produced by a dark fermentation of organic waste mediated by bacteria in the GPLabs facilities of Veritas company, was utilized.

Synthesis and characterization

The materials have been synthesized using the Pechini route, a wet chemistry route that ensures good reproducibility. As a matter of fact, the SMMO phase was not easy to stabilize, consequently different characterization methods have been performed to verify the phase purity and to establish which atmosphere is the most suitable to obtain this type of materials, but also to understand the possible effects of morphology and undesired phases on the catalytic activity.

The XRD diffractograms showed that the phase was synthesized properly in all the two studied environments: oxidative (air) and reducing (5% H_2 in Ar). Even if the SMMO double perovskite was present in all the samples, in the reducing atmosphere the phase purity was higher with relation to the other environment. This trend was observed in all SMMO materials (x = 0, 0.2, 0.5 and 1).

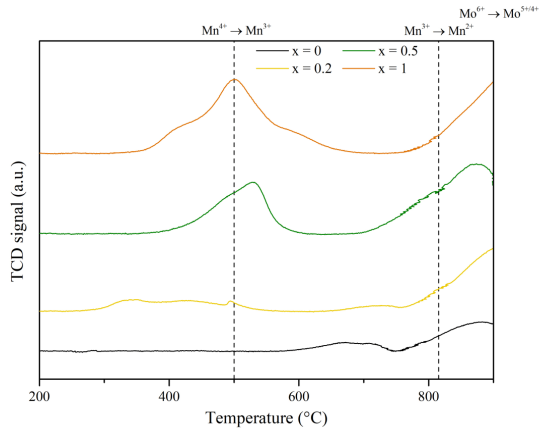

Graph C.1: H_2-TPR analysis of SMMO materials.

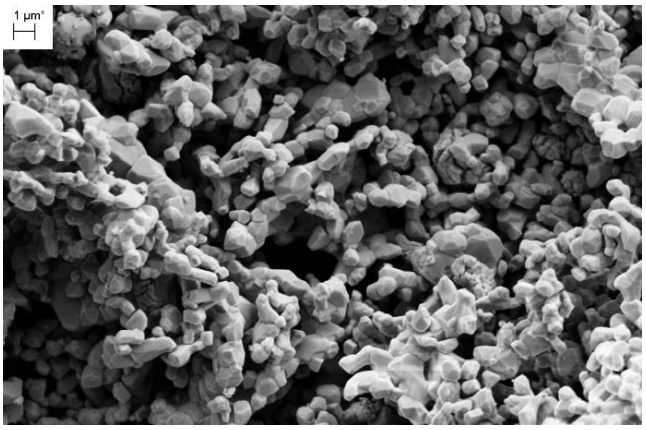

Figure C.1: SEM images of the x = 0 sample.

Material	Element	Theoretical (%)	EDX (%)	XPS (%)
x = 0	Sr	50.0	54.1	46.6
	Mg	25.0	20.7	36.4
	Mo	25.0	25.2	17.0
x = 0.2	Sr	50.0	48.2	41.5
	Mg	20.0	21.3	37.0
	Mn	5.0	6.9	3.4
	Mo	25.0	23.6	18.0
x = 0.5	Sr	50.0	40.0	55.4
	Mg	12.5	10.3	16.4
	Mn	12.5	14.6	5.4
	Mo	25.0	26.1	22.9
x = 1	Sr	50.0	47.4	60.3
	Mn	25.0	29.3	22.1
	Mo	25.0	23.2	17.6

Table C.1: comparison of theoretical and experimental percentage compositions of cations for the different samples.

A H_2-TPR analysis has been carried out in order to study the oxidation state of the cations inside the double perovskite structure. A twins-like behaviour was observed in samples x = 0 – 0.5 and x = 0.2 – 1 for what concerns the reduction peak lying around 900°C, coming from the convolution of the reduction of both manganese (III) to manganese (II) and molybdenum (VI) to molybdenum (V/IV). The principal hypothesis is the non (complete)-reduction of manganese (III) to manganese (II) in x =

0.5 sample, that is coherent with the behaviour of the x = 0 compound, in which the cation in question is obviously not present.

SEM images were acquired to have a graphical understanding of the powder morphology; all samples were characterized by a polyhedric-like shape with a mediocre porosity, mainly due to both the utilisation of ethylene glycol as cross-linker in the synthesis phase and the high thermal treatments required to achieve the correct and desired phase. More about the porosity of these materials will be explained in *Appendix A*.

EDX quantitative analysis were indicative of the surface segregation of strontium and magnesium cations in all samples, as the experimental values were lower than the nominal ones. Different results were obtained for manganese and molybdenum, whose experimental compositional values were in accordance with the theoretical ones within a few percentage units.

A not negligible surface segregation of strontium and magnesium cations with an increase in manganese content was observed by XPS analysis, hypothesizing a correlation between the phenomena (with the only exception of x = 0.2 sample) and confirming EDX results. Compositional techniques like EDX and quantitative XPS (*Table C.1*) were indicative of the scarce manganese presence on the surface of the samples, that was also confirmed by the qualitative XPS analysis.

Thermo-catalytic results

$$CO_2 + H_2 \xrightarrow{\Delta} CO + H_2O \qquad \text{(C.1)}$$

The catalytic performances of SMMO materials toward RWGS reaction (summarised in the *Eq. C.1*) have shown a behaviour similar to the one observed with the H_2-TPR analysis; in fact, a twins-like behaviour was again observed in samples x = 0 – 0.5 and x = 0.2 – 1, with the first two that have shown a higher (and comparable) CO yield at lower temperatures. This evaluation is in accordance with the hypothetical absence of manganese (II), and thus the presence of manganese (III), in the x = 0.5 sample, whose performances were the highest thanks to a co-operation of the high catalytic activity of manganese (III) cations (due to its ability to have a good oxygen exchange, as reported by previous literature works [1,2]) and the Lewis basicity of magnesium (II) sites [3]. Further investigation should be carried out in order to better understand the role of B-site cations in the reaction mechanism.

CO yield (*Graph C.2* and *C.3*) and CO_2 conversion were characterized by the same trend, with the first one slightly lower due to the not complete selectivity of the catalyst toward CO formation; in

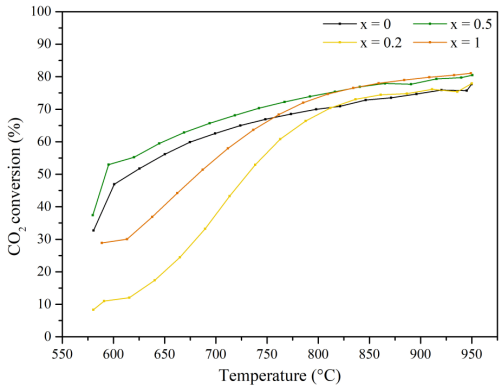

Graph C.2: CO_2 conversion percentage with respect to reaction temperature.

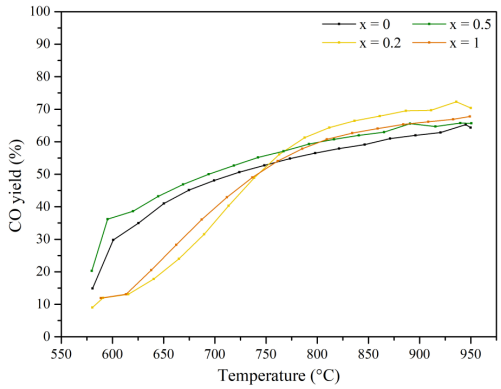

Graph C.3: CO percentage yield with respect to reaction temperature.

fact, the main hypothesis is that some of the starting CO_2 was converted into CH_3OH, lately undergone condensation in the chiller and so not analysed by the GC instrument. The comparison with the state-of-the-art materials has shown equal conversion degree, but shifted at higher temperatures (50% at 600°C for the x = 0.5 sample against the same value at 450°C for PMGs-based promoters [4,5]). The main benefit of changing the active material is the non-utilisation of PMGs materials, that are for instance very expensive and not environmentally sustainable.

No significant changes have been shown by the post-reaction XRD analysis, apart for the formation in minimum quantities of strontium carbonate phase ($SrCO_3$) in all samples and of a strongly defective double perovskite (i.e. $Sr_{11}Mo_4O_{23}$) in the x = 0.2 sample. This is an indication of a quite good cyclability of the SMMO catalysts, even if longer-lasting catalytic tests should be performed in order to have a better understanding of this aspect.

The SEM images acquired after the RWGS reaction cycle have shown no significant modification to the morphology and porosity of the samples; the polyhedric-like structure was maintained in all the SMMO family, together with the closed porosity.

The more evident phenomenon observed by EDX and quantitative XPS after reaction analysis was the surface segregation of strontium cation, in the samples with lower manganese content (x = 0, 0.2) which is substituted by the molybdenum surface segregation when the amount of manganese increases (x = 0.5, 1). Noteworthy, the amount of Sr revealed by the EDX is higher in the sample x = 0.5 in which Mo begins to prevail surface segregation. This last cation behaviour was only revealed by XPS thus indicating that this phenomenon only interests few outermost monolayers: an increasing tendency to undergo segregation with the increase in manganese content was observed. A decrease in carbonate species content was observed by fitting the C1s photopeak, as the relative contributions

Material	Element	Theoretical (%)	EDX post-GC (%)	XPS post-GC (%)
x = 0	Sr	50	54.4	51.7
	Mg	25	20.4	33.2
	Mo	25	25.2	15.1
x = 0.2	Sr	50	49.3	54.6
	Mg	20	19.1	17.6
	Mn	5	6.8	7.1
	Mo	25	24.9	20.7
x = 0.5	Sr	50	49.4	56.6
	Mg	12.5	12.0	14.8
	Mn	12.5	12.2	0.6
	Mo	25	26.4	28
x = 1	Sr	50	49.1	63.0
	Mn	25	27.1	7.4
	Mo	25	23.8	29.5

Table C.2: comparison of theoretical and experimental percentage compositions of cations for the different samples after RWGS reaction.

Material	Element	XPS fresh (%)	XPS post-GC (%)
x = 0	C ($M-CO_3$)	7.71	4.79
	O ($M-CO_3$)	33.45	12.93
x = 0.2	C ($M-CO_3$)	6.63	5.20
	O ($M-CO_3$)	25.17	8.86
x = 0.5	C ($M-CO_3$)	7.66	5.54
	O ($M-CO_3$)	25.05	11.65
x = 1	C ($M-CO_3$)	6.58	7.07
	O ($M-CO_3$)	20.93	24.55

Table C.3: comparison of XPS percentage composition of carbon and oxygen derived from the fitting of the carbonate contribution.

have dramatically decreased (with the only exception of x = 1 sample, mainly because of strontium segregation); this is consistent with a thermal removal of the spurious species, due to the high operating temperatures.

Electro-catalytic results

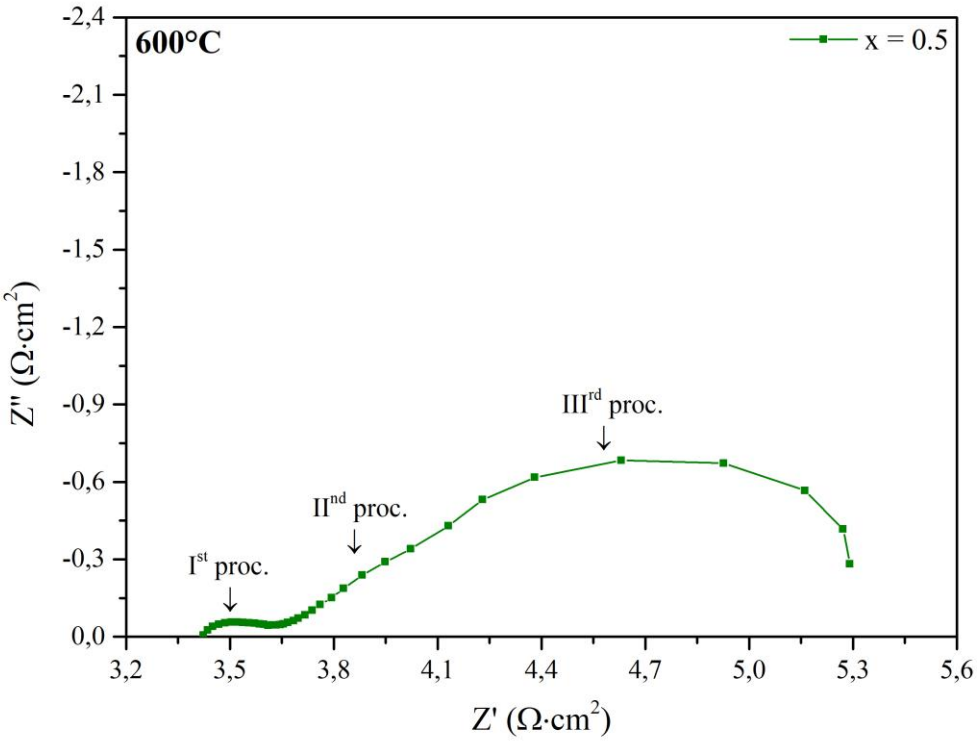

Graph C.4: Nyquist plot of the x = 0.5 cell, in H_2 + CO_2 fuel, at 600°C.

The symmetric cells were obtained by mixing 70% GDC and 30% SMMO powder (and α-therpineol as binder), deposited by tape casting of the GDC pellet and then sintered at 1200°C for 6 hours in air.

Three processes were observed by EIS analysis of the cells:

- the Ist process is temperature dependent and thus involved different phenomena like
  - at 600°C, the values in the range of kHz are related to charge transfer reaction [6]
  - at 650°C (and in general for T > 600°C in the x = 0.2 cell), a frequency in the range of the hundreds of Hz is indicative of Triple Phase Boundary (TPB) processes [7]
  - at T > 700°C, frequencies between 25 and 60 Hz are symptoms of diffusion-related processes [7]

	ASR H_2 ($\Omega \cdot cm^2$)				ASR $H_2 + CO_2$ ($\Omega \cdot cm^2$)			
T (°C)	**x = 0**	**x = 0.2**	**x = 0.5**	**x = 1**	**x = 0**	**x = 0.2**	**x = 0.5**	**x = 1**
600	1.19	5.25	1.82	3.89	2.10	2.02 *	2.24	1.81 *
650	0.28	0.49	0.28	0.26	0.32	1.11	0.36	1.28
700	0.12	0.14	0.09	0.15	0.08 *	0.57	0.12	0.58
750	0.04	0.08	0.05	SC	SC	0.34	0.05	SC
800	0.02	0.04	0.04	SC	SC	SC	0.02	SC

Table C.4: ASR values for H_2 and $H_2 + CO_2$ feeding gas.

Figure C.2: equivalent circuit utilized for the curves fitting.

- the IInd process, reported to take place at 0.2 Hz, is known in literature to be related to the slow dissociative hydrogen adsorbtion on the GDC surface [8,9]
- the IIIrd one is related to supercapacitive phenomena typical of molybdenum-based double perovskite structures [10]

The electrolyte resistances have shifted toward higher values once CO_2 was inserted in the feeding gasses; this is consistent with the partial utilization of the available hydrogen in the RWGS reaction. No dilution by means of CO_2 was observed, as the absolute hydrogen quantity was kept equal in the two tests (10 sccm).

The phenomenon at the basis of these tests is not clear, principally because of the hypothetical short circuit caused by the exposure of GDC electrolyte to a H_2-rich atmosphere and the consequent reduction of Ce (IV) to Ce (III); a H_2-TPR analysis on GDC powder should help understanding the temperature at which this reduction is manifested and so when the electrolyte loses the capability to be only an ionic conductor and starts to be an electronic conductor, thus indicating the short circuit threshold.

The only cell that has not undergone short circuit phenomena was the x = 0.5, that was indeed the only one in which no breaking of the pellet was observed. The overall performances of this material lie in the same order of magnitude of the state-of-the-art material, Ni-YSZ, thus opening to future possible research in this field. [11] In this cell, an average increase of 28% in ASR values was evinced by the fitting with the equivalent circuit in *Figure C.2*.

What's next?

Regarding the thermo-catalytic reduction of CO_2 to CO (RWGS reaction), a topic currently under scrutiny due to recent EU discussions on synthetic fuels produced through the Fischer-Tropsch reaction, there are two primary perspectives to consider. The first is the optimization of the synthetic route in order to maximize the surface area of the samples, which is usually strongly correlated with the catalytic activity as the catalyst should be more performing and efficient the more active sites are present. In this regard, new complexing agents (like EDTA or stearic acid, that are reported to have a higher complexing activity than citric acid [12]) should be tested, together with the lowering in calcination treatments temperatures; in fact, this last parameter is widely known to have an influence on the sintering process, and thus on the morphology and the porosity of the samples. Lastly, further investigations on the catalytic performances of the x = 0.5 sample should be carried out by means of an operando analysis, in order to clarify the eventual presence of manganese (III) and its influence on the material performance toward RWGS reaction. A possible investigative way can be an X-Ray Absorption Near Edge Structure (XANES), a technique that can provide information on the electronic structure or the unoccupied levels; a deeper study near manganese absorbing edge, being this technique influenced by the oxidation states of the elements, should be able to give an answer at the hypothesis that has been made in *Chaper 4*.

From the electro-catalytic point of view, the principal need is to overcome the utilisation of GDC at operating temperatures above 600°C, at which short circuit phenomena are evident (as reported in *Chapter 6*). To do so, as also reported by literature [13], the optimal electrolyte to be used would be LSGM together with a buffer layer made of Lanthanum-Doped Ceria (LDC), in order to avoid both the formation of undesired spurious phases (but maintaining a good compatibility with the electrolyte) and the mechanical failure of the electrolyte pellet under reducing atmosphere. Obtaining a chemical and mechanical stability would allow to perform new series of cells test, both symmetrical (to have a full electrochemical characterization of the SMMO materials family) and complete, thus evaluating the obtainable electrical power. Moreover, there will be the possibility to perform these tests under different feeding conditions, principally switching from hydrogen to methane, to have a confirm of the effective fuel versatility of the catalysts. Not negligible will be the role of the ink calcination environment; the goal will be to sinter the electrode in-situ (in a brand new set-up that will allow the exposition to different atmospheres of anode and cathode) in a reducing atmosphere, avoiding the formation of molybdate phases.

References

1 M. Ezbiri, V. Becattini, M. Hoes, R. Michalsky and A. Steinfeld, High Redox Capacity of Al-Doped $La_{1-x}Sr_xMnO_{3-\delta}$ Perovskites for Splitting CO_2 and H_2O at Mn-Enriched Surfaces, *ChemSusChem*, 2017, **10**, 1517–1525.

2 Q.-H. Wu, M. Liu and W. Jaegermann, X-ray photoelectron spectroscopy of $La_{0.5}Sr_{0.5}MnO_3$, *Materials Letters*, 2005, **59**, 1980–1983.

3 M. Isegawa and A. K. Sharma, CO_2 reduction by a Mn electrocatalyst in the presence of a Lewis acid: a DFT study on the reaction mechanism, *Sustainable Energy Fuels*, 2019, **3**, 1730–1738.

4 D. Kobayashi, H. Kobayashi, K. Kusada, T. Yamamoto, T. Toriyama, S. Matsumura, S. Kawaguchi, Y. Kubota, M. Haneda, S. M. Aspera, H. Nakanishi, S. Arai and H. Kitagawa, Boosting reverse water-gas shift reaction activity of Pt nanoparticles through light doping of W, *J. Mater. Chem. A*, 2021, **9**, 15613–15617.

5 M. Zhu, Q. Ge and X. Zhu, Catalytic Reduction of CO_2 to CO via Reverse Water Gas Shift Reaction: Recent Advances in the Design of Active and Selective Supported Metal Catalysts, *Trans. Tianjin Univ.*, 2020, **26**, 172–187.

6 Y. M. Park, H. J. Lee, H. Y. Bae, J. S. Ahn and H. Kim, Effect of anode thickness on impedance response of anode-supported solid oxide fuel cells, *International Journal of Hydrogen Energy*, 2012, **37**, 4394–4400.

7 M. Rao, S. H. Jensen, X. Sun and A. Hagen, Unwinding Entangled Degradation Mechanisms in Solid Oxide Electrolysis Cells Through Electrode Modifications and Impedance Analysis, *Fuel Cells*, 2019, **19**, 445–457.

8 S. Primdahl and M. Mogensen, Mixed conductor anodes: Ni as electrocatalyst for hydrogen conversion, *Solid State Ionics*, 2002, **152–153**, 597–608.

9 S. Primdahl and Y. L. Liu, Ni catalyst for hydrogen conversion in gadolinia-doped ceria anodes for solid oxide fuel cells, *Journal of the Electrochemical Society*, 2002, **149**, A1466–A1472.

10 Y. Liu, Z. Wang, Y. Zhong, X. Xu, J.-P. M. Veder, M. R. Rowles, M. Saunders, R. Ran and Z. Shao, Activation-free supercapacitor electrode based on surface-modified $Sr_2CoMo_{1-x}Ni_xO_{6-\delta}$ perovskite, *Chemical Engineering Journal*, 2020, **390**, 124645.

11 B. Shri Prakash, S. Senthil Kumar and S. T. Aruna, Properties and development of Ni/YSZ as an anode material in solid oxide fuel cell: A review, *Renewable and Sustainable Energy Reviews*, 2014, **36**, 149–179.

12 D. Navas, S. Fuentes, A. Castro-Alvarez and E. Chavez-Angel, Review on Sol-Gel Synthesis of Perovskite and Oxide Nanomaterials, *Gels*, 2021, **7**, 275.

13 Y.-H. Huang, R. I. Dass, J. C. Denyszyn and J. B. Goodenough, Synthesis and Characterization of $Sr_2MgMoO_{6-\delta}$, *Journal of The Electrochemical Society*.

Appendixes

Appendix A: Brunauer-Emmett-Teller (BET) analysis

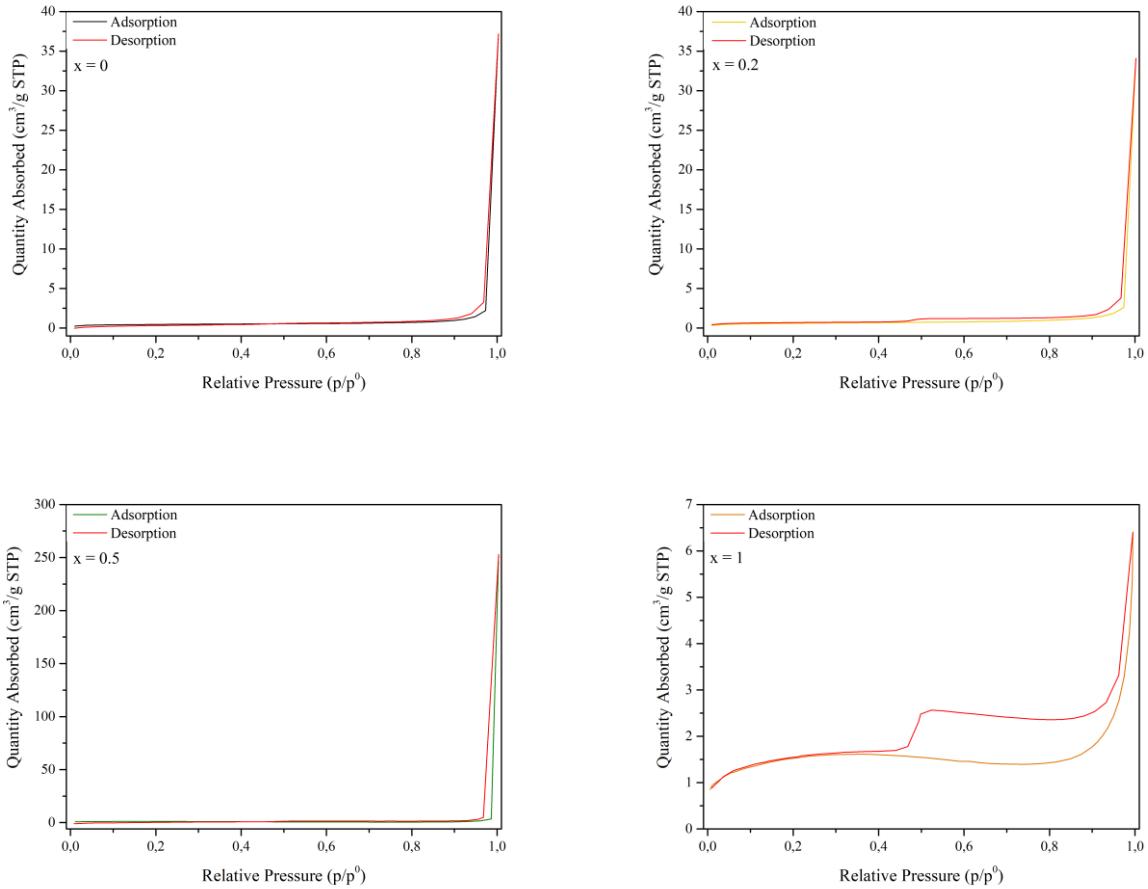

Graph A.1: BET isotherm curves of the SMMO samples.

Adsorption isotherms were obtained for all the samples using N_2 as the adsorptive gas, in order to characterize their Specific Surface Area (SSA). The measurements were carried out using an ASAP 2020 Plus Physisorption instrument. The samples were first degassed at 300°C for 3 hours in order to remove gas molecules adsorbed on the surface of the material, to then undergo analysis. During the analysis, the instrument has dosed a specific amount of gas inside the tube containing the sample in order to reach a predefine pressure defined by the user, then waited until equilibrium is reached, and measured the amount of gas adsorbed by the sample. This was done consecutively up until saturation pressure is reached, corresponding to relative pressure $p/p^0 = 1$. The sample was covered with N_2 molecules in different steps, comprising the adsorption of molecules on the surface, formation of a monolayer (corresponding to the whole surface covered by a single layer of gas molecules), onset of multilayer coverage and consequent filling of the sample pores by capillary condensation. Once

Material	SSA (m^2/g)
x = 0	1.50
x = 0.2	1.98
x = 0.5	3.24
x = 1	5.08

Table A.1: SSA values for the SMMO materials.

saturation pressure was reached, the instrument then proceeded to reduce the pressure inside the analysis tube (with consequent desorption of gas molecules from the surface) and measures the amount of gas adsorbed. By plotting the quantity of gas adsorbed (Q) versus the relative pressure (p/p^0), the adsorption isotherm of the sample is obtained, for both adsorption and desorption. This is a fingerprint of the sample, and its SSA can be determined using the BET model. This is a theory based on some thermodynamic assumptions that states that, by plotting the quantity $\frac{1}{Q[(p^0/p)-1]}$ over p/p^0 in the relative pressure range 0.05-0.3 a straight line is obtained.

The BET curves reported in *Graph A.1* appear to be a composite of mostly Type II and partly Type IV isotherms, indicating samples characterized by macro- and meso-pores [1]; in particular, this last kind of porosity is further confirmed by the presence of a hysteresis loop in the curves. Moreover, an increase in SSA with the increasing manganese content was observed, whose cause can be found in the considerations done in *Paragraph 3.6* and *3.7* by means of XPS analysis; in fact, manganese superficial presence was reported to be low, thus leaving the perovskite exposed, while a tendency of magnesium cation to undergo surface segregation was registered.

Appendix B: new SOFC testing set-up

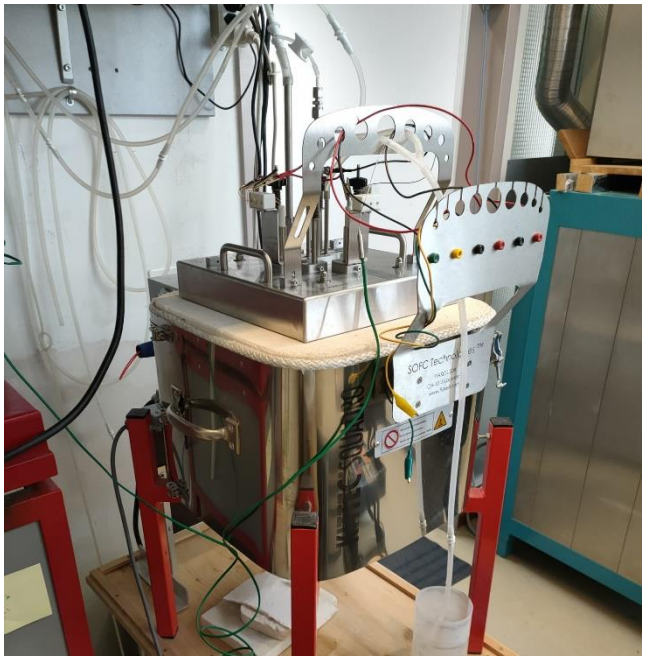

Figure B.1: the new SOFC testing set-up.

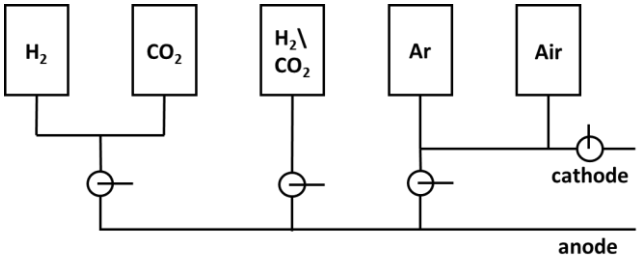

Figure B.2: schematic representation of the new gas management system.

Part of this work was also dedicated to the choice of a new SOFC testing set-up (shown in *Figure B.1*), to be utilized for further electrochemical evaluations of the designed and constructed cells. For this purpose, together with Fiaxell SARL, a company based in Lausanne (CH) that has made the design and construction of SOFC testing set-ups its main business activity, a new testing device was developed.

Going more into details, the device is equipped with a nickel housing flange for the cell, in which Inconel tubes are welded in order to carry the feeding gas to the SOFC; a centred tube is welded on the 6x5 cm nickel plate, and its function is to recover exhaust gasses (via two 4 mm diameter holes located at the cell periphery) for eventual compositional analysis via GC-MS. A long-term test kit, to avoid the poisoning from elements like chromium, iron or silicon, on the air side during the tests, was also designed. Moreover, a new cartridge was developed for the application of the set-up also in other fields, like steam reforming (with the help of a peristaltic pump), ammonia cracking and many others. The device, which is about to come soon in IMPACT facilities, will help to perform complete cells tests, by exposing the two sides to different atmospheres already for the inks calcination processes, thus avoiding the formation of impurities on the anode site and, simultaneously, not to expose the cathode side to an undesired reducing environment.

Together with the testing set-up, a new gas management system (schematized in *Figure B.2*) is under development with the help of the mechanical services of the Chemical Sciences Department.

References

1 M. Thommes, K. Kaneko, A. V. Neimark, J. P. Olivier, F. Rodriguez-Reinoso, J. Rouquerol and K. S. W. Sing, Physisorption of gases, with special reference to the evaluation of surface area and pore size distribution (IUPAC Technical Report), *Pure and Applied Chemistry*, 2015, **87**, 1051–1069.

Aknowledgments

In this section, dedicated to the people that have somehow participated in this journey, I want to switch to a language that surely will be more understandable by everyone, our mother language.

La prima persona che voglio ringraziare è la Prof.ssa Antonella Glisenti. Grazie per come mi hai accolto nel tuo gruppo, con estrema competenza scientifica ma soprattutto con molta vicinanza dal lato umano. Le sedute settimanali di "confessione" nel tuo ufficio sono state un toccasana, sia per quanto riguarda il prosieguo di questo lavoro che per il puro gusto di farsi una chiacchierata.

Alla base di una buona ricerca scientifica non sta una sola persona, ma la condivisione con gli altri. Grazie di cuore a tutti i componenti del gruppo IMPACT, perché con le vostre diverse specializzazioni mi avete insegnato cos'è la scienza al di fuori dei libri di testo. Le diversità di carattere mi hanno fatto capire quanto l'essere buoni colleghi sia fondamentale per non sentire il peso del lavoro e, se sono felice di far parte di questa famiglia, voi ne siete gli artefici. Però, per favore, non rubatemi il primato al SEM.

Un ringraziamento speciale, tra i vari membri di IMPACT, lo voglio dedicare a Chiara e Michele, che con me hanno condiviso questo periodo di tesi tra misure sbagliate o interrotte, celle non adese e bilance non calibrate, e che sono diventati in poco tempo delle persone di riferimento anche fuori l'università. *Quelli della stanza del Micro*.

Mamma e papà, grazie di tutto. Mi avete supportato e sopportato in ogni cosa, moralmente e non, nei momenti di gioia come questo e nei tanti momenti difficili che abbiamo passato. Queste due righe non saranno mai abbastanza significative di tutto ciò che avete fatto e che continuate a fare, ma spero che siano per voi un orgoglio. Questo traguardo è anche vostro.

Grazie a Maria Vittoria, che è parte della mia vita da più di sei anni e che da così tanto tempo si subisce gran parte dei miei difetti. Il tuo sorriso è sempre stato la migliore medicina contro le brutte giornate e le tue proposte spesso strampalate il miglior modo per staccare dalla monotonia dello studio. Magari però la prossima volta a Casa Milan ci andiamo.

Come potrei non ringraziare i miei amici storici? Non potrei! Provo ad elencarvi tutti: grazie a Carlo, Alessia, Sporz, Alice, Matteo, Diletta, Ricky, Pat, Piovan, Fra, Andrea e Thomas. Dieci anni fa è iniziato tutto con un'uscita in bicicletta e, senza accorgermi dello scorrere del tempo, ho passato con voi i momenti migliori della mia adolescenza, come i torneassi ("SCARSSSO"), le peripezie nel piazzale di un benzinaio a Latisana (povera Clio), gli Skribbl.io in pandemia e i milkshake al chiaro di luna ai Sampieri. Tralasciamo però le ginocchia sbucciate sul chilometro della morte ed i palloni finiti

in Fiumicello dal campetto di Don Frank. Avete spesso sopportato le mie pare, tirandomi su il morale, e non sapete quanto sia stato importante.

A tutti gli amici non citati sopra, non mi sono dimenticato di voi! A Ettore e Calise, con cui ho condiviso una vita sui banchi, prima al liceo e poi all'università. A Simone e Nicolò e i *troppi* meme mandati su IG. A Sofia e alle sue sempre dolci parole. A Elena e alle risate che ci facciamo alle spalle della Mari. A Nicola, alle nostre tante passioni condivise e al suo spronarmi ad essere sempre meglio. Grazie, senza di voi non sarebbe stato lo stesso.

Per ultima voglio ringraziare una persona speciale, a suo modo una delle mie ammiratrici più grandi, che sta festeggiando questo momento con me, ma guardandomi da lontano. Posso solo immaginare come esprimeresti la tua felicità e come mi dimostreresti di essere orgogliosa di me, e mi piace pensare che tu ora lo stia facendo. Questo lavoro è dedicato a te.

“I’m so happy that I am alive,

In one piece, and short”

Sergeant Joker, “Full Metal Jacket”